GROWTH, STRUCTURE AND TRIBOLOGICAL PROPERTIES OF ATOMIC LAYER DEPOSITED LUBRICIOUS OXIDE NANOLAMINATES

Benedict Anyamesem Mensah, B.S., M.S.

Dissertation Prepared for the Degree of

DOCTOR OF PHILOSOPHY

UNIVERSITY OF NORTH TEXAS

December 2010

APPROVED:

Thomas W. Scharf, Major Professor
Richard Reidy, Committee Member
Jincheng Du, Committee Member
Witold Brostow, Committee Member
Nigel Shepherd, Committee Member
Narendra Dahotre, Chair of the Department of Materials Science and Engineering
Costas Tsatsoulis, Dean of the College of Engineering
James D. Meernik, Acting Dean of the Robert B. Toulouse School of Graduate Studies

Mensah, Benedict Anyamesem, Growth, structure and tribological properties of atomic layer deposited lubricious oxide nanolaminates. Doctor of Philosophy (Materials Science and Engineering), December 2010, 176 pages, 7 tables, 56 figures, 132 references.

Friction and wear mitigation is typically accomplished by introducing a shear accommodating layer (e.g., a thin film of liquid) between surfaces in sliding and/or rolling contacts. When the operating conditions are beyond the liquid realm, attention turns to solid coatings. Solid lubricants have been widely used in governmental and industrial applications for mitigation of wear and friction (tribological properties). Conventional examples of solid lubricants are MoS_2, WS_2, h-BN, and graphite; however, these and some others mostly perform best only for a limited range of operating conditions, e.g. ambient air versus dry nitrogen and room temperature versus high temperatures. Conversely, lubricious oxides have been studied lately as good potential candidates for solid lubricants because they are thermodynamically stable and environmentally robust. Oxide surfaces are generally inert and typically do not form strong adhesive bonds like metals/alloys in tribological contacts. Typical of these oxides is ZnO. The interest in ZnO is due to its potential for utility in a variety of applications. To this end, nanolaminates of ZnO, Al_2O_3, ZrO_2 thin films have been deposited at varying sequences and thicknesses on silicon substrates and high temperature (M50) bearing steels by atomic layer deposition (ALD). The top lubricious, nanocrystalline ZnO layer was structurally-engineered to achieve low surface energy {0002}-orientated grain

that provided low sliding friction coefficients (0.2 to 0.3), wear factors (range of 10^{-7} to 10^{-8} mm^3/Nm) and good rolling contact fatigue resistance. The Al_2O_3 was intentionally made amorphous to achieve the {0002} preferred orientation while {101}-orientated tetragonal ZrO_2 acted as a high toughness/load bearing layer. It was determined that the ZnO defective structure (oxygen sub-stoichiometric with growth stacking faults) aided in shear accommodation by re-orientating the nanocrystalline grains where they realigned to create new friction-reducing surfaces. Specifically, high resolution transmission electron microscopy (HRTEM) inside the wear surfaces revealed in an increase in both partial dislocation and basal stacking fault densities through intrafilm shear/slip of partial dislocations on the (0002) planes via a dislocation glide mechanism. This shear accommodation mode mitigated friction and prevented brittle fracture classically observed in higher friction microcrystalline and single crystal ZnO that has potential broad implications to other defective nanocrystalline ceramics. Overall, this work has demonstrated that environmentally-robust, lubricious ALD nanolaminates of $ZnO/Al_2O_3/ZrO_2$ are good candidates for providing low friction and wear interfaces in moving mechanical assembles, such as fully assembled rolling element bearings and microelectromechanical systems (MEMS) that require thin (~10-200 nm), uniform and conformal films.

ACKNOWLEDGEMENTS

I would like to express my deepest gratitude to my major professor, Dr. Thomas W. Scharf, for all the support and guidance he offered me during the course of my study here at UNT. The knowledge I have gained from him is invaluable and I feel privileged to have had the opportunity to work under his supervision. I also want to express my appreciation to Drs. Rick Reidy, Jincheng Du, Nigel Shepherd and Witold Brostow for serving on my dissertation committee. Their suggestions and immense contributions improved this work tremendously. To Nancy Bunce and Dr. Dave Diercks, (CART) thank you so much for the tool training. I would like to express my thanks to my colleagues from the LAMMA group (Hamid, Anchal, Jon-Erik, Kyle and Wei Lun) for the help on instrumentation and problem discussions. You guys really rock! This work would not have happened without my friends at UNT, Eric, Ghare, Nelson, Carl, Arun, Antarikish, Mohammed, Fan Lin, Drs. Minghang, Ming Ti, Sonny and Koffi, thanks for all your assistance throughout this study and my stay at UNT.

I could not have come this far without the love and support of my family, to my wife Akos and kids (Maureen and Josiah) thanks for understanding and motivating me to achieve this aim. Furthermore, I would like to thank my mum Margaret and my in-laws for the moral and prayer support. The Mathis family cannot be left out; your support to me has been immeasurable. I love you all. Finally, I would like to thank God almighty for giving me the strength and ability to achieve my target, I will forever be grateful.

TABLE OF CONTENTS

Page

Page

Page

LIST OF TABLES

Page

LIST OF FIGURES

Page

Page

Page

Page

Page

CHAPTER 1

INTRODUCTION

1.1 Historical Perspective

Friction is defined as the force that helps in resisting the relative lateral motion of solid surfaces or fluid layers in contact. It has been known and studied for ages. The laws of friction have a rich history. The theories, deductions and experiments of scientific geniuses Leonardo da Vinci (1452-1519), Isaac Newton (1643-1727), Guillaume Amontons (1663-1705), and Charles Coulomb (1736-1806) give the world its first intellectual insights into the world of friction.[1] Leonardo da Vinci, ca. 1500, realized how important friction was for the working of machines and according to his notebooks, he found that friction is independent of contact area and frictional resistance of a body is about 1/4 of its weight (both of which are generalizations). In 1699, French physicist Guillaume Amontons, who was unaware of da Vinci's work, published his own work on friction. Attempting to explain friction, he theorized that friction is caused by surface roughness. The peaks of one surface lay in the valleys of the adjoining surface, and Amontons believed that friction is the force required to pull the peaks up the other surface until they clear. He rediscovered the laws of friction for dry sliding between two flat surfaces (1^{st} law: friction force is proportional to normal force and 2^{nd} law: magnitude of friction force does not depend on the apparent area of contact). Several years later, French physicist Charles Augustin de Coulomb (1785) verified Amontons' observations

and postulated another friction law: the frictional force is independent of velocity once motion starts. He also studied the difference between static friction and kinetic friction. As to the cause of friction, Coulomb theorized that at least part of the frictional force might result from cohesion of molecules of the two sliding surfaces. Many developments occurred over the years until 1950 when Francis Bowden and David Tabor (Cavendish Laboratory, Cambridge University, UK) elucidated many of the current mechanisms for reduction of friction and wear; as examples, using soft coatings and adherent molecular and lubricant surface layers.[2,3] It should be noted that the aforementioned laws of friction are empirical in nature and there are cases in which they do not apply. For example, Chapter 5 shows an example where the friction force for nanocrystalline zinc oxide (ZnO) coatings does not increase linearly with normal force as predicted by Amontons; instead, it follows a normal force to the -1/3 power, which is consistent with the Bowden and Tabor analysis for Hertzian contacts.

1.2 Motivation

Solid and liquid lubricants are substances that are introduced between two moving surfaces to reduce friction, which results in wear reduction and overall improved efficiency.[4] Hence in situations where friction needs to be mitigated, lubricants have been used to minimize interfacial contacts. The first evidence of society using lubricants was from the Egyptians, whom used water to help lubricate sleds that carried massive stone monuments and later from the Romans whom used rags dipped in animal fat (lard) to lubricate wagon wheels.[2] In more recent times mankind has replaced these kinds of

natural lubricants with synthetic oils and greases from petroleum distillates due to their efficiency in modern machinery.

Unfortunately liquid-based lubricants have limitations which make them not applicable to the ever increasing demand for future extreme applications. Some of these limitations include (but not limited to) the fact that they

- Are likely to degrade or decompose at high temperatures or under high radiation fluxes
- Cannot be used in high vacuum environments or inert atmospheres (e.g. outer space)
- Can solidify or congeal at low temperatures, or volatize in high-vacuum environments[5]

Due to these technological challenges and demanding applications, in the past several years solid lubricants are being increasingly employed in extreme environments (e.g., high temperatures, ultrahigh vacuum) as a solution to areas where the liquid lubricants are not applicable. Solid lubricants are materials which despite being in the solid state are able to reduce friction between two surfaces sliding against each other without the need for a liquid media.[6] The process of solid lubrication has been described with many names; these including "dry lubrication, dry-film lubrication, solid lubrication, and solid-film lubrication", which all imply that the process occurs under non-liquid conditions. Therefore in a broad sense, lubrication by solids embraces any process where a lubricating solid is present between the contacting materials.[5]

Specifically, solid lubricants generally have the following advantages over liquid lubricants:

- Higher stability and better tribological properties in extreme cyclic conditions, such as high-temperatures (> 500^{o}C) to cryogenic temperatures (< ^{o}C) operation, ultrahigh vacuum (10^{-9} to 10^{-10} torr) to ambient pressure and ambient air (high humidity) to dry nitrogen (low humidity) environments
- Higher order of effectiveness at high loads and slow speeds
- Liquid lubricants are sometimes not appropriate due to migration and aging (liquid can settle leaving some parts unprotected)
- Provide design simplification because lubrication distribution systems and seals are not required

The following can be considered as disadvantages:

- Do not have the ability to self-heal or replenish in the tribological contact
- Can eventually wear away over time
- In some lubrication regimes, such as hydrodynamic lubrication, they have higher friction and resultant wear
- Have high coefficient of friction and wear than for hydrodynamic lubrication
- Their color may be undesirable, such as with graphite and carbon nanotubes[5]

Individual solid lubricants that are currently available mostly perform best only for a limited range of operating conditions. For example, environment plays a significant role in determining the tribological performance of thin films and coatings that are designed to mitigate friction and wear. Coatings that give extremely low friction and

long wear life in one environment can fail to do so in a different environment. There are many classes of solid lubricating materials in both bulk and coating form: (a) transition metal dichalcogenides such as MoS_2 and WS_2, (b) carbon-based materials like graphite, diamond-like carbon, nanocrystalline diamond, (c) polymers, such as polytetrafluoroethylene, PTFE, and (d) soft metals like silver, tin, indium, gold and their alloys. Barring a few exceptions, most of these materials can be applied as thin coatings on tribological components (bearings, seals, magnetic hard drives, etc.) to reduce friction, wear and debris generation.

1.2.1. Transition Metal Dichalcogenides

1.2.1.1. Molybdenum Disulfide (MoS_2) and Tungsten Disulfide (WS_2)

Among the various members of the transition metal dichalcogenides family of compounds, MoS_2 and WS_2 are well known for their solid lubricating behavior and are widely used in practical applications. Their lubricating behavior stems from their intermechanical weakness which is intrinsic to their crystal structure. For example, MoS_2 crystallizes in the hexagonal structure where a sheet of molybdenum atoms is sandwiched between two hexagonally packed sulfur layers with a high c/a ratio (c=12.29Å, a=3.16Å). The bonding within the S-Mo-S sandwich is covalent, while weak Van der Waals forces hold the sandwich together resulting in interlamellar mechanical weakness. Thus, under a shearing force the basal planes slide over one another by intracrystalline slip and transfer to the rubbing counterface. The main mechanisms for imparting low interfacial shear are: a) creation of the (0002) basal plane by separating the weakly bonded sandwiches and subsequent reorientation parallel to the sliding direction, and b)

the development of a transfer film on the counterface to accommodate interfacial sliding. The ability of MoS_2 and WS_2 to form transfer films on the counterface implies that is not necessary to coat both surfaces of the sliding couple; coating one contacting surface would suffice to generate low friction after the initial run-in period. Also, it is not necessary to have fully crystalline films with the preferred parallel crystallographic texture. Several experimental studies confirmed that friction would induce crystallinity into MoS_2 and WS_2 films that lack long range order, and orient the (0002) planes parallel to the sliding direction during the run-in period. Tungsten disulfide also behaves in a similar fashion, but it is more expensive to synthesize compared with the naturally occurring molybdenite. However, WS_2 is thermally stable to approximately 500 to 550ºC, while the performance of MoS_2 begins to deteriorate above 400ºC.[7,8] Both MoS_2 and WS_2 coatings exhibit extremely low friction coefficients (μ~0.02 or less) and long wear life (several million sliding cycles) when employed in either dry inert gas or in ultrahigh vacuum.[9] However, when sliding in humid air, dangling or unsaturated bonds on the edge of basal planes react with moisture and oxygen in the environment to form tribooxidation products, such as MoO_3 and WO_3, resulting in higher friction (0.15-0.2) and extremely short wear life.[10]

1.2.1.2. Doped MoS_2 and WS_2

There is an increasing demand for environmentally robust solid lubricant coatings that can adapt themselves to different.[11] For instance, even if the targeted application is friction mitigation in space, often times the satellites and satellite launch vehicles wait for extended periods of time in humid coastal environments prior to launch, potentially

exposing the moving mechanical assemblies to humidity. In view of this, there have been major studies aimed at developing multi-phase materials known as adaptive lubricants and chameleon coatings.[12] A number of metal or oxide dopants in MoS_2 have also been successfully tried. Notable examples of dopants include: Ti, Al, Ni, Au, Pb, PbO, and Sb_2O_3. The presence of these dopants can lead to increased coating density, hardness and oxidation resistance in humid environments compared to pure MoS_2. Amongst these, Sb_2O_3 and Au doped MoS_2 films[12,13,14] and Ti doped MoS_2 films[15] are gaining acceptance as robust coatings for commercial use, including for applications in satellites.

1.2.2 Carbon-Based Materials

1.2.2.1 Graphite

Graphite is also a layered solid with a hexagonal lattice and high *c*/*a* ratio (c = 6.71Å, a = 2.46Å).[10] Similar to MoS_2, the carbon atoms in their basal planes are held with strong covalent bonds while the basal planes themselves are held together by weak Van der Waals cohesive forces, resulting in interplanar mechanical weakness. The presence of water vapor in the environment and crystal defects are believed to facilitate the interlamellar shearing of graphite crystals. These basal planes exhibit low surface energies and have little adhesion amongst them. However, when the basal plane becomes damaged, high energy edge sites of the lamellae are exposed and bond strongly to other edge sites causing increased adhesion. Low friction is maintained when these reactive edge sites are neutralized (passivated) by the adsorption of water, or other condensed vapors.[10] Unlike the case of MoS_2 and WS_2, graphite needs moisture, or adsorbed gases, in the environment (>100 ppm) - they either act as intercalants or passivate the dangling

covalent bonds, or both, to lubricate. In vacuum and in dry environments, graphite without additives exhibits high friction - a phenomenon known as "dusting," first observed in the late 1930s when graphite brushes in aircrafts experienced accelerated wear at high altitudes. The most widespread use of graphite (besides electrical contact brushes) in anti-friction applications is in metal- and polymer-matrix self lubricating composites as 'built-in' solid lubricant. Sometimes graphite is also applied as a resin bonded coating.

1.2.2.2. Diamondlike Carbon (DLC)

DLC coatings are typically amorphous with short range ordered phases of mixed sp^3-type tetrahedral bonding (diamond hybridization) and sp^2-type trigonal bonding (graphitic hybridization). These are known to exhibit an unusual combination of tribological and mechanical properties: low friction coefficients and low wear rates, relatively high hardness, and high elastic modulus.[16] DLC materials doped with hydrogen (~10–50 at.%) are commonly referred to as hydrogenated DLC. Alternatively, DLC can be doped with S, Si and SiO_x, as well as transition metals, such as Cr, W and Ti, which form nanoscale hard metal carbide phases, to improve their mechanical behavior and wear resistance. The friction coefficients of DLC coatings range from 0.001 to 0.5 depending upon the test conditions (i.e., contact stress, sliding velocity, temperature) and the environment. In addition, the chemical bonding and hydrogen content of the coatings profoundly influence the friction coefficient. For instance, hydrogen-free DLC coatings work best in humid air where low friction coefficients (~0.1) can be achieved for long durations, while hydrogenated coatings perform better in dry or inert gas environments.

Synthesizing one single DLC material to achieve low friction in both dry and humid environments can be a challenging task. Recent research shows promise for environmentally-robust tribological nanocomposite coatings, such as diamondlike nanocomposite (DLN), whose structure has been conjectured to consist of two amorphous interpenetrating networks, a diamondlike (*a*-C:H) network and a quartzlike (*a*-Si:O) network with minimal bonding between the two networks.[17] The mutual stabilization of these networks prevents the growth of graphitic carbon at high temperatures as well as serves to enhance the adhesion and reduce the internal stress to approximately −0.5 GPa. The composition of DLN can vary but is typically around $(CH_{0.15})_{0.7}(SiO_{0.3})_{0.3}$.

There are many similarities in the tribological behavior of DLN and MoS_2. For instance, DLN (as well as many other DLCs) transfer a thin layer of material from the coating to the counterface, known as a transfer film. Thus, it is not necessary to coat both surfaces of the friction couple. Secondly, DLN also exhibits non-Amontonian behavior with friction coefficient decreasing with increasing Hertzian contact stress. Chemical mapping by Time-of-Flight Secondary Ion Mass Spectroscopy (ToF-SIMS) aided by Automated eXpert Spectral Image (AXSIA) software showed that the transfer film in dry nitrogen was predominantly a mixture of long range carbon and hydrogenated carbon while in humid air it was composed of mostly silicon oxide species.[18] It appears that by forming transfer films of long range carbon and hydrogenated carbon in dry nitrogen, and predominantly silicon oxide species in humid air, DLN is able to adapt itself to both dry and humid environments, thus becoming an environmentally-robust low friction coating.

Besides the inherent tribological behavior and the environmental effects discussed above, coating-substrate interface plays a critical role in governing the coating performance. For instance, DLCs are known to have adhesion issues with substrate materials that contain non-carbide forming elements. In such cases, a thin Ti adhesion layer is typically applied prior to depositing DLC. Focused ion beam (FIB) microscopy and finite element analysis modeling (FEM) are important tools to study coating-substrate interface reliability. FIB-sections of wear scars are routinely made to visualize friction-induced subsurface deformation and to validate FEM.[18,19] For example, when contact stresses are increased beyond a limit that the substrate begins to plastically yield, Hertzian elastic contact theory is no longer valid. This underscores the need to design multilayer coating architecture (e.g., a hard coating sandwiched between DLN and the softer substrate) to withstand higher operating stresses.

1.2.2.3. Nanocrystalline Diamond

Diamond films offer many attractive properties such as high hardness, stiffness, thermal conductivity and high resistance to wear. Diamond when applied as a coating with ultrananocrystalline structure, i.e., ~3-5 nm grains, is referred to as ultrananocrystalline diamond, or UNCD. UNCD exhibits low surface roughness (~13 nm RMS) and low friction in both dry nitrogen and humid air. Like MoS_2/Sb_2O_3/Au and DLN coatings, the friction coefficients of UNCD (self-mated configuration) decreased with increase in Hertzian contact stress. However, unlike MoS_2/Sb_2O_3/Au and DLN coatings, the friction coefficients and interfacial shear strengths are lower in humid air than in dry nitrogen, which may be due to adsorbed water passivating the dangling bonds

on the UNCD surfaces.[20] Furthermore, it is desirable to coat both surfaces of the friction couple and use it in self-mated configuration to avoid wear of the uncoated counterface.[21]

1.2.3 Polymers

Among polymeric materials, polytetrafluoroethylene (PTFE) is well known for its antifriction property.[10] This follows from its smooth molecular profile and low intermolecular cohesion.[22] PTFE has no unsaturated bonds and is not easily polarized. During sliding contact it forms a thin transfer film of itself on the counterface, like the previously mentioned solid lubricant coatings. Unfortunately, the low intermolecular cohesion responsible for easy drawing of molecular chains out of the crystalline portions of the polymer, which gives rise to low friction (~0.1 against a steel counterface), results also in unacceptable amounts of wear.[23,24] Thus, it is impossible to achieve the desired combination of low friction and wear using PTFE alone. Without sacrificing the characteristic low friction of PTFE, its wear resistance can be improved (by up to a factor of 1000) by adding fillers to the PTFE matrix.[24] The improved wear performance of filled PTFE may be due to the formation of a continuous and strongly adhering of transfer film on the counterface. PTFE also shows decreasing friction coefficients with increasing contact stress, similar to other solid lubricants. PTFE is used as a matrix in self-lubricating composites as well as solid lubricant fillers (fibers and powders) in composites, e.g., electroplated Ni-PTFE coatings, for low friction applications. However, attempts to deposit thin coatings of PTFE by physical vapor deposition techniques often result in cross-linking the polymer and loss of its antifriction characteristics.

1.2.4. Soft Metals

Soft metals, such as lead, tin, indium, silver and gold when applied as thin films on relatively hard substrates can result in low shear strengths and hence low friction. The widespread use of Pb, Sn and In is in bearing alloys. Examples include Babbit metals based on needle shaped intermetallics in a tin-rich matrix, leaded bronzes containing islands of lead in a bronze matrix and Al-Sn alloys. These are applied as thick overlays in steel backings to fabricate the bearings. Silver is sometimes used as a filler in high temperature self-lubricating and composites.[24,25] Thin layers of soft metal can either provide shear accommodation or their low melting eutectics can result in melt lubrication at asperity contacts.

CaF_2, BaF_2, PbO, and B_2O_3 are other solid lubricants that also provide lubrication at high temperatures, since their shear strength decreases at these high temperatures just like the soft metals. But after melting, they become glass-like and are highly prone to cracking when used again at low temperatures.[26] Accordingly, better solid lubricants that can perform over a wide range of extreme conditions, have low friction coefficient and good wear resistance are necessary.

Oxides have been studied lately as good potential candidates for solid lubrication because they are thermodynamically stable in air and even at elevated temperatures. Oxide surfaces are generally inert and typically do not form strong adhesive bonds like metals in tribological contacts. The inability of single crystal and microcrystalline oxides to deform plastically or shear prevents them from obtaining low friction, as well as forming friction reducing third-body films on wear surfaces and the wear debris formed

from them is usually abrasive. That is, due to their brittle nature at room temperature, there has been little attention given to oxides as possible candidates as solid lubricants. Studies by Karch et al.[27] determined that if the grain size of conventional polycrystalline ceramics (oxides included) can be reduced down to a few nanometers, it would become ductile. They concluded that, the ductility seemed to originate from the diffusional flow of atoms along the intercrystalline interfaces. Schoitz et al.[28] with the help of computer simulations also reported that grain boundary sliding was in large parts responsible to the plastic deformation in nanocrystalline metal with a minor contribution from dislocation activity in the grains. It was therefore realized that plastic deformation in ceramics could be exhibited by nanocrystalline films at low temperatures. The grain size refinement was applied by Zabinski et al.[29] in their quest of studying the use of ZnO as a solid lubricant over a wider range of temperatures. They reported that thin film nanocrystalline grain size zinc oxide has high potential to be lubricous material because it is relatively soft, ductile and the chemical stoichiometry and microstructure can be controlled to introduce defects into the film. Their tribological sliding measurements showed a friction coefficient of ~0.2 while bulk ZnO film exhibited coefficient of friction values of ~0.7-0.8 at room temperature. As the grain sizes increased and approached that of conventional oxides especially with the increase in coating thickness, the coefficient of friction also increased and lubricity is eventually lost. Romanes[30] addressed the issue of growing a thick film and maintaining the nanometer grain size based on the Elam et al.[31] hypothesis that by alternating ZnO and a second oxide in a nanolaminate configuration, the nanometer grain size could be preserved. Romanes reported on the crystal structure

and tribological behavior of ZnO/Al_2O_3 nanolaminate; in particular the effect of growth temperature and their interfacial density. The nanolaminate films were deposited by an atomic layer deposition (ALD) technique. Therefore, the motivation of this research is to determine what combination and sequence of ALD deposited nanolaminates of ZnO, aluminum oxide (Al_2O_3) and zirconium oxide (ZrO_2) (high fracture toughness ceramic) will provide the best tribological behavior based on engineering the nanolaminate structure and tailoring its structural defects. In addition, the dissertation will focus on the effect of how *ex-situ* annealing changes the nanolaminate crystal structure and tribological (friction and wear) properties.

As the thickness of thin films continues to be scaled down, deposition tools that can coat with high-quality and ultra thin films are required. Typical chemical vapor deposition (CVD) or physical vapor deposition (PVD) techniques are difficult to achieve conformal and uniform films with the appropriate thickness, and they are also not capable of coating structures with high aspect ratios (buried interfaces/shadowed surfaces). ALD is currently considered as one of the most promising thin film deposition techniques for enabling nanoscale device fabrication. ALD is suitable for manufacturing inorganic material layers with thickness down to a fraction of a monolayer. The ALD technique offers unprecedented thickness control, quality, uniformity and material properties of the monolayer films. It has the capability to coat extremely complex shapes with a conformal material layer of high quality capability unique among thin-film deposition techniques. Due to these unique properties, ALD is finding more applications.[32,33,34]

The nanolaminate solid lubricant will be grown on Si and M50 high temperature bearing steel with more details in Chapter 3. The M50 bearing steels will be used for high temperature rolling contact fatigue (RCF) applications in order to study the lifetime of the coated nanolaminate film. RCF results in surface damage when stress is repeatedly applied where two bodies roll on one another. It is a family of damage phenomena like cracking or pitting/delamination that are limited to the near-surface layer of bodies in rolling contact.[35] It is responsible for the failure of rolling element bearings, gears, and camshafts. Due to increased demands and harsher extreme operation conditions (i.e., higher temperatures, contact pressures, severe environmental conditions that can lead to corrosion, oxidation and erosion) than before, new solid lubricants that can meet these challenges are needed.[36] There are two key processes that govern RCF: crack initiation and crack propagation which are related to the characteristics of the surface quality, stress distributions and lubrication conditions. But the main factor that causes RCF failure presently is the surface crack defects.[37] In order to prevent crack initiation and propagation, a tough ceramic oxide with a very high elastic modulus is required; ZrO_2 is one of the toughest ceramics at low temperatures. ZrO_2 was used as a high toughness/-load bearing layer, which shown in chapter 4 helped prevent any crack initiation and propagation in the nanolaminate film. Additionally, the topmost lubricous nanocrystalline ZnO layer was structurally-engineered to achieve low surface energy, textured (0002)-orientated grains, which provided low sliding friction coefficient and wear factors. This ZnO texture was achieved by depositing an amorphous Al_2O_3 layer beneath the ZnO layer.

Therefore this study is aimed at how the film texture/structure influence the friction and wear properties. The deformation mechanism that is associated with the low coefficient of friction values is quantified. The friction and wear reducing mechanism in ZnO was studied by focused-ion beam high resolution scanning electron microscopy (FIB/HRSEM) and high resolution transmission electron microscopy (HRTEM) analysis inside worn surfaces and subsurfaces..

1.3 Contributions of Dissertation

This work is aimed at providing the following answers to three important questions:

a. How does ALD processing determine the ZnO/ZrO_2 and $ZnO/Al_2O_3/ZrO_2$ nanolaminate defective structure and how this structure affects tribological properties?
b. How are the structure-property interrelationships affected by ex situ annealing of the nanolaminates?
c. Is nanoscale plasticity observed and if so what is (are) the plastic deformation mechanism(s) of the nanocrystalline ZnO layer after sliding and rolling (RCF)? This will be accomplished by using HRSEM/FIB and HRTEM analyses that can provide a site specific investigation of the tribologically-altered surface and subsurfaces.

1.4 Dissertation Overview

This dissertation deals with the ALD synthesis of ZnO, Al_2O_3 and ZrO_2 nanolaminates, their structural and tribological properties. It has six main chapters. This chapter (Chapter 1), provides a broad introduction to the genesis of friction, lubrication and the potential of the use of oxides as solid lubricants. The motivation for this study is also provided here. Chapter 2 discusses an overview of tribology, solid lubrication mechanism and the most recent studies on potential solid lubricants to be used in extreme conditions. This chapter also discusses the basic features of ALD, its benefits/limitations and a detailed ALD process for growing ZnO, Al_2O_3 and ZrO_2. Chapter 3 describes and discusses the experimental procedures and characterization techniques. Chapter 4 discusses the deposition of $ZnO/Al_2O_3/ZrO_2$ and ZnO/ZrO_2 nanolaminates on silicon substrate, the resultant structure and the role of defects in controlling the tribological properties of the films. In Chapter 5, a parallel study of $ZnO/Al_2O_3/ZrO_2$ nanolaminate film deposited on M50 high temperature bearing steel substrates is presented. Chapter 6 outlines with the conclusions based on the experimental results of the preceding chapters, as well as recommendations for future work. Each chapter ends with a list of works that were referenced.

1.5 Chapter References

[1] Dowson, D., History of Tribology, 2nd edition, Wiley, (1998).

[2]Bhushan, B., Introduction to Tribology, John Wiley & Sons, NY. (2002).

[3] Khonsari, M. M., Booser, R. E., Applied Tribology: Bearing Design and Lubrication, John Wiley & Sons, NY. (2001).

[4] Totten, G.E., Westbrook, S.R., and Shah, R.R., Fuels and Lubricants handbook: Technology, Properties, Performance and Testing, Vol 1, ASTM Manual Series; MNL 37 (2003)

[5] R. L. Jentgen. IEEE Transactions on Parts, Hybrids, and packaging, Vol. PhP-7, No. 2, June (1971)

[6] Ludema, K.C., Friction, Wear and Lubrication:A Textbook in Tribology, CRC Press LLC, FL, (1996)

[7] Brainard, W.A., NASA TN D5141 (1969)

[8] Sliney, H.E., Trib. Int. 15, 303 (1982)

[9] Braithwaite, E.R., Solid Lubricants and Surfaces, Clarendon, Oxford, (1964) 139,

[10] Prasad S.V., and Zabinski, J.S., Nature, 387 (1997) 761

[11] Muratore, C., and Voevodin, A.A., Annu. Rev. Mater. Res., 39 (2009) 297

[12] Hilton, M.R., and Fleischauer, P., Surf. Coat. Technol. 54-55 (19920 435

[13] Zabinski, J.S., Donley, M.S., Walck, S.D., Schneider, T.R., and McDevitt, N.T., Trib. Trans. 38 (1995) 894

[14] Scharf, T.W., Kotula P.G., and Prasad, S.V., Acta Materialia, 58 (2010) 4100-4109

[15] Teer, D.G., Wear 251 (2001) 1068

[16] Erdemir, A., and Donnet, C., eds., Tribology of Diamond-like Carbon Films: Fundamentals and Applications, Springer, 2008

[17] Scharf, T.W., Ohlhausen, J.A., Tallant, D.R. and Prasad, S.V., Journal of Applied Physics, 101 (2007) 063521-1 -063521-11

[18] Prasad, S.V., Michael, J.R., and Christenson, T.R., Scripta Mat. 48 (2003) 255

[19] Jungk, J.M., Michael, J.R., and Prasad, S.V., Acta Mat. 56 (2008) 1956

[20] Konicek, A.R., Grierson, D.S., Gilbert, P.U.P.A., Sawyer, W.G., Sumant, A.V., and Carpick, R.W., Phys. Rev. Lett. 100 (2008) 235502

[21] Grierson, D. S., Sumant, A.V., Konicek, A.R., Abrecht, M., Birrell, J., Auciello, O., Carlisle, J.A., Scharf, T.W., Dugger, M.T., Gilbert, P.U.P.A., and Carpick, R.W., J. Vac. Sci. Technol. B 25 (2007) 1700

[22] Briscoe B. J., and Tabor, D., Wear, 34 (1975) 29

[23] Bahadur, S., and Tabor, D., Wear, 98(1984) 1

[24] Dellacorte C., and Sliney, H.E., Lubric. Eng., 48 (1992) 877

[25] DellaCorte, C., Edmonds, B.J., and Benoy, P.A., NASA TM-210944, (2001)

[26] Zabinski, J. S., Sanders, J. H., Nainaparampil, J. and Prasad, S. V., Tribology Letters, 8 (2002)103-116

[27] Karch, J., Birringer, R., Gleiter, H., Nature 330 (1987)556-558

[28] Schiotz, J., Di Tolla, F. D. and Jacobsen, K. W., Nature 391 (1998) 561

[29] Zabinski. J. S., Corneille, J., Prasad, S. V., McDevitt, N. T. and Bultman, J. B., J. Mater. Sci. 32 (1997) 5313-5319

[30] Romanes, M., PhD Dissertation, Uni. of N. Texas (2008)

[31] Elam, J. W., Sechrist, Z. A. and Gordon, R. G., Thin Solid Films 414 (2002) 43-55

[32] Becker, S. J., PhD Dissertation, Harvard University (2002) 9

[33] Puurunen, R. L., J. of Applied Physics 97 121301 (2005)

[34] Kim, H., Lee, B. H. and Maeng, J. W., Thin Solid Films 517 (2009) 2563-2580

[35] Stewart, R. and Ahmed, R., Wear 253 (2002) 1132-1144

[36] Erdemir, A., Rolling-contact fatigue and wear resistance of hard coatings on bearing steel substrates. In: presented at 19th Int. Conf. on Metallurgical Coatings and Thin Films (April 1992)

[37] Wereszczak, A.A., Wang, W., Wang, Y., Hadfield, M., Kanematsu, W., Kirkland, T.P., and Jadaan, O.M., http://info.ornl.gov/sites/publications/files/Pub2425.pdf

CHAPTER 2

OVERVIEW OF SOLID LUBRICANT FRICTION AND WEAR NANOCRYSTALLINE OXIDE CERAMICS AND ATOMIC LAYER DEPOSITION

2.1 Solid Lubricant Tribology (Friction and Wear)

The word 'tribology' is derived from the Greek word *tribos*, meaning rubbing or sliding. Tribology is the science and technology of interacting surfaces in relative motion. It encompasses every aspect of friction, lubrication and wear. Tribology is an interdisciplinary field. Rather complex surface interactions in a tribological interface require knowledge of various disciplines, such as materials science/engineering, mechanical engineering, chemistry, physics, solid mechanics, and rheology.

2.1.1. Friction

Key to tribology is the frictional force, F, which is the lateral resistance encountered when two surfaces are in relative motion with each other. There is a relationship between the frictional force and the force or load acting normal to the direction of motion (L), known as the coefficient of friction (COF) or μ

$$COF(\mu) = \frac{F}{L} \tag{2.1}$$

The COF is not a material's intrinsic property but rather a system's property since it is a function of the applied load, interfacial temperature, sliding velocity and environment.

Usually, high COF is undesirable; however, it is essential in certain areas such as car tires that provide traction on the road and screws to hold construction materials together.

According to the classical theory of Bowden and Tabor,[1] friction force, F, is a product of the contact area (A) and the shear strength (τ) of the lubricant material (see Figure 2.1). Thus, the friction coefficient, μ, can be expressed by:

$$\mu = \frac{F}{L} = \frac{A \bullet \tau}{L} = \frac{\tau}{P_H} = \frac{\tau_o}{P_H} + \alpha \qquad (2.2)$$

where L is the normal force (load); P_H is the mean Hertz pressure; τ_o is the interfacial shear strength, a 'velocity accommodation parameter' which is a property of the interface; and α represents the pressure dependence of the shear strength. The constant 'α' is the lowest attainable friction coefficient for a given friction couple. In principle, a hard material with a soft skin ought to provide low friction coefficient by reducing τ_o and increasing P_H (low A).

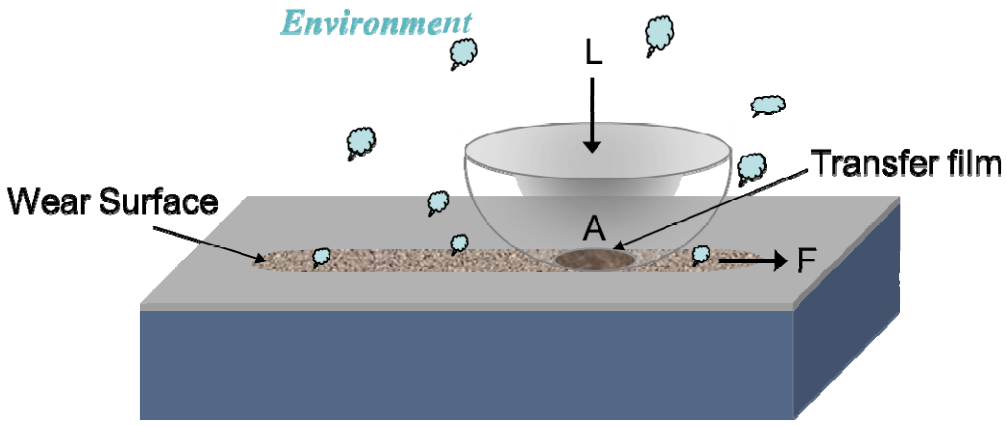

Figure 2.1: Schematic of a hemi-spherical pin sliding on a coated substrate. Tribology is a system's property, principally governed by contact mechanics and tribochemical (chemistry induced by sliding) reactions.

For a 'sphere-on-flat' elastic contact, which is known as the Hertzian elastic contact model, this friction coefficient can be expressed as:

$$\mu = \tau_o \pi \left(\frac{3R}{4E} \right)^{2/3} L^{-1/3} + \alpha \tag{2.3}$$

where R is the sphere radius and E is the equivalent Young's modulus. Instead of the Amontonian first law of friction, where μ is independent of L, the Bowden and Tabor analysis for Hertzian contacts predicts,

$$\mu \propto L^{-1/3} \tag{2.4}$$

Thus, when contact deformation is elastic, the friction coefficient will decrease with increasing normal load (or mean Hertz pressure). The linear relationship between $L^{-1/3}$ and μ (Eq. 2.3) has been experimentally verified for a number of solid lubricant coatings (see Figure 2.2).

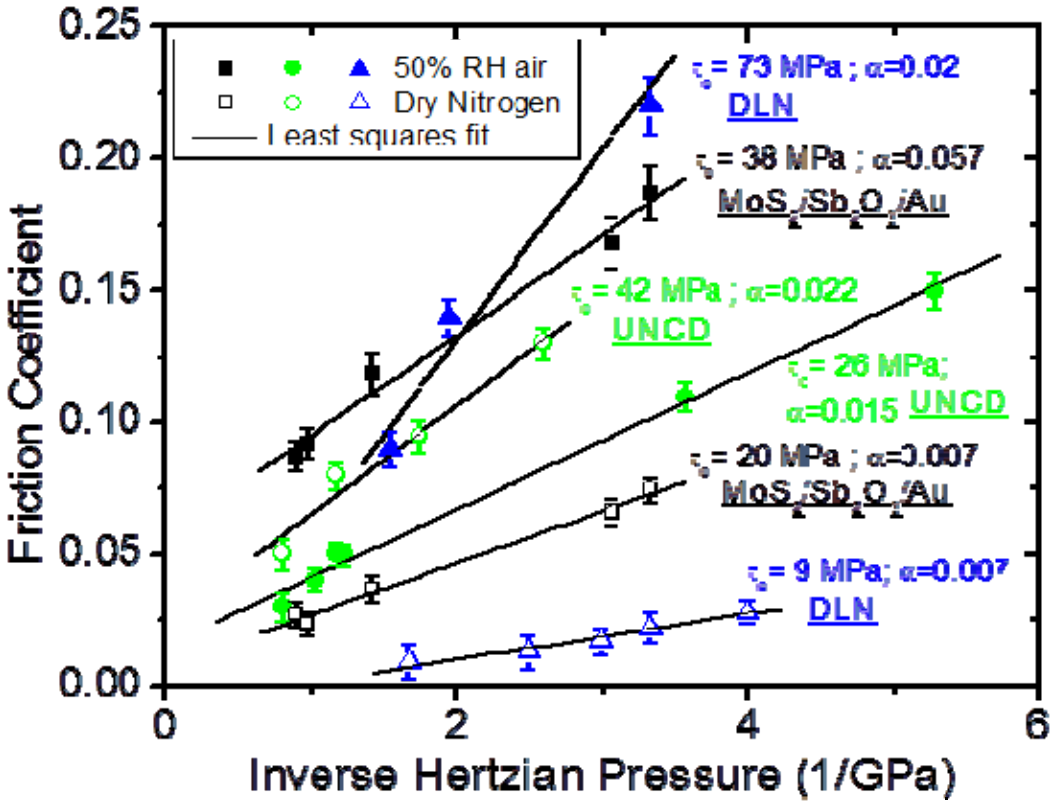

Figure 2.2: Linear regression fits for friction coefficient as a function of inverse Hertzian pressure fitted to $\mu=(\tau_o/P_H)+\alpha$ with values of shear strength (τ_o) shown for three low friction, environmentally-robust coatings: Si_3N_4 on DLN, UNCD coated Si_3N_4 on UNCD, and Si_3N_4 on $MoS_2/Sb_2O_3/Au$ in both dry nitrogen and humid air [T.W. Scharf private communication].

For thin and soft coatings, the pressure is primarily supported by the substrate and increasing the substrate modulus and hardness will decrease the contact area for a given normal load. Thus, the ideal scenario for achieving low friction is to have an elastically stiff and hard substrate support the normal load and keep the contact area small, while the surface coating provides shear accommodation and reduces junction strength, until the substrate begins to yield and plastically deform.

Friction does not just rely on physical and mechanical properties of individual materials that come into contact; instead, as mentioned earlier, it is a system's property involving interactions within pairs of contacting surfaces and between them and the environment. Many tribological contacts result in transfer of material from the coating surface to the counterface (such as the hemispherical pin shown schematically in Figure 2.1), plus surface chemical reactions with the surrounding environment, resulting in wear surfaces whose chemistry is significantly different from the bulk. Environment plays a significant role in determining the tribological performance of coatings that are designed to mitigate friction. Coatings that give extremely low friction and long wear life in one environment can fail to do so in a different environment.

2.1.2. Wear

Wear is the surface damage or removal of material from one or both of two solid surfaces. It occurs when solid surfaces are in sliding, rolling or impact motion relative to one another. First, during relative motion, material on the contacting surface may be displaced so that properties of the solid body, at least at or near the surface, are altered, but little or no material is actually lost. Later, material may be removed from a surface and may result in the transfer to the mating surface or may break loose as a wear particle. Thus, wear damage often precedes actual loss of material. It should be emphasized that damage due to material displacement on a body, with no net change in weight or volume, also constitutes wear. Wear, as previously discussed friction, is not a material property, but rather a system response. Operating conditions, such as contract stress, environment,

and velocity, also affects interfacial wear. In addition, it is not necessarily true that high-friction interfaces exhibit high wear rates and vice versa.

Wear is the major cause of material wastage and loss of mechanical performance, thus any reduction in wear can result in considerable economical savings. There is a process by which wear volume loss occurs, known as the wear mechanism or mode. If wear particles are formed, even though these may greatly influence the wear mechanism and wear rate, wear volume loss will occur only if the particles are lost from the local surface. Matthews et al.[2] categorized wear mechanisms into two groups; mechanical wear mechanisms and physical-chemical wear mechanisms.

Mechanical wear mechanisms include:

- Ploughing/cutting by abrasion, erosion, etc, whereby (micro)chips of material are formed through ploughing of a harder surface (or third body) in a softer one. Abrasive wear occurs when asperities of a rough, hard surface or hard particle slide on a softer surface and damage the surface by plastic deformation or fracture.
- Extraction of material by adhesive wear, in which wear particles are formed by being pulled out from the surface. Adhesion (or bonding) occurs at the surface roughness asperity (protrusion) contacts at the interface, and these contacts are sheared during sliding, which may result in detachment of a fragment from one surface (usually the softer) and adhering to the other surface (the harder one). Subsequently, the transferred fragments may form loose particles (ejected or re-circulated back and forth in the contact).

- Plastic deformation/compaction of material by combination of abrasive and adhesive wear, in which material on the surface is plastically deformed and flowing away from the contact area or compacted within the contact area to potentially form a third body (transfer film). If the wear tribo-couple consists of a hard and soft material, then the hard asperities or hard particles result in the plastic flow of the softer material.

Physical-chemical wear mechanisms include:

- Chemical wear in which volume is lost by chemical reaction. Oxidative and/or corrosive wear may also occur where the oxidized or corroded material (layer), respectively, are subsequently lost. Thus chemical wear requires both chemical reaction (corrosion and/or oxidation) and interfacial contact.
- Physical wear in which volume is lost through dissolution, diffusion or evaporation.

Other wear mechanisms/modes include fatigue wear, such as rolling contact fatigue discussed in Chapter 5, impact/erosive wear, and fretting (oscillatory wear). In practice, different combinations of mechanisms will occur together, so that the above mechanisms rarely occur independently. During the course of the wear process, the relative contributions of these mechanisms change in time as a result of changes in the local conditions within the tribological system. This may be regarded as the single largest problem with wear prediction, thus predicting how the system will change in time and, therefore, how the nature and contribution of each acting wear mechanism will change.

2.1.3 Role of Solid Lubricants

Finally, lubrication by solid is also defined as the process employed to reduce wear of one or both surfaces in contact by transmitting frictional stresses between the opposing surfaces. Solid lubricants are applied to separate the two surfaces and reduce their friction and wear, sometimes accomplished by forming a protective third body transfer film. When the surfaces of two bodies are in close proximity to each other, they first come into contact at the peaks commonly known as asperities. During the relative motion between the two surfaces, friction may be experienced between the asperities of the different surfaces and the resulting energy dissipation will be due to the interaction of these asperities. This interaction could result in either plastic or elastic deformation based on the applied stress and material properties of the surface. *A* changes as the interaction between the surfaces continues, this is because the contact conditions continue to change due to the plastic deformation. According to equation 2.2, with the change in the *A,* the COF will also change. The primary purpose of a lubricant is to separate these contacting surfaces (asperities) and thereby mitigate friction and wear.

2.2 Oxide Ceramics

Oxide ceramic materials are formed when a metal reacts with oxygen. They can either form a covalent bond or ionic bond depending on the difference in electronegativities (EN). Based on Pauling's ionicity fraction, similar EN between the metal and oxygen will result in more covalent bonding character versus a larger difference in EN, will result in more ionic bonding character. There are two forms of oxide ceramics: the single and the multicomponent oxides. The multicomponent oxides

refer to those that contain more than one cation type in the structure and the single oxides have only one cation type in the structure (binary oxides). In general, both ionic and covalent bonds have the tendency to have large bond and lattice energies; the large bond/lattice energies allows these materials to exhibit high strength, high hardness, chemical and thermal resistance. Traditional oxide ceramics (micro/macrocrystalline and single crystals) are excellent engineering materials for demanding applications requiring these characteristics, but they exhibit inherent brittleness at low temperatures, and, hence they have very low resistance to loads (i.e. low fracture strength and toughness). This low strength is due to the strong bonds between the metal and oxygen, thus it is difficult for dislocations to move to cause any crystalline slip in micro/macrocystalline and single crystal oxides in addition to very few number of slip systems and large Burgers vectors. Brittle fracture is the typical failure mode in these materials. This occurs when a critical stress is reached at a weak point (flaw) and a micro-crack is formed and rapidly travels throughout the material, causing failure. Very little or no plastic deformation occurs in the surrounding areas of the crack. When cracks propagate in oxide ceramics, large wear particles that are abrasive are normally formed during sliding contacts. High friction and significant wear by a third body abrasive wear mechanism are observed during the sliding and this leads to device or equipment failure.[30]

Even though, oxide ceramics have low fracture toughness at ambient temperatures, their demand in the area of tribological applications is increasing. They have been used as mechanical seals, prosthetic devices and ball bearings as well as becoming reliable materials for a wide range of applications in extreme conditions.

However due to their brittleness, there is always a significant amount of wear associated with their use. Thus at both ambient and elevated temperatures, if oxide ceramics could be engineered to plastically deform during sliding without any catastrophic failure, they could become very reliable materials for a wide range of tribological applications.[30]

2.2.1 Tribological Behavior of Bulk and Microcrystalline Oxide Ceramics

Materials that have grain sizes less than 100 nanometers in all dimensions are considered as nanocrystalline materials. On the other hand, if the grain size of a ceramic material is more than 1 micron, they are considered to be bulk oxide ceramics. Bulk oxide ceramics typically have polycrystalline crystal structures and often times are not reliable for many tribological applications under dry sliding conditions. Both the friction and wear coefficients of bulk oxide ceramics are too high to be practical for most tribological applications. Several investigators have concluded that microfracture is by far the greatest source of wear in bulk oxide ceramic materials.[3,5] This is because, unlike metallic materials, most ceramics show essentially no sign of plastic elongation. The inherent brittleness of these materials is thought to originate from their usually limited number of slip systems available for plastic flow and the inherent difficulty of dislocation glide in their structures. This is the reason for the abrasive nature of the wear debris. A major cause of microfracture in bulk oxide ceramics is related to internal volume defects. Despite all the technological advances made in their fabrication, bulk oxide ceramics still contain many internal defects (e.g., flaws, voids, inclusions, weak grain boundaries). During sliding contact, these defects act as stress concentration points. Under the

influence of normal and tangential forces, micro-cracks can initiate from these defects, where dislocations may sometimes pile up and thus block slip-band propagation.[4]

Rainforth reviewed the wear behavior of bulk oxide ceramics and categorized wear in bulk oxide ceramics into two regimes (i.e. mild or severe).[5] Most ceramics exhibit a wear transition from mild to severe wear, at some critical load. This transition is characterized by an increase in wear, often several orders of magnitude, and is associated with the onset of brittle fracture at the surface. Hence at the severe regime, there is a rapid failure. More studies are conducted at the transition from mild to severe wear in order to prevent its occurrence. The mild wear regime is defined by the smoothing of the worn surface and the formation of third body transfer films. In order to increase the resistance to fracture in oxide ceramics, structural engineering is needed by refining grain size, adding defects, etc. Rainforth has targeted three strategies with this approach: (a) reduction in grain size with improved density in an attempt to reduce the flaw size within the material; (b) formation of duplex structures, and, (c) improvement in toughness by a transformation toughening mechanism with applicability to zirconia. All these strategies were looked into in this dissertation at the nanoscale regime. In the case of (a), all the crystalline films exhibited nanoscopic grain sizes. With respect to (b), a duplex geometry was processed using ZnO/ZrO_2 and $ZnO/Al_2O_3/ZrO_2$ nanolaminates. For (c), ZrO_2 was implemented as a relatively high toughness/load bearing layer in order to prevent brittle crack formation in the nanolaminates. All of these approaches will be further discussed in this dissertation.

2.2.2 Plastic Deformation in Nanocrystalline Oxides

In general, when a material is mechanically stressed, it will exhibit the following sequence in response: elastic deformation, plastic deformation, and fracture. In the case of elastic deformation, when stresses are no longer applied, the deformation is reversed and the material returns to its original shape. On the other hand, if the deformation is not reversible when a stress is no longer applied, plastic deformation occurs. In this case, there is a change in the material's structure over all size and length scales, e.g. from atomic bonds broken to dislocation glide to grain boundary (GB) deformation/sliding. The plastic deformation behavior is from the motion of a number of individual dislocations on specific crystal lattice planes along certain directions (slip systems), and just like in mechanical loading, is relevant in tribological contacts where there is crystalline slip.

At room temperature, oxide ceramics are brittle, which is due to difficulty in dislocation motion (slip) because a) nearest neighbors of like charge (cations and anions) resist motion (repulsion), b) larger Burgers vector slip distances, and (c) there are few total slip systems (made up of partial dislocations with smaller slip steps). Unlike metals whose ductility is directly related to the ease of dislocation, the bonding in ceramic oxides makes slipping process difficult and the dislocations are essentially immobile.[6] Furthermore, larger grain size oxide ceramics have poor ductility due to the aforementioned limited number of slip systems and it is difficult to activate them without the introduction of thermal energy in these materials. Thus plastic deformation is rarely observed in oxide ceramics at ambient temperature. The question now is how can oxide

ceramics be made to exhibit significant plastic deformation under tribological stresses at both low and high temperatures without brittle fracture?

Ductility in nanocrystalline ceramics was first reported by Gleiter et al.[7], who observed that TiO_2 and CaF_2 plastically deform at low temperatures by reducing their grain size to a few nanometers. They confirmed that this ductility seemed to have originated from the diffusional flow of atoms along the intercrystalline interfaces. Gleiter et al. concluded that the diffusional creep rate of a polycrystalline material may be enhanced by reducing the crystal grain size and by increasing the grain boundary diffusivity. Schiotz et al.[8] with the help of computer simulations also reported that most of the plastic deformation occurring in nanocrystalline copper (with possible implications to nanocrystalline ceramics) was due to a large number of small "sliding" event of atomic planes at the grain boundaries with only a small fraction of the deformation being caused by dislocation activity in the grains. Their theory is a critical grain size, d, which is also known as the cross-over grain size, is responsible for the mechanism change from dislocation motion (Hall-Petch) to grain boundary motion (inverse Hall-Petch). These two studies proposed that the Inverse Hall-Petch effect, in which the deformation happens along nanocrystalline grain boundaries instead of the classical microcrystalline Hall-Petch effect, in which the deformation classically happens by yield stress was responsible for the observed plastic deformation. For conventional grain size materials (1-100 μm diameter) the empirical Hall-Petch equation predicts that

$$\sigma_y = \sigma_o + kd^{-1/2} \tag{2.5}$$

where σ_y is the yield strength, σ_o is a friction stress below which dislocations will not move in a single crystal, k is a constant and d is the grain size. Thus as the grain size is refined, the strength increases as $d^{-1/2}$ and can, potentially, reach very high values as there is a greater total grain boundary area to stop dislocation slip thereby increasing the strength of the material. Once the grain size of materials are reduced to the nanoscale, these materials may deform by the inverse Hall-Petch phenomena in which there is grain boundary activity so that finer grained materials would be softer and more deformable. Differences from the classical Hall-Petch behavior at the nanoscale are not unexpected since the traditional explanations for this behavior involve a large array of dislocations piled up at the grain boundary. The length of such a pile-up is of the order of magnitude of the grain diameter. At nanoscale grain sizes, applied stresses required approach or exceed theoretical strength. At these small grain sizes, the dislocation forces are sufficient to eliminate dislocations by moving them into the grain boundaries.[9]

This inverse Hall-Petch effect has generated controversy with only a few sets of results obtained to date, which are all for metals. Koch[9] and coworkers concluded in 2001 that, at the time of their work, only two experimental data sets (Erb et al.[10] and Narayan et al.[11]) truly demonstrated the inverse Hall-Petch effect. Their findings were that, most of the experiments that reported the inverse Hall-Petch effect had samples that exhibited clear artifacts and there were also problems with the accurate determination of grain size and its distributions. Nanocrystalline metals of aluminum,[12] copper[13] and nanocolumnar nickel[14] have been studied by computer simulations and the inverse Hall-Petch effect was observed in these materials. In general, there is a growing consensus that the apparent

anomalous dependence of yield stress on grain size can be rationalized by the activation of deformation mechanisms taking place at the grain boundary which compete with crystal plasticity and become the dominant operative dissipative deformation mechanism when grain sizes are sufficiently small.[15]

In 1998, Muller et al.[16] analyzed the plasticity of nanocrystalline ZrO_2 prepared by a laser evaporation. The grain size of the ZrO_2 was determined to be in the range of 57 and 110 nm. In their study to determine the applicability of these nanoscale powders for producing ceramics with nanocrystalline microstructure, a uniaxial pressing and pressureless sintering of yttria partially stabilized tetragonal (YTZ) to a density of more than 98% determined that, this powder shows a superplastic behavior. In 1999, Sagalowicz et al.[17] studied the microstructure and defects of wurtzite isostructures ZnO and AlN thin films. Both films exhibited the {0002}- preferred orientation, or c-axis basal plane orientation. They also reported ZnO exhibited a high density of both planer defects and dislocations (double and single stacking faults of 10^{12} cm^{-2} in density), but not AlN (due to small grain size). They concluded that a large x-ray diffraction peak width ($> 0.3^{o}$) was exhibited by the (0002) plane, which originates from non uniform strain or lattice imperfections. These lattice imperfections include large angle grain boundaries, planer defects and dislocations.

Ovid'ko[18] and coworkers in 2007 reported that, GB sliding emanates to the formation of dipoles of edge disclinations (linear rotational defects). The strengths of the formed disclinations are equal in magnitude to the misorientation angles of the tilt boundaries involved in GB sliding, and the dipole arms (the distance between the

disclinations forming a dipole) are equal in magnitude to the displacements of the corresponding GBs. In 2008, they[19] proposed a model that described the influence of GB sliding on crack growth in nanocrystalline ceramics. This was based on the fact that brittleness in nanocrystalline ceramics decreases due to grain boundary sliding. Thus the GB sliding caused by an external stress and by concentrated stresses near the crack tip brings about the formation of an array of disclination dipoles, which can partially relieve the elastic stresses near the crack tip. GB sliding can increase the critical crack length (above which the catastrophic growth of cracks begin), and hence increase the fracture toughness of the ceramic. They concluded that, the increase in the critical crack length and the related improvement of the fracture toughness are very significant at small nanograin sizes and misorientation angles of GBs. In 2007, Mo et al.[20] in their quest to enhance ductility and toughness in nanocrystalline ceramics at high strain-rates used computer simulations based on molecular dynamics (MD). This technique is suited for the study of high strain-rate limits of deformation and to unravel its atomistic details. They performed MD simulations to elucidate the tensile deformation mechanism of nanocrystalline SiC at a strain rate of 10^8 s^{-1}. Their study revealed a suppressed cavitation in the absence of diffusion and in the absence of dislocation activity in the grains. This suppressed cavitation is primarily due to the reduction of the grain size and governed by plastic flow along GBs, which delays localization of deformation. They showed in their work that nanocrystalline SiC exhibits increased ductility and toughness without compromising its strength. Jian et al.[21] in 2008 studied the nanomechanical behavior of pulsed laser deposited (PLD) ZnO thin films that were deposited on different substrates.

They demonstrated that even though the normal load was increased from 0.02 to 5 mN during a friction test, the coefficient of friction almost remained constant into the early period for three of the substrates [(0001) 6H-SiC, c-sapphire, a-sapphire]. The COF for these films were 0.31, 0.28 and 0.25 respectively. With the increase in load, they reported that despite the increase in plastic deformation of ZnO, which might have resulted in grooving during scratch, no cracking of the thin films took place. They associated the small fluctuations in the COF values to point-on orientation of the tip, the layered structure of the thin films or nanoscale fracture events that might have occurred during the test. However, they acknowledged that there was no catastrophic wear or delamination of the thin films, thus the COF values corresponded to a mild wear regime.

Lin et al.[22] in 2009 also reported on ZnO thin films that were prepared by a sol-gel method both on glass and silicon substrates. They studied the interrelationships between crystal structure, surface morphology and the tribological behavior of these films by annealing them to different temperatures (450 to 800^{o}C). They observed an increase in grain size with an increase in annealing temperature by measuring the broadening of the ZnO (0002) peak. They also mentioned that the (0002) peak shifted with the temperature increase, which was correlated to the existence of residual stress between the ZnO film and the silicon substrate. The tribological behavior of the films was determined by using a normal load of 0.5 gf from a Si_3N_4 ball. The as deposited films on glass had higher COF than the annealed films with COF values ranging from 0.61 to 0.36. On Si substrates, the COF of as deposited and 450^{o}C were much higher compared to the films annealed at higher temperatures with the COF ranging from 0.52 to 0.24. The relatively high friction

for the as deposited film and the 450^{o}C film was associated with abrasive plowing of the wear debris present at the sliding interface. They concluded that at relatively low annealing temperatures, the transformation of the film microstructure was insufficient to result in the improvement of mechanical properties (hardness and elastic modulus).

Based on the current literature, it has been demonstrated that normal brittle polycrystalline ceramics could become ductile if their grain size is reduced to tens of nanometers and less. In this dissertation, this phenomenon is used in the promotion of lubricity and plasticity in nanocrystalline ZnO coatings subjected to tribological contacts as well as using advanced characterization techniques to determine the chemical and structural mechanisms responsible for friction and wear.

2.2.3 Lubricious Oxide Materials

Normal oxide films made of metallic adhesives have little or no capacity of self-lubrication at ambient temperatures due to their high brittleness and large amounts of faceted wear debris. At ambient temperatures, it is very difficult to activate any dislocation motions since ions of like charges repel motion and Burger vector (unit of slip) distances are large, hence these oxides are unable to plastically deform and are brittle. Their surfaces are generally inert and typically do not form strong adhesive bonds like metals in tribological contacts. But at high temperatures (> 0.5 $T_{melting}$), oxides have been used as solid lubricants due to their ability to plastically deform. Bulk, microcrystalline ZnO films are known to have very high COF ($\mu \sim 0.7$), as reported by Zabinski et al.[23] who also determined that PLD ZnO films exhibit low COF ~ 0.2 and long wear lives greater than 10^6 cycles at room temperature. The films were highly

textured, with the (0002) plane being the most dominant peak. The ZnO films exhibit columnar grains with widths of ~20 nm and also contained subgrains within the columns (defective mosaic substructure). They concluded that the stoichiometry and microstructure of the ZnO films could be controlled by adjusting the substrate temperature (low T) and oxygen partial pressure during the pulsed-laser deposition. They also suggested that this study could be repeated for other oxides to provide good tribological properties at room temperature. In 2000, they[24] proposed that the mechanism for the increase in plasticity was due to the reduction of the grain size within the oxide coating as shown in Figure 2.3.

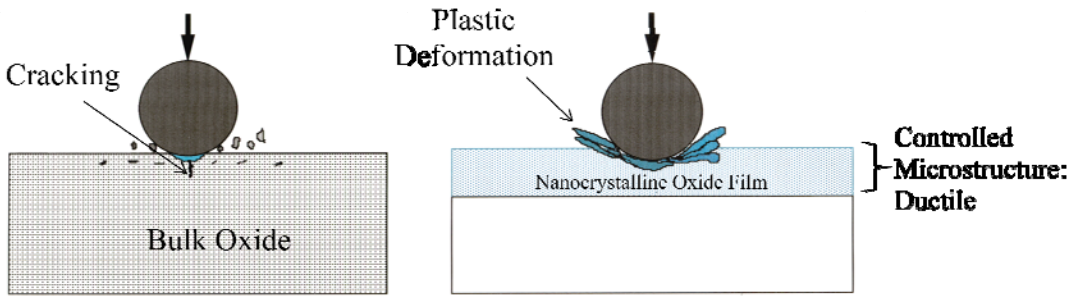

Conventional Brittle Oxide Ductile Oxide Film

Figure 2.3: Schematic illustration of wear mechanisms in a conventional brittle oxide and a ductile nanocrystalline oxide film.[23]

In 2008, Romanes[30] reported low coefficient of friction values of approximately 0.22 after 10,000 cycles for ZnO/Al_2O_3 nanolaminates deposited by atomic layer deposition at different deposition temperatures. All friction measurements were done at room temperature under low loads of 10 and 25 grams. The nanolaminate films deposited at temperatures of 200, 250 and 300^{o}C were varied from 1 bilayer to 64 bilayers with the

Al_2O_3 and ZnO layers alternating. The Al_2O_3 layer was deposited first on a silicon substrate followed by the ZnO layer. She proposed that laminating the ZnO with Al_2O_3 was beneficial for the enhancement of the low surface energy (0002) preferred orientation thus suppressing other competing higher surface energies such as the (10-10) and (10-11) grains. Romanes concluded that, the 8-bilayers deposited at 200^{o}C exhibited the lowest coefficient of friction (~0.19) and this was due to the low surface energy (0002) preferred orientation, smaller grain size (< 20 nm), sufficient thickness of the top ZnO layer and the ability of the Al_2O_3 layers to aid in load transfer and act as a pathway to dissipate energy in preventing crack formation. The 16 and 64 bilayers showed the highest coefficient of friction values among all the nanolaminates. Romanes work made use of high resolution transmission electron microscope to study plastic deformation mechanisms inside the wear tracks. She observed that during sliding, there is a reorientation of the nanocrystalline surface layer that contributes to the friction reduction. This velocity accommodation mode was shown to be the result of progressive refinement of the ZnO grains that proceeds from crystalline to amorphous. This layer is soft, ductile and easily smears along the wear track resulting in lower interfacial shear and hence low friction.

It is obvious that nanocrystalline grain size oxide ceramics could be considered as very good candidates to be lubricious at low temperatures. More detailed structural and chemical studies need to be carried out to determine friction and wear mechanism in lubricious oxides.

2.3 Atomic Layer Deposition

Atomic layer deposition (ALD) is a variant of the chemical vapor deposition (CVD) technique, suitable for manufacturing ultra-thin films with thickness down to a fraction of a monolayer. ALD was developed and introduced worldwide under the name of atomic layer epitaxy (ALE) in the late 1970s by Suntola and co-workers.[25] The motivation behind its development was the desire to make thin electroluminescent (TFEL) flat panel displays. But after its successful introduction, ALD has found various applications (during the 1990s and 2000s) in the areas of compound semiconductors (especially the III-V compounds), solar cells, microelectronics, optics, protective applications, and gas sensors. Currently, ALD is considered as one of the most promising thin film deposition techniques for enabling nanoscale device fabrication. The major driving force for the recent increase is a direct consequence of the ever-scaling down of device dimensions and the increasing aspect ratios in microelectronic devices. This is also demonstrated by a rapidly increasing number of new materials, processes and reactor designs as well as users in both industry and academia.

ALD has the capability to coat extremely complex shapes with a conformal material layer of high quality capability unique among thin-film deposition techniques. The technique offers unprecedented control of thickness, uniformity, quality and material properties monolayer films that are very thin. One of the features of ALD technology that distinguishes it from other thin film deposition techniques is its self-limiting nature. The chemistry is such that the entire surface is reacted to completion, disallowing further reactions to continue to take place.[26,27,28]

ALD growth is in the form of a cyclic process where there is a sequential use of self terminating gas-solid reactions. This growth is based on the following unique features:

- A self-terminating reaction of the first reactant (reactant A)
- Evacuation or purging of the non-reacted reactants and the gaseous reaction by-products
- A self-terminating reaction of the second reactant (reactant B)
- Evacuation or purging of the reactants and byproduct molecules from the chamber with inert gas

Steps 1 - 4 are known as a reaction cycle. Steps 1 and 3 are normally referred to as half reactions of an ALD reaction. One ALD reaction cycle adds a given amount of material to the surface, referred to as the *growth per cycle* (GPC). To grow a material layer, reaction cycles are repeated until the desired amount of material has been deposited.[29] ALD and CVD may have many similarities but there is a clear distinctive feature of the ALD which lies in the self-limitation for precursor adsorption and alternate, sequential exposure of precursors and reactants. In other words, in contrast to other deposition techniques, ALD proceeds through self-limitation in reactions between chemicals and substrates. As the film growth proceeds in a self-limiting manner, each cycle deposits exactly the same amount of material, and thus the film thickness may be accurately controlled simply by the number of deposition cycles. For example, for AB binary material, these half reactions will generally follow:

1^{st} reaction: surface + $AB_{(g)}$ → surface: A + $B_{(g)}$

2^{nd} reaction: surface: A + $CD_{(g)}$ → surface: AC + $D_{(g)}$

One ALD cycle is illustrated in the two half reactions above. Ideally, one reaction cycle will add a given amount of AC to the deposited film. A desired thickness of the material can be deposited by the number of required cycles. ALD can also be used to deposit single elements, in such situations the 2^{nd} reaction maybe a pulse of sacrificial precursor, a plasma exposure or a thermal spike to take away unwanted molecules from the surface allowing it to be reactive for the next 1^{st} reaction. Both nitrogen and argon are used as purging and carrier gas to separate the two half reactions.[30] The purge (or evacuation) period removes all the excess precursor molecules and volatile byproducts leaving only the reacted AC amount on the surface.[32] ALD cycle times range from sub second to many seconds depending on sample geometry and chemistry.

ALD's unique features allow the growth of highly conformal films with accurate thickness over large areas. The ALD benefits are listed below:

- Accurate and simple thickness control
- Large-area compatibility
- Large-batch compatibility
- Excellent conformality
- No problems with inconsistent vaporization rates of solid precursors
- Good reproducibility
- Straight forward scale-up
- Capability to produce sharp interfaces and superlattices

- Possibility to interface modification
- Favors precursors highly reactive toward each other, thus enabling effective material utilization
- High quality materials are obtained at low processing temperatures, and
- Capability to prepare multilayer structures in a continuous processing temperature window.[32]

Most of the ALD processes reported are based on the above described exchange reactions between molecular precursors. Another possible reaction type is additive with elemental precursors but because only a few metals are volatile enough, the applicability of these reactions is limited. In majority of the ALD processes reported, the reactions are activated only thermally under isothermal conditions. The alternate pulsing is definitely the most characteristic feature of ALD but almost as distinctive is the self-limiting growth mechanism. However, some deviations from the absolutely self-limited growth conditions may be accepted with certain precautions. A common misconception is that ALD growth always proceeds in a layer-by-layer manner, but this is often not the case as only a fraction of a monolayer may be deposited in each cycle. Reasons for the less than a monolayer per cycle growth are the limited number of reactive surface sites, and the steric hindrances between bulky ligands in the chemisorption layer. Another misconception is that ALD would produce atomically smooth films. This indeed may often be the case with epitaxial or amorphous films, but the nucleation and grain growth involved in the formation of polycrystalline films usually leads to a measureable surface roughness which increases along with film thickness. Practice has shown that ALD made

films often, though of course not always, possess superior quality as compared with films made by other methods at the corresponding temperatures. This can be related to the fact that in ALD each monomolecular layer reaction step is given enough time to reach completion while in other methods the continuous growth may prevent this by covering the unreacted species with new deposits. Many ALD processes may be performed over a relatively wide temperature range. Therefore, a common growth temperature is often found for different materials, thereby making it possible to deposit multilayer structures in a continuous manner.

The major limitation of ALD is evidently its slowness since at best, only a monolayer of the film is deposited per one cycle. Growth rates of 100-300 nm/hr obtained are very typical. However, the low growth rate does not mean low productivity. The low growth rate is compensated for by the good large-batch and large-area processing capabilities of ALD. Additionally, due to the continuous down scaling in dimensions, film thicknesses have shrunk down to a level wherein ALD is competitive with other deposition techniques. One other limitation to the widespread use of ALD has been the lack of good and cost-effective processes for some important materials. Some of these materials include metals, Si, SiO_2, Si_3N_4 and several ternary and multicomponent materials. There is also the limitation of the number of compatible precursor compounds. For a precursor to be ALD compatible, there are some general requirements for a good ALD precursor which include the following:

- Sufficient volatility at the deposition temperature
- No self-decomposition (thermally stable) allowed at the deposition temperature

- Aggressive and complete reactions
- No etching of/and not soluble in the film or substrate material
- No dissolution into the film or substrate
- Un-reactive volatile byproducts
- Sufficient purity
- Availability at a reasonable price
- Easy to synthesize and handle
- Nontoxic and environmentally friendly.[31,32]

According to the principles of ALD, each gas-solid reaction must be saturating by nature, and must be allowed to saturate on the surface. The type of saturation gas-solid reactions that may result in the bonding of the compound reactant onto a solid surface is classified as follows.

a. Ligand exchange
b. Dissociation and
c. Association

These mechanisms can occur simultaneously until saturation is reached. But of these three mechanisms, ligand exchange would often be preferred, because its equilibrium can be driven towards the product by removing the gaseous reaction products. When a compound reactant chemisorbs on a solid substrate, saturation of the surface with adsorbed species is typically caused by either of two factors; steric hindrance of the ligands and limited number of bonding sites. The former is related to the shielding of reactive sites by ligands of chemisorbed species making them inaccessible. This is most

likely for larger precursor molecules and those having large side groups. The latter occurs when the number of bonding sites on the surface is less than required for achieving a full ligand coverage. Although space remains on the surface, no accessible bonding sites are available.[31]

2.3.1 ALD Oxide Films

ALD oxide film studies have often dealt with growth mechanism investigations, but also structural properties of the films have been of interest. ALD is generally suited for the deposition of oxide thin films and overlayers for various applications. ALD oxide films have found industrial applications as dielectrics in electroluminescent thin film displays, but in the future gate oxides for MOSFET transistors will also perhaps be processed by ALD. The oxide films are deposited when an oxygen source is reacted with a volatile metal source, water is most frequently used as the oxygen source. Other oxygen sources that are employed include H_2O_2, O_2, O_3 as well as oxygen plasma. Ozone is a strong oxidizer producing dense films and furthermore for some weakly reactive precursors, such as the β-diketonates, ozone (or H_2O_2) remains the only alternative to obtain the metal oxides and at the same time reduce the impurities to a reasonable level.[32,15] There has also been a multicomponent oxides deposited by ALD, examples are $SrTa_2O_6$ or ferroelectric $SrBi_2Ta_2O_9$ which were deposited by plasma enhanced ALD (PEALD). In this study, however, the concentration is on binary oxides namely ZnO, ZrO_2 and Al_2O_3.

2.3.2 ALD ZnO

Zinc oxide (ZnO) is one of the typical transparent conducting oxides with a number of attractive characteristics. It is a direct and wide bandgap semiconductor material (E_g = 3.4 eV) and has a variety of potential applications. Zinc oxide crystallizes in three forms: hexagonal wurtzite (B4 type), shown in figure 2.4, cubic zincblende, and the rarely observed cubic rocksalt. The wurtzite structure is most stable and thus most common at ambient conditions. The zincblende form can be stabilized by growing ZnO on substrates with cubic lattice structure. In both cases, the zinc and oxygen are tetrahedrally coordinated. The rocksalt structure is only observed at relatively high pressures ~10 GPa. The hexagonal lattice (space group $P6_3mc$) has lattice parameters a = 0.3296 and c = 0.52065 nm. The structure of ZnO can be simply described as a number of alternating planes composed of tetrahedrally coordinated O^{2-} and Zn^{2+} ions, stacked alternately along the c-axis. The tetrahedral coordination in ZnO results in non-central symmetric structure and it is responsible for the piezoelectricity and spontaneous polarization. It is also a key factor in crystal growth, etching and defect generation. The four most common face terminations of wurtzite ZnO are the polar Zn terminated (0001) and O terminated (000-1) faces (c-axis oriented), and the non-polar (11-20) (a-axis) and (10-10) faces which both contain an equal number of Zn and O atoms. The most common polar surface is the basal plane.[33,34]

Many deposition techniques have been employed to synthesize ZnO thin films. Some of these techniques include RF sputtering technique, physical vapor deposition technique (PVD), pulsed laser deposition (PLD) technique, and atomic layer deposition

(ALD) technique.[35,36,37,38,39] Among these various techniques of ZnO film deposition, ALD can deposit a film in a surface-controlled manner with layer-by-layer growth. Several metal precursors have been employed in synthesizing ALD ZnO, these include dimethyl zinc, zinc chloride, zinc acetate and diethyl zinc. Of all these, diethyl zinc (DEZ, $Zn(CH_2CH_3)_2$) is the most common precursor used, which was also employed in this dissertation. As an oxygen source, to react with the volatile metal source, water (H_2O) is most frequently used. Other oxygen sources used include H_2O_2, O_2, O_3 as well as oxygen plasma. Ozone (H_2O_2) is a strong oxidizer producing dense films, furthermore for some weakly reactive precursors, such as β-diketonates. Ozone remains the only alternative to obtain the metal oxides and at the same time reduce the impurities (reaction by products) to a reasonable level.[40]

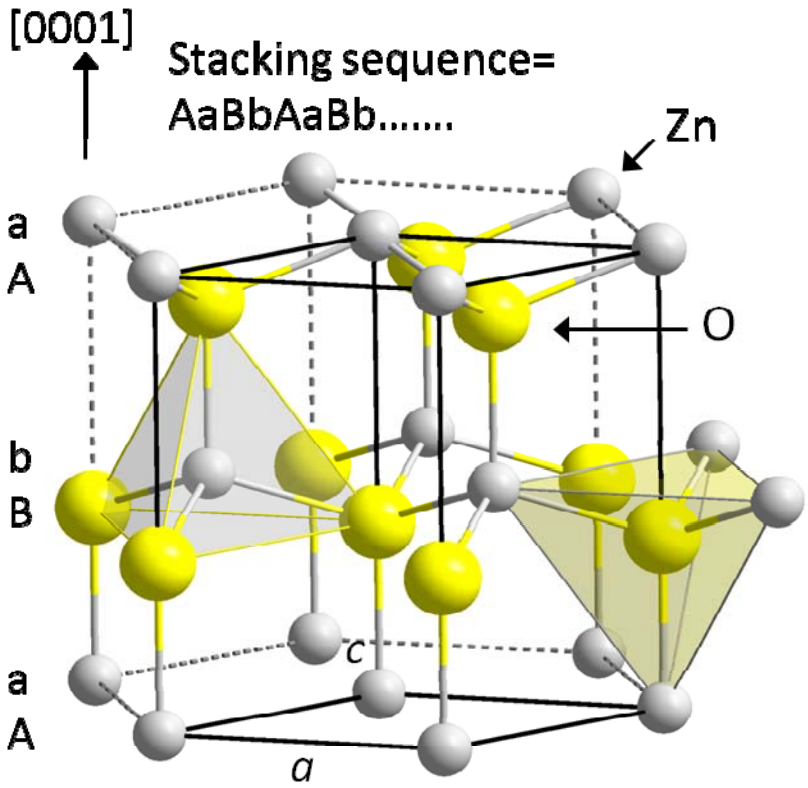

Figure 2.4: ZnO structure (wurtzite structure).

Deposition temperature plays a very important role in what crystal orientation is the most dominant when growing ZnO film by ALD technique. For temperatures less than 200°C, (10-10) texture is observed, and at temperatures of 200°C or higher, (0002) texture is observed.[41,42,43] The two half reaction that occur for ALD ZnO when DEZ and H_2O are used are found below:

$$ZnOH^{\dagger} + Zn(CH_2CH_3)_2 \rightarrow ZnOZn(CH_2CH_3)^{\dagger} + C_2H_{6(g)}$$

$$ZnOZn(CH_2CH_3)^{\dagger} + H_2O \rightarrow ZnOH^{\dagger} + C_2H_{6(g)}$$

Where † indicates surface species.

2.3.3 ALD ZrO_2

Zirconium oxide (ZrO_2) is an extensively studied material from both theoretical and experimental points of view. This is due to its excellent chemical and physical properties and important applications, which has positioned it as one of the most important ceramic materials in modern technology.[44] Due to its low thermal conductivity, high refractive index and high ionic conductivity, ZrO_2 has been used in areas such as thermal barrier coatings, high-temperature optical filters, oxygen sensors and fuel cells applications. It also has a high modulus and the toughest among ceramics at low temperatures when stabilized tetragonal phase is present. At ambient pressure the pure ZrO_2 has three phases (these are shown in figure 4.3): monoclinic, tetragonal and cubic. At high-temperature it has the cubic structure (space group *Fm3m*), which transforms to the tetragonal form (space group $P4_2/nmc$) at about 2570 K. At approximately 1400 K ZrO_2 passes to the monoclinic phase (space group $P2_1/c$). With increasing external pressure (between 3-15 GPa)[45] the monoclinic phase transforms into an orthorhombic phase. The tetragonal and cubic phases of ZrO_2 could be stabilized by (a) doping them with other oxides such as MgO, Co, and Y_2O_3, (b) making the grains very small, (c) growing as thin films, and (d) using substoichiometric composition. Depending on the doping concentration, ZrO_2 remains cubic or tetragonal even at room temperature.[46]

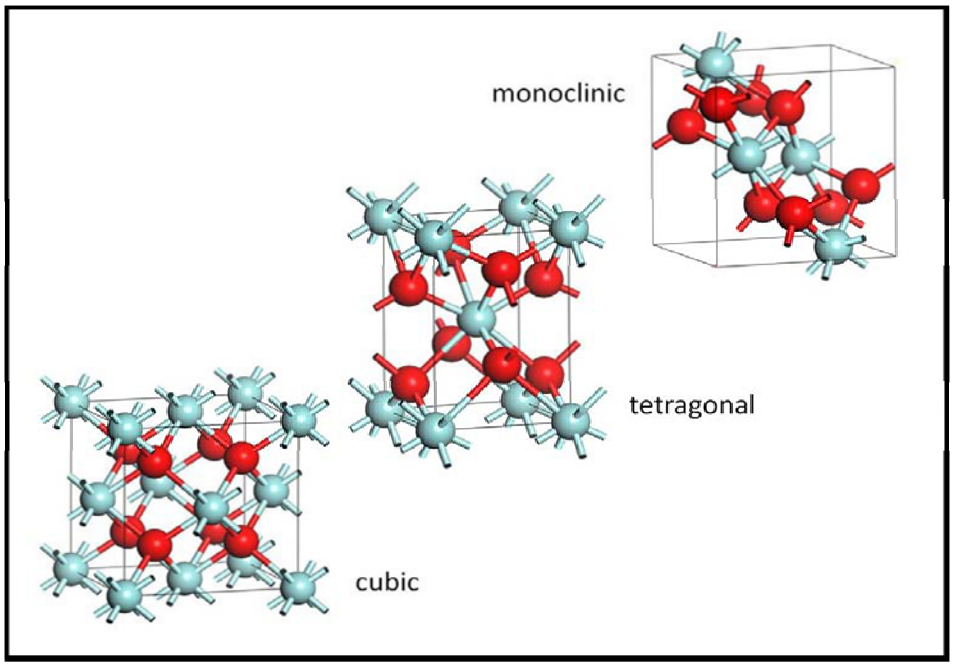

Figure 2.5: Low-pressure forms of ZrO_2. Red and Blue spheres are O and Zr atoms respectively.[30]

The crystal structure for ALD deposited ZrO_2 is sensitive to the precursors used, growth temperature and film thickness.[47] In this study, $Zr(nMe_2)_4$ and water were used as the zirconium and oxygen precursors respectively. The two half reactions that occur for ALD ZrO_2 when $Zr(nMe_2)_4$ and H_2O are used are found below:

$$ZrOH^{\dagger} + Zr(NMe_2)_4 \rightarrow ZrOZr(NMe_4)^{\dagger} + NMe_2H_7\ (g)$$

$$ZrOZr(NMe_2)^{\dagger} + H_2O \rightarrow ZrOH^{\dagger} + NMe_2H_7\ (g)$$

Where † indicates surface species.

2.3.4 ALD Al_2O_3

Aluminum oxide (Al_2O_3) in its bulk state is one of the most widely used materials in the family of engineering ceramics. It is known as a refractory material with good chemical stability, extremely high hardness and relatively high thermal conductivity.

Especially for the alumina thin films. These properties are very useful in technological applications in areas such as micro and opto-electronics, sensor techniques and catalysis.[48] The most common form of crystalline Al_2O_3, α-aluminium oxide, is known as corundum. Corundum has a trigonal Bravais lattice with a space group of R-3c. There are some emerging metastable alumina's, these includes the γ, δ, η, θ, κ, β, and χ polymorphs, and they have been growing in importance.[49] A variety of vacuum deposition techniques have been used to prepare Al_2O_3 films and ALD is one of such techniques. ALD deposited Al_2O_3 is the most studied deposited film by this technique. It is well known that applying ALD technique to prepare Al_2O_3 films, good quality amorphous thin film could be obtained below its crystallization temperature of ~500^{o}C. However, the preparation conditions determine the growth morphology and microstructure of the films thus changing their physical and chemical properties.

Few metal precursors have been explored in synthesizing ALD Al_2O_3. These metal precursors include aluminum chloride ($AlCl_3$)[1], tris-diethylamino aluminum (TDEAA)[50], and trimethylaluminium (TMA, $Al(CH_3)_3$)[51]. Of all these, TMA is the most common precursor used, this was also employed in this work. As an oxygen source, to react with the volatile metal source, water (H_2O) is most frequently used; O_3 is also sometimes used with TMA.[52] Other oxygen sources used include H_2O_2, O_2, O_3 as well as oxygen plasma. The TMA/H_2O ALD process has been studied as a nearly ideal ALD process because the GPC is high (30-40% of a monolayer). The two half reactions that occur for ALD Al_2O_3 when TMA and H_2O are used are found below:

$$AlOH^{\dagger} + Al(CH_3)_3 \rightarrow AlOAl(CH_3)^{\dagger} + CH_4\ (g)$$

$$AlOAl(CH_3)^{\dagger} + H_2O \rightarrow AlOH^{\dagger} + CH_4\ (g)$$

Where † indicates surface species. Al_2O_3 films grown by ALD are insulating, amorphous and smooth,[53] the surface of chemistry is also favorable to growth on a wide variety of substrates including oxides, nitrides, metals, semiconductors[54] and polymeric[55] surfaces. TMA decomposes at temperatures above 300^{o}C thus ALD Al_2O_3 is normally grown below 300^{o}C which is below the crystallization temperature.[56] In this dissertation, the growth temperature was set at 200^{o}C.

2.4 Chapter References

[1] Bowden, F. P., and Tabor, D., The Friction and Lubrication of Solids, Clarendon, Oxford, 1986, Part 1.

[2] Matthews, A., Franklin, S. and Holmberg, K., J. Phys. D: Phys. 40 (2007) 5463-5475

[3] S. M. Weiderhorn, S. M., Annu. Rev. Mater. Sci., 14(1984)373-403

[4] Erdemir, A., Friction and Wear of Ceramics, chapter 7

[5] Rainforth, W. M., J. Mater. Sci. 39 (2004) 6705-6721

[6] Gumbsch, P., Taeri-Baghbadrani, S., Brunner, D., Sigle, W. and Ruhle, M., Physical Review Letters, 87, 8 (2001)

[7] Karch, J., Birringer, R. and Gleiter, H., Nature 330, 10 (1987) 556-558

[8] Schiotz, J., Di Tolla, F. D. and Jacobsen, K. W., Nature 391 (1998) 561

[9] Koch, C.C., and Narayan, J., Mat. Res. Soc. Symp. Vol. 634 (2001)

[10] Erb, U., Nanostructured Mater. 6 (1995) 533-538

[11] Narayan, J., Koch, C.C., Zhang, X. and Venkatesan, R., Unpublished results, (2000)

[12] Yamakov, V., Wolf, D., Salazar, M., Phillpot, S.R. and Gleiter, H., Acta Materialia (2001) 2713-2722

[13] Schoitz, J., Di Tolla, F.D. and Jacobsen, K.W., Nature 391 (1998) 561-563

[14] Farkas, D. and Curtin, W.A., Materials Science and Engineering A, 412 (2005) 316-322

[15] Jerusalem, A., MSc. Thesis, Massachusetts Inst. of Tech. (2004)

[16] Muller, E., Oestreich, Ch., Popp, U., Michel, G. and Rendtel, A., Journ. Of Anal. Chem (1998) 361: 594-597

[17] Laurent Sagalowicz, Glen R. Fox, Marc-Alexandre Dubois, Claude A. P. Muller, Paul Muralt and Nava Setter, Journal of the European ceramic society 19 (1999) 1427-1430

[18] I.A. Ovid'ko and A.G. Sheinerman, Appl. Phys. Lett. 90, 171 927 (2007)

[19] I.A. Ovid'ko, N.V. Skiba, and A.G. Sheinerman, Physics of the Solid State 50(2008) 7

[20] Yifei Mo and Izabela Szlufarska, Appl Phys Letters 90, 181926 (2007)

[21] Jian, S.-R., Teng, I.-J., Yang, P.-F., Lai, Y.-S, Lu, J.-M, Chang, J.-G., and Ju, S.-P., Nanoscale Res Lett (2008) 3:186-193

[22] Lin, L.-Y., Kim, D,-Y., Thin Solid Films 517 (2009) 1690-1700

[23] Zabinski, J.S., Corneille, J., Prasad, S.V., McDevitt, N.T. and Bultman, J.B., Journal of Materials Science 32 (1997) 5313-5319

[24] Zabinski, J.S., Sanders, J.H., Nainaparampil, J. and Prasad, S.V., Tribology Letters 8 (2000) 103-116

[25] Suntola, T., and Antson, J., U.S. Patent No. 4,058,430, 15 November 1977

[26] Ritala, M. and Leskela, M., Atomic Layer Deposition (Handbook of Thin Film Materials, edited by H.S. Nalwa) Vol. 1 Academic Press. 2002.

[27] Kim, H., Lee, H. and Maeng. –J. W., Thin Solid Films 517 (2009) 2563-2580

[28] Becker, S. J., PhD Dissertation, Harvard University (2002)

[29] Puurunen, R.L., Journal of Applied Physics 97, 121301 (2005)

[30] Romanes, M., PhD Dissertation, Uni. of N. Texas (2008)

[31] Puurunen, R.L., Chemical Vapor Deposition 2003, 9, No. 5

[32] Leskela, M. and Ritala, M., Thin Solid Films 409 (2002) 138-146

[33] Dulub, O., Boatner, L. A. and Diebold, U., Surf. Sci. 519 (2002) 201

[34] Meyer, B. and Marx, D., Phys. Rev B 67 (2003) 035403

[35] Yoon, G., Yim, M., Kim, D., Ling, M. and Chai, D., Journal of Vacuum Science Technology. A 22(1, 2004)

[36] Gao, W. and Li, Z., Ceramics International 30 (2004) 1155-1159

[37] Helmersson, U., Latteman, M., Bohlmark, J., Ehiasarian, A. P. and Gudmundsson, J. T., Thin Solid Films 513 (2006) 1-24

[38] Christoulakis, S., Suchea, M., Katharakis, M., Katsarakis. N., Koudoumas, E. and Kiriakidis, G., Rev. Adv. Mater. Sci. 10 (2005) 331-334

[39] Kucheyev, S. O., Biener, J., Wang, Y. M., Baumann, T. F., Wu, K. J., Buuren, Van T., Hamza, A. V., and Satcher, J. H., Elam, J. W. and Pellin, M. J., Applied Physics Letters 86, 0831008 (2005)

[40] Niinisto, L., Paivasaari, J., Niinesto, J. and Nieminen, M., Phys. Stat. Sol. A 201, 7 (2004) 1443-1452

[41] Pung, S. Y., Choy, K. L., Hou, X. and Shan, C., Nanotechnology 19 (2008) 435609

[42] Makino, H., Miyake, A., Yamada, T., Yamamoto, N, and Yamamoto, T., Thin Solid Films 517 (2009) 3138-3142

[43] Godlewski, M., Guziewicz, E., Luka, G., Krajewski, T., Lukasiewicz, M., Wachnicki, L., Wachnicka, A., Kopalko, K., Sarem, A. and Dalati, B., Thin Solid Films 518 (2009) 1145-1148

[44] Torres-huerta, A. M., Vargas-Garcia, J.R., Dominquez-Crespo, M.A. and Romero-Serrano, J.A., Journal of Alloys and Compounds 483 (2009) 394-398

[45] Terki, R., Bertrand, G., Aourag, H. and Coddet, C., Materials Science in Semiconductor Processing 9 (2006) 1006-1013

[46] Sternik, M. and Parlinski, P., The Journal of Chemical Physics 122 (2005) 064707

[47] Aarik, J., Aidla, A., Mandar, H., Uustare, T. and Sammelsleg, V., Thin Solid Films 408 (2002) 97-103

[48] Krumov, E., Mankov, V. and Starbova, K., Journal of Optoelectronics and Advanced Materials Vol. 5, No. 3 (2003) p. 675 - 678

[49] Paglia, G., Ph. D. Dissertation, Curtin Univ. of Technology, Perth (2004)

[50] Katamreddy, R., Inman, R., Jursich, G., Soulet, A. and Takoudis C., J. Mater. Res., Vol. 22, No. 12 (2007)

[51] Lu, H.L., Ding, S.J., Chen, W., Zhang, D.W. and Wang, L.K., J. Mater. Res., Vol. 22, No. 5 (2007)

[52] Granneman, E., Fischer, P., Pierreux, D., Terhorst, H. and Zagwijn, P., Surface & Coatings Technology 201 (2007) 8899-8907

[53] Elam, J. W. Sechrist, Z. A. and George, S. M. Thin Solid Films, 414 (2002) 43-55.

[54] Groner, M. D., Elam, J. W., Fabreguette, F. H., and George, S. M., Thin Solid Films, 413 (2002) 186-197.

[55] Elam, J. W., Wilson, C. A., Schuisky, M., Sechrist, Z. A., and George, S. M., Journal of Vacuum Science & Technology B, 21 (2003) 1099-1107.

[56] Burgess Jr., D.R., Maslar, J.E., Hurst, W.S., Moore, E.F., Kimes, W.A., Fink, R.R. and Nguyen, N.V., Characterization and Metrology for ULSI Technology 2005

CHAPTER 3

EXPERIMENTAL PROCEDURE

In this chapter, the procedures used for sample preparation, film deposition and characterization will be discussed. The instruments used in the experiments belong to UNT's Materials Science and Engineering Department and the Center for Advanced Research and Technology (CART) at The University of North Texas, Denton. The operations and procedure manuals can be located on the CART webpage (http://cart.unt.edu).

3.1 Substrates Cleaning (Silicon Wafer, M50 Steel)

P-type silicon substrates which were cut into smaller pieces (approximately 1 in x 1 in) and mirror polished M50 Steel coupons that were obtained from Timken Company, Canton, OH were used as the substrates. Prior to the nanolaminates film deposition, the silicon (100) substrates were ultrasonically cleaned in acetone, methanol and deionized water for five minutes each. In the case of the mirror polished M50 steel coupons, they were ultrasonically degreased in soap and DI water for 10 minutes. This was followed by 5 minutes of acetone, methanol and DI water cleaning respectively, all with ultrasonication. The substrates were blown dry with high purity nitrogen gas.

3.2 Film Deposition

$ZnO/Al_2O_3/ZrO_2$ trilayer and ZnO/ZrO_2 bilayers were deposited on both cleaned silicon and M50 substrates by using the Cambridge NanoTech Savannah 100 viscous flow hot wall single wafer ALD reactor. On depositing the $ZnO/Al_2O_3/ZrO_2$ one trilayer film on the silicon substrate, the ZrO_2 was deposited first on the silicon with native oxide, this was followed by the Al_2O_3 and the ZnO was the final layer to be deposited. In the case of the M50 steel coupons, the nanolaminates were deposited in the order of $ZnO/Al_2O_3/ZrO_2/Al_2O_3$. Al_2O_3 was the first to be deposited and this was followed by the ZrO_2. Another layer of Al_2O_3 layer was deposited before the ZnO was finally deposited. The ZnO/ZrO_2 bilayer films were only deposited on silicon substrate. Two separate types (2 and 8 bilayers) of the ZnO/ZrO_2 were deposited. The ZrO_2 was deposited first on the silicon with native oxide followed by the ZnO layer. This was repeated until the required number of bilayers were acheived. The ZnO is always the top surface layer. The ZnO and Al_2O_3 were deposited at 200^oC and the ZrO_2 deposited at 250^oC. Figure 3.1 shows the ALD reactor and the computer control interface. The operation of the ALD is controlled by the LabView software. But inserting or removing of substrate from the deposition chamber or turning on and off of the precursors are controlled manually. The deposition chamber has a reactor space of 100 mm in diameter x 6mm deep. Table 3.1 provides a description of the experimental conditions for the $ZnO/Al_2O_3/ZrO_2$ one trilayer film while Table 3.2 describes the conditions for the ZnO/ZrO_2 bilayers.

Table 3.1: Deposition conditions for growing ZnO/ Al_2O_3/ ZrO_2 one trilayer nanolaminate.

Precursor	Pulse (S)	Purge (S)	Number of Cycles	Deposition Temperature (°C)	GPC (Å/cycle)
T Zr	0.4	60	1283	250	1.5
DI H_2O	0.025	60			
TMA	0.015	20	408	200	0.79
DI H_2O	0.015	20	123		
DEZ	0.015	60	690	200	1.02
DI H_2O	0.015	60			

Table 3.2: Deposition conditions for growing ZnO/ZrO_2 two and eight bilayer nanolaminates.

Precursor	Pulse (s)	Purge (s)	Number of Cycles (2 Bilayers)	Number of Cycles (8 Bilayers)	Deposition Temperature (°C)	GPC (Å/cycle)
T Zr	0.4	60	567	161	250	1.5
DI H_2O	0.025	60				
DEZ	0.015	60	351	99	200	1.02
DI H_2O	0.015	60				

Figure 3.1: An image of the Savannah 100 ALD system with the accompanying software, used for all the nanolaminate depositions. (Source: Cambridge Nanotech Inc).

In the ZrO_2 film deposition, Tetrakis (dimethylamido) zirconium(IV) "$Zr(NMe_2)$" from Sigma Aldrich and de-ionized water were used as the chemical precursors to provide Zr and O sources to the growing surface. The Al_2O_3 film was deposited by using Trimethyl Aluminum "(TMA) as the Al precursor, the precursor that was used in the case of ZnO is Diethyl Zinc "(DEZ)" as the Zn precursor. The metal organic and the de-ionized water precursors were alternatively pulsed into the reactor using N_2 as a carrier gas. In order to prevent gas-phase reaction which is caused by intermixing of the precursors, the reactor was purged with research grade nitrogen gas after each precursor pulse. The flow rate for the N_2 gas is 20 sccm. Inside the chamber, the base pressure was

maintained at approximately 0.5 torr. The $Zr(NMe_2)$ precursor was set at 75^{o}C, with the precursor valve temperature also set at 115^{o}C, the stop valve tee and bellows temperatures were set at 150^{o}C. These settings as well as the deposition parameters such as, duration of the metal organic and de-ionized water pulses, purge time between precursor pulses, number of cycles, inner disk/substrate and the outer disk temperature were all controlled by the LabView software. After substrate is loaded, a wait time of 10 minutes is allowed for the chamber and substrate conditions to reach equilibrium before the pulsing is started.

The samples are removed from the vacuum chamber after the deposition and it is allowed to cool down in air before storing them in the desicator.

3.3 Film Characterization

3.3.1 Ellipsometry

A J A Woollam Variable Angle Spectroscopic Ellipsometer (VASE) was used to measure the thickness of the ZnO, Al_2O_3 and ZrO_2 films. Measurements were between 400 and 1200 nm under 65^{o}, 70^{o} and 75^{o} incidence angle. The VASE is equipped with a Czerny-turner scanning monochomator with a focal length of 160 mm and an effective aperture ratio of f/4.5. The wavelength dependence of the refractive index film and extinction coefficients were modeled using the Wvase32 software that accompanied the instrument.

3.3.2 Heat Treatment Furnaces

Thermal annealing was undertaken by using the Barnstead Thermolyne 48000 Furnace. The samples were annealed at 400 and 1000^{o}C for duration of 2 hours. All thermal annealing of the samples were done under atmospheric pressure, after anneal the samples were allowed to air cooled.

3.3.3 Atomic Force Microscopy

To determine the surface topography and roughness of the as deposited and annealed nanolaminates, an atomic force microscope (AFM) was used. All the samples were studied using the Veeco Nanoscope III Scanner Probe microscope AFM. All the imaging were done in the tapping mode, with silicon cantilever probes (Tap300-10 from Budget Sensors) of 300 kHz resonating frequency. The sizes of the scanned areas were typically 5 μm x 5 μm, the scans were done at three different areas on the sample. These values were averaged out and used as the average roughness of the deposited film.

3.3.4 X-ray Diffraction

In order to identify the phases and assess the possible texture crystallographic orientation in both the as deposited and the annealed nanolaminate films, a Rigaku Ultima III diffractometer was used in the grazing angle incidence XRD (GIXRD) in the parallel beam mode using a thin film stage and a scintillation detector. CuK_{α} x-rays with a wavelength of 0.154 nm were generated at 40 kV and 44 mA. Scans were done between 20-90^{o} 2theta, most of the settings were kept at constant values: 5^{o} incident angle, 0.05^{o} step size, 2 degree/min scan speed, 10 mm divergence height limiting slit, 0.5^{o} incident side Soller slit, open attenuator, 0.5^{o} diffracted side parallel beam (PB) slit, and open

sizes for all divergence, scattering and receiving slits (DS/SS/RS). Jade v7.0 software was used to process and analyze the scan results for GIXRD.

According to the Debye-Scherrer equation,

$$d = \frac{0.9\,\lambda}{B\cos\theta} \tag{3.1}$$

(Bauer et al., 1978) which relates the crystal size to the broadening of the diffraction peaks, the grain sizes of the deposited crystals were determined. From the equation, λ is characteristic CuK_{α} wavelength of 0.154 nm, B is the full-width at half maximum (FWHM) of the broadened diffraction line on the 2θ scale (radians) and θ is the angle (Bragg angle) between the incident beam and sample plate in the XRD machine. When the FWHM of a peak is measured, the resultant breadth is a product (convolution) of the actual material and the instrument, this is known as the instrumental broadening. Thus in order to determine the actual FWHM of the material, the instrumental broadening FWHM must be removed. The FWHM of the instrument has been identified from the x-ray diffraction spectrum of single crystalline Si wafer to be 0.0016049 (radians). Thus if the observed peak of the material has a width of W_{FWHM}, and the width due to instrumental effect is W_{instr}, then the new width used in determining the crystallite size W_{sample} is given by:

$$W_{sample}^2 = W_{FWHM}^2 - W_{instr}^2 \tag{3.2}$$

3.3.5 Pin-on-Disc (POD) Tribometer Test

The coefficients of friction (COF) of the films were determined by using the Falex (Implant Sciences) ISC – 200 pin-on-disk (POD) tribometer. This pin-on-disk tribometer measures the sliding friction coefficient on planar surfaces. The deposited

nanolaminate films (thin film disk) were rotated under the pin counterface materials which were held in a stationary position by a cantilever beam. In order to generate a point contact between the pin and the disk, a vertical (normal) load is applied. Si_3N_4 (H = 22 GPa) and SS 440 C (H = 10 GPa) pins/balls with 1/8 inch (3.2 mm) diameter (ceramic/ceramic and metal/ceramic respectively) were used as the counterface materials. The coefficients of friction were calculated throughout the test by taking the ratio of the tangential load, measured by a strain gauge transducer, to the normal load. The tests were performed in unidirectional sliding mode under normal loads that were of 25, 50, 100 and 250 grams at room temperature and lab air (~ 40% relative humidity). Table 3.3 provides the experimental POD test protocol used for the nanolaminate films. The pins were cleaned with acetone, methanol and DI water respectively prior to performing any test. The POD tests were repeated at least two times on a particular film. However, the radius was changed as well as the total number of cycles to reach the same distance (200 m) travelled by the pin. The revolutions per minute (RPM) is also adjusted whenever the radius is changed in order to keep the linear speed constant at 2.2 cm/s for all the POD tests.

Table 3.3: POD Test Design Settings

Set	Normal Load (g)	Pin Material	Replicates
Nanolaminates on Si substrate (As-deposited and Annealed)	25, 50, 100	Stainless Steel (SS440C) Si_3N_4	≥ 2
Nanolaminates on M50 Steel substrate (As-deposited and Annealed)	25, 50, 100, 250	Si_3N_4	≥ 2

In order to assess the tribological behavior of the films, the Hertzian Theory of Elastic Deformation was used to determine the contact parameters. This theory relates the circular contact area of a sphere with a plane (or more general between two spheres) as depicted in figure 3.2 to the elastic deformation properties of the nanolaminates.

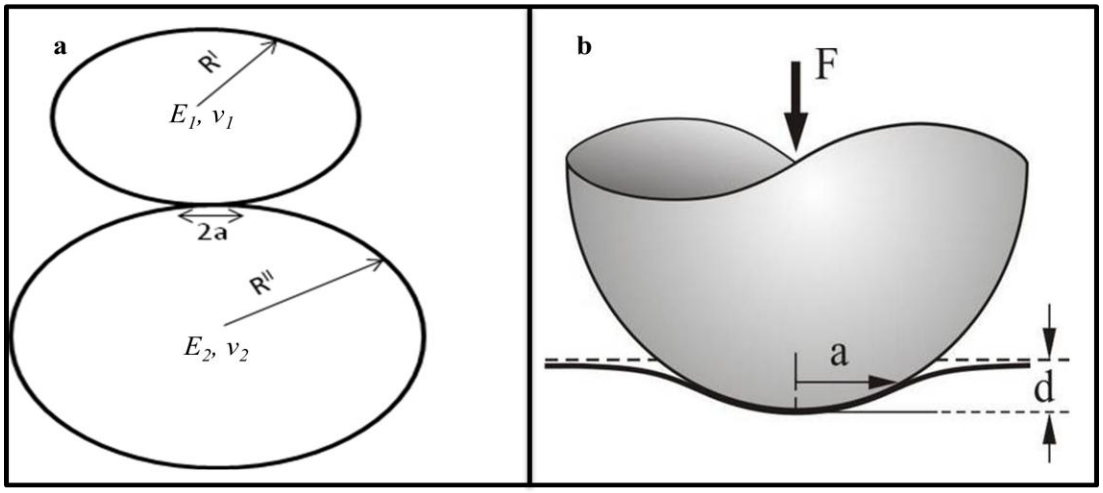

Figure 3.2: Schematic illustration of a) Hertzian contact between spheres, b) Hertzian contact between a sphere and an elastic material, with an increase in contact area.

Considering two bodies with radii of curvature R^I and R^{II} that are in contact, the contact radius, a, is given by

$$a = \left[\frac{3LR}{4E^*}\right]^{\frac{1}{3}} \tag{3.3}$$

where L is the applied normal force (load), R is the relative radius of the contact and E* is the combined Young's modulus of the two materials. R and E* are defined below.

$$R = \left(\frac{1}{R^I} + \frac{1}{R^{II}}\right)^{-1} \tag{3.4}$$

where R^I and R^{II} are the radii of the contacting surfaces, e.g. radii of pin and disc. The radius is considered positive for convex surface and negative for a concave surface. For radii with flat surfaces, infinity is normally used.

$$\frac{1}{E^*} = \frac{1-v_1^2}{E_1} + \frac{1-v_2^2}{E_2} \tag{3.5}$$

where v is the Poisson's ratio and E_1 and E_2 are the elastic modulus of the contacting materials. For a circular (point) contact, the mean pressure (P_m) is given by;

$$P_m = \frac{L}{\pi a^2} \tag{3.6}$$

The maximum pressure (Hertz pressure), P_{max} occurs at the center of the contact and this is given by

$$P_{max} = \frac{3L}{2\pi a^2} = \frac{3}{2}P_m \tag{3.7}$$

In analyzing the tribological behavior of solid coatings, the kinetic friction coefficient defined as the ratio of the frictional force and the applied load, i.e.

$$\mu = \frac{F}{L} \tag{3.8}$$

was applied. The frictional force, F, is expressed as a product of the actual contact area (A) and the shear strength of the lubricant material that has to be overcome in order to slide (τ), $A\tau$ as shown in figure 3.3. Bowden and Tabor (1986) assumed that in order for the bodies to slide relative to each other

a. The asperities should plastically deformed and
b. The interfacial stress component should correspond to the shear strength of the soft material τ_{crit}.

3.3.6 Rolling Contact Fatigue Test

The rolling contact fatigue (RCF) machine was used to determine the life of rotating cylindrical test specimens (3/8" diameter rod) subjected to various material, lubricant, and load conditions. The springs on the test head were used to transmit a load of 1.5 GPa through the cups to the three ½" diameter balls. The three 52100 steel (uncoated) balls are driven by the rod and rotate around the rod. 8 to 10 drops of MIL-L-23699 synthetic based oil lubricant is supplied by drip feeding onto the top of the rod. The rod rotates at a speed of 3600 rpm and the test runs until a spall develops and/or the coating fails. Figure 3.4 shows a schematic diagram of a three ball on rod RCF machine and table 3.4 provides the conditions under which the test was undertaken.

Table 3.4: RCF Testing Conditions

Rod Coating	ALD $ZnO/Al_2O_3/ZrO_2$ on CrN/Cr/M50
Cup Coating	ALD $ZnO/Al_2O_3/ZrO_2/Al_2O_3$ on CrN/Cr/M50
Balls	52100 steel (uncoated)
Hertzian Pressure	1.5 GPa
RCF Cycles	10,000/20,000/1.3 million/or 6 million
Lubricant	MIL-L-23699 (8-10 drops per minute) –synthetic based oil used in aircraft turbine engines

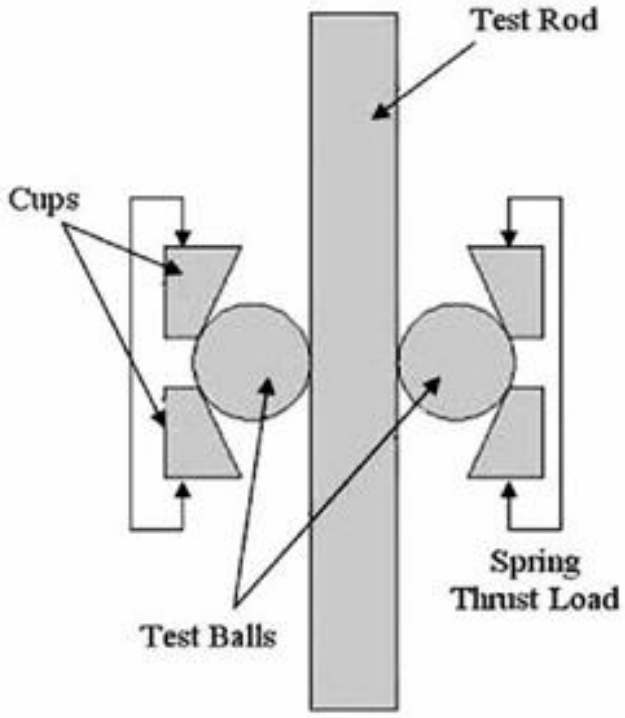

Figure 3.3: Schematic of three ball on rod RCF machine.

3.3.7 Optical Microscopy

A Nikon Eclipse ME600 optical microscope was used to capture the images of the pin surfaces and the wear tracks at 10X, 20X and 50X magnifications after POD testing. The images were analyzed by the NIS-Elements BR2.30 software.

3.3.8 Profilometer

A Veeco Dektak 150 Profilometer was used to measure the wear track depths and cross-sectional areas removed after the pin-on-disk tests. The cross-sectional area data were used to calculate the wear factor of the worn area. The stylus pin used had a radius of 12.3 µm radius, a force of 100 µg was applied with scan lengths between 800 and 1200 µm.

3.3.9 Scanning Electron Microscopy and Focused-ion beam microscopy and Micromachining

A FEI-Nova Dual Beam Scanning Electron Microscopy/Focused Ion Beam (SEM/FIB) was used for evaluations of both the unworn and worn surfaces and the debris after the POD testing. Cross-sectional TEM specimens preparation was also performed with the dual beam focused ion beam inside the SEM. The micromachining technique was done by using Ga ions in the FIB to prepare the specimens of <100 nm thickness and approximately 10 – 20 µm long cross-section. Before the specimens were micromachined, three different techniques for protecting the surface of the nanolaminate films were undertaken. First, a ~50 nm thin layer of electron beam Pt was deposited at 3kV, 4.3 nA, this was followed by a 500 nm ion beam Pt at 10 kV, 0.1 nA and finally, a 1 µm ion beam Pt at 30 kV, 0.12 nA. Rough milling was done at 30 kV starting at 7 nA

spotsize and progressively decreased to 50 pA as the foil is thinned down to electron transparency i.e. <100 nm. A 5 kV, 70 nA cleaning/final thinning step was done to eliminate ion damage from the specimen. After the cut with the Ga ion beam, the specimen was then transferred via an Omniprobe nanomanipulator and attached onto a 3-mm TEM Cu grid. In order to remove carbon and other impurities from the specimens surfaces prior to being introduced into the TEM chamber, the specimens were cleaned with Ar plasma.

3.3.10 Transmission Electron Microscopy and Energy Dispersive X-ray Spectroscopy

An FEI Co. Tecnai G2 F20 S-Twin Schottky field-emission Scanning Transmission Electron Microscopy (S/TEM) was used to characterize the structure, ZnO lattice d-spacing, and ZnO grain orientation inside and outside the wear tracks. The STEM was operated at 200 kV.

3.3.11 X-ray Photoelectron Spectroscopy

The stoichiometry and composition of the nanolaminates were determined by PHI 5000 Versaprobe X-ray Photoelectron Spectrometer system. The XPS system is equipped with a monochromatic Al $K\alpha_1$ x-ray source of 1486.6 eV ($h\nu$). The elemental composition of the surface of the films were acquired by operating the X-ray source at 10.9 W with a pass energy of 58.7 eV, 45^o take-off angle and 0.5 eV/step scan rate. Additionally, an Ar^+ gun was used to sputter clean the top 1.2 nm of the films to remove adventitious carbon, and subsequently extract the chemical bonding information from below the original surface. The depth profiling was done with intermittent ion sputtering Ar^+ ion beam at 1 kV raster-scanned over a 2 mm x 2 mm area of the sample for a

predetermined time of 60 s followed by a core level spectra acquisition. The depth profile samples were characterized using a 200 µm x-ray spot at 50 W power. A PHI MultiPak™ software was used to fit the curves and smooth both the elemental composition and depth profile line shapes.

3.3.12 Auger electron spectroscopy

Surface analysis with auger electron spectroscopy (AES) was performed inside of the wear tracks. This was done to analyze the chemical composition inside the wear tracks. The AES analysis was performed with a PHI 670xi Scanning Auger Nanoprobe (SAN) working at 10 - 20 keV and a beam current of 10 nA. The SEM attached with the SAN was used to obtain the micrographs with magnifications of up to 14000X by using raster scanning with a highly focused electron beam. Using the same raster scan, with a 2 point acquisition method and a 512 resolution, the SAN was used to produce elemental composition maps of the wear tracks. A PHI MultiPak™ software was used for the compositional analysis of the mapped wear tracks.

CHAPTER 4

ATOMIC LAYER DEPOSITION OF LUBRICIOUS $ZnO/Al_2O_3/ZrO_2$ AND ZnO/ZrO_2 NANOLAMINATE FILMS ON SILICON SUBSTRATE

In this chapter, the experimental results and discussion of the various processing, structure and properties of $ZnO/Al_2O_3/ZrO_2$ one trilayer and ZnO/ZrO_2 2 and 8 bilayers nanolaminate films deposited on silicon substrate by ALD are presented. It should be noted that the characterization follows a top-down approach, where the surface is characterized first going down towards the substrate. The post-tribotest characterization is preceded by the as deposited and annealed nanolaminate characterization. Based on the results, the $ZnO/Al_2O_3/ZrO_2$ one trilayer nanolaminate films have the best potential to be used as a solid lubricant in load bearing and high temperature applications. These results findings are summarized at the end of the chapter.

4.1 Nanolaminate film condition selection

The nanolaminate films were deposited on Si wafers to study the role of structure in controlling the tribological properties (coefficient of friction and wear factor). Approximately 200 nm thickness nanolaminate film was deposited with different layer combinations under varying deposition conditions. The crystal structure and coefficient of friction (COF) results on various nanolaminate thin films were first considered to identify what combination and deposition conditions resulted in lower friction and wear

factor.[1] Based on the COF and the wear factors, it was identified that the $ZnO/Al_2O_3/ZrO_2$ nanolaminate film possessed the best properties.

4.1.1 $ZnO/Al_2O_3/ZrO_2$ One Trilayer Surface Morphology

AFM was used to study the surface roughness of the as deposited and annealed nanolaminate films. Figure 4.1 shows the AFM images of 1-trilayer of the as-deposited, *ex-situ* annealed in air at 400^{o}C and 1000^{o}C nanolaminate films. The deposition conditions for these films were previously outlined in Table 3.1. The images indicate that there is increase in the surface roughness as the nanolaminate films are annealed at 1000^{o}C, the as-deposited nanolaminate film has the smoothest surface followed by the 400^{o}C film. Figure 4.2 shows a plot of the surface roughness (RMS) verses temperature of anneal, this plot also indicates an increase in the height range of the asperities (Z-range) as the annealing temperature is increased. The as-deposited nanolaminate film has the lowest height range, this is followed by the 400^{o}C with the 1000^{o}C having the highest height range. This is in accordance with the RMS data for these three conditions.

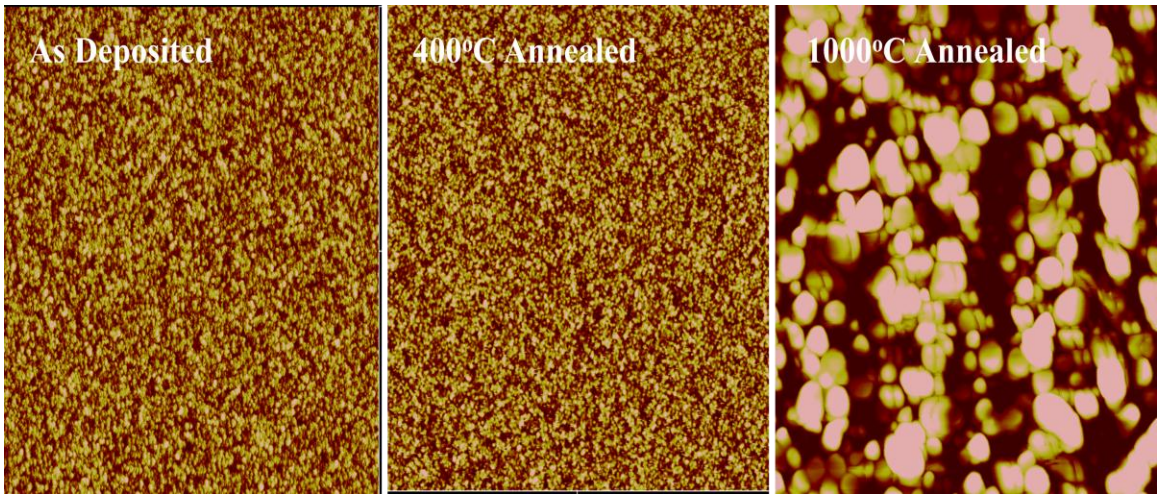

Figure 4.1: AFM surface scan of 1-trilayer nanolaminate film with scan size of 5 X 5 µm. As-deposited (left), ex-situ annealed in air at 400°C (middle) and 1000°C (right).

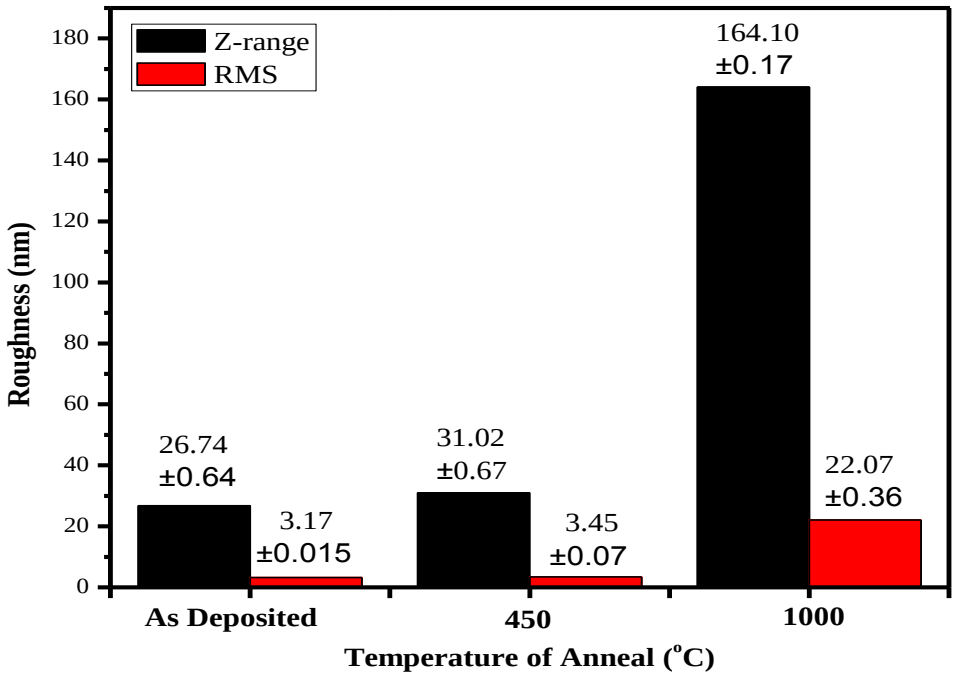

Figure 4.2: A graph of the Temperature of Anneal versus the Surface Roughness Parameters of One Trilayer Nanolaminates.

4. 1. 2 $ZnO/Al_2O_3/ZrO_2$ One Trilayer Nanolaminate Film Composition

XPS was used to analyze the chemical composition of the one trilayer nanolaminate films. It was determined that the as-deposited Zn:O composition was 57:43 atomic percentage. ZnO should demonstrate a 50:50 zinc-to-oxygen atomic percentage ratio, thus the ZnO layer exhibits oxygen deficient stoichiometry that would suggest oxygen vacancies, or conversely zinc rich (zinc interstitials). After annealing the nanolaminate to 400^{o}C, the ZnO layer became closer to stoichiometric with values of 53:47 indicating some surface oxidation. At 1000^{o}C annealing, there is the presence of both Zr and Al in the surface composition. The presence of these two elements at the surface indicates that there is either a diffusion of the Zn into the underneath layers or Zn evaporation. This may also explain why the AFM analysis indicated a very rough surface after the 1000^{o}C anneal.

(a)

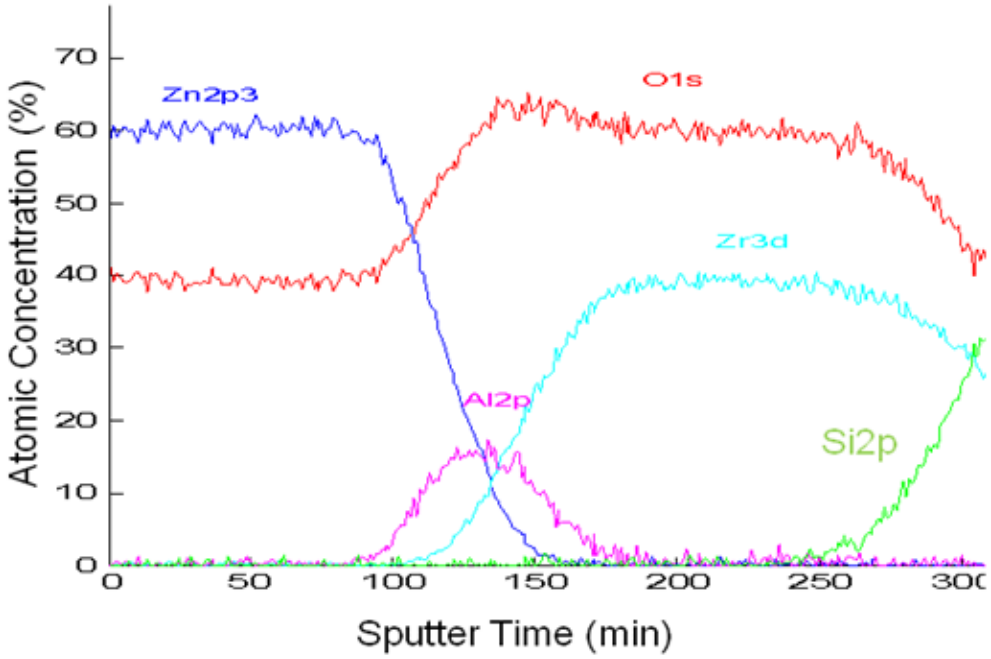

(b)

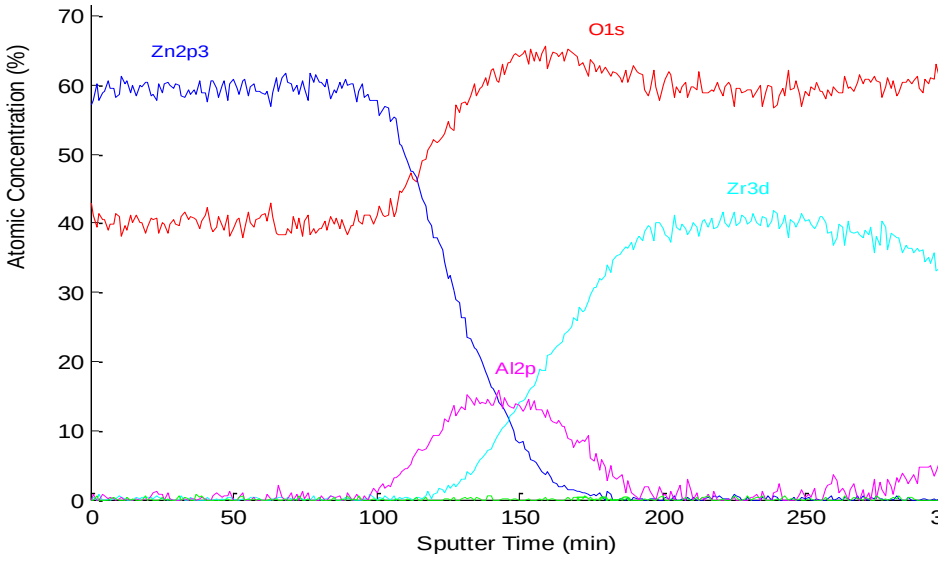

Figure 4.3: XPS depth profile results of $ZnO/Al_2O_3/ZrO_2$ nanolaminate film deposited on Si substrate (a) As-deposited, (b) annealed at 400^{o}C.

(c)

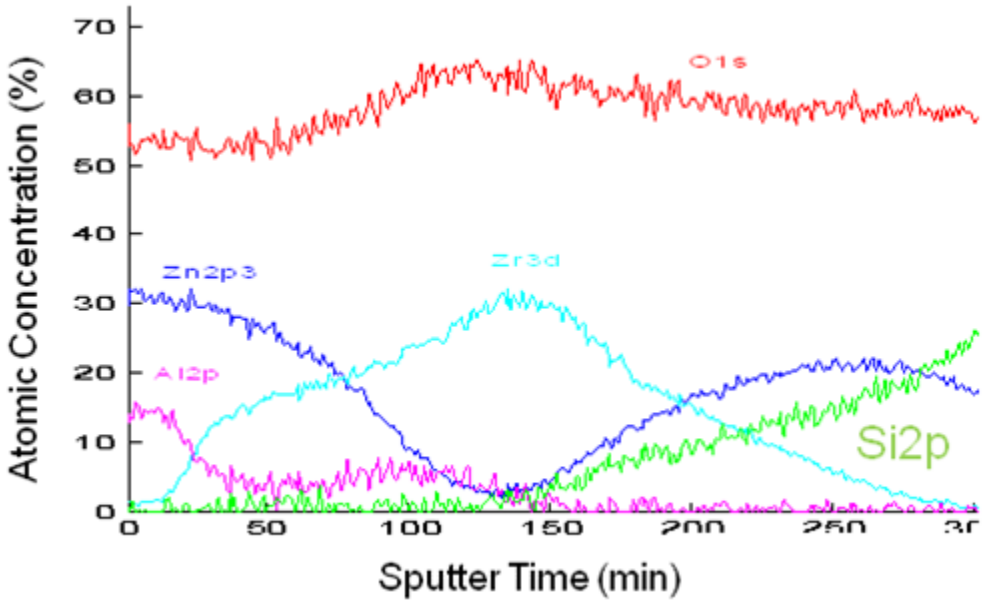

(d)

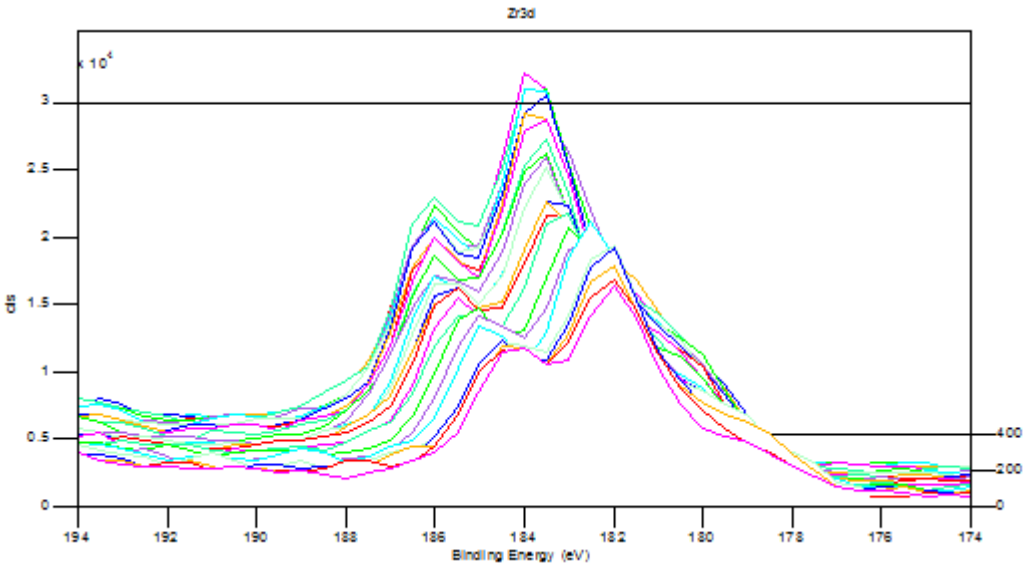

Figure 4.3: XPS depth profile results of $ZnO/Al_2O_3/ZrO_2$ nanolaminate film deposited on Si (c) annealed at 1000°C. (d) Zr $3d_{5/2}$ peak montage after 1000°C anneal.

In Figure 4.3a, the XPS depth profile of the as-deposited nanolaminate film confirms the oxygen deficiency in the ZnO, Al_2O_3 and ZrO_2 layers. The depth profile for the nanolaminate film annealed at 400^{o}C showed similar atomic concentrations as the as-deposited film. This is shown as Figure 4.3b. In Figure 4.3c, the depth profile for the 1000^{o}C annealed film shows the presence of high concentration of Al on the surface while there is a very low concentration of Zr on the surface. Even though there is Zn on the surface, it is observed that there is diffusion of Zn into the other layers, a high concentration of Zn was observed sitting on top of the Si substrate. Figure 4.3d indicates the Zr $3_{d5/2}$ montage. It is observed from the plot that, the $3_{d5/3}$ peak is shifting from the right towards the left as sputter time increases. After 50 minutes of sputtering, the binding energy of the $3_{d5/2}$ spectra is ~ 181.9 eV, this increased steadily to 183.9 eV after 180 minutes of sputtering. There have been several studies on the peak shift on the shift of the 3d5/2 spectra. It has been related to change in the Zr oxidation state, thus with the Zr cations mainly present in the valence four oxidation state (Zr^{4+}), can change to Zr^{3+} and Zr^{2+} due to the Zr cations filling interstitial states during the thermal aneal. This is observed when there is a peak shift of more than 1 eV which was observed in the montage above (Figure 4.3d).[28] It is also observed that, there is difference in the atomic percentages of the high resolution scan and the depth profile; this could be attributed to the preferential sputtering of oxygen by the argon during the depth profiling.[2]

4.1.3 $ZnO/Al_2O_3/ZrO_2$ One Trilayer Nanolaminate Films Microstructure

The XRD spectra (with incident angle = 5^o) of the ALD deposited nanolaminate films on silicon are shown in Figure 4.4. For all the conditions, the XRD spectra show that ALD ZnO film crystallizes in the hexagonal wurtzite structure grains with strong (0002) diffraction peak implying that most of the c-axis of ZnO grains are arranged perpendicular to the substrate surface. The spectra also shows peaks for ZrO_2, with the as deposited and 400^oC annealed nanolaminates exhibiting tetragonal crystal structure. The peak that is dominant in these nanolaminate films is the (101) peak. In the case of the 1000^oC annealed nanolaminate film, the crystal structure changes from tetragonal to monoclinic and the most dominant peak is the (-111). There were no peaks that could be attributed to the Al_2O_3 and aluminum-zinc oxide (AZO, $ZnAl_2O_4$), thus the Al_2O_3 is an amorphous layer.

The XRD scans of the as-deposited and annealed nanolaminate films, which shows peaks corresponding to hexagonal ZnO (wurtzite structure), tetragonal and monoclinic ZrO_2 are based on indexed PDF#01-089-7102, PDF#01-070-7304 and PDF#01-070-8739, respectively. The ZnO (0002) peak was detected at ~34.5^o 2θ, the ZrO_2 (101) and (110) peaks at ~30.6^o and ~35.3^o 2θ respectively and the ZrO_2 (-111) peak at 28.4^o. No Al_2O_3 peaks were detected in the films. ZnO crystallites are clearly (0002) preferentially orientated or textured. Figure 4.5 shows the corresponding ZnO (0002) pole figure for the as-deposited film, which confirms the highly (0002) out-of-plane fibrous texture. The most favorable growth directions of ZnO crystals are (0001), (0110) and (2-1-10), out of these, (0001) is the fastest growth direction.[3,4] Thus (0002) texture,

otherwise called c-axis orientation, is commonly observed in ZnO films because the c-plane perpendicular to the substrate normal is the most densely packed and thermodynamically preferred in the wurtzite structure.[5] ZnO films that are grown on glass and amorphous substrates also exhibit the c-axis orientation.[6] A (0002) texture has been shown to promote good tribological properties in PLD ZnO, so promoting its growth in the nanolaminates is productive for tribological applications.[7]

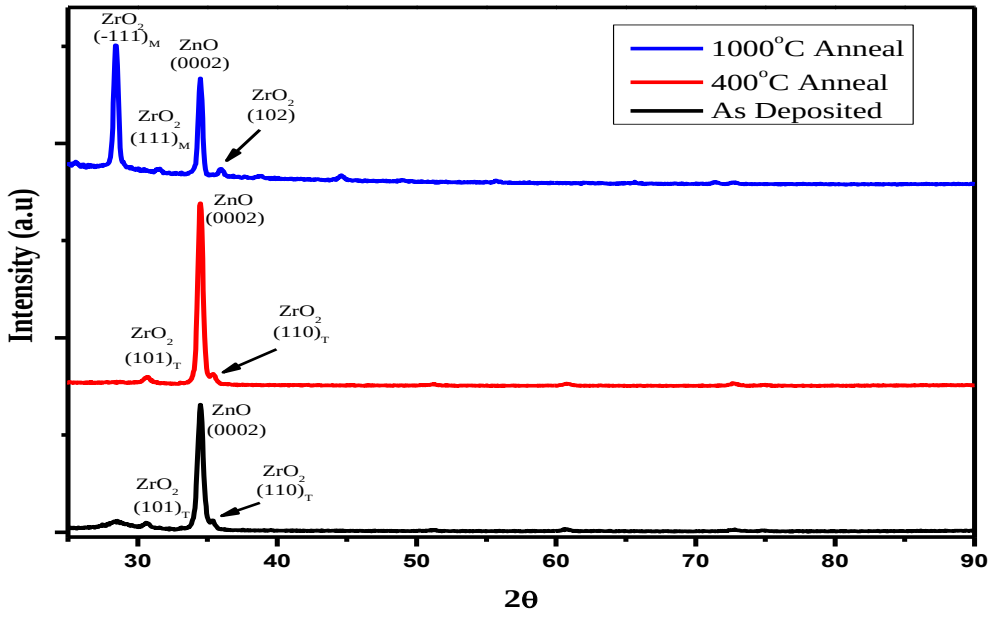

(a)

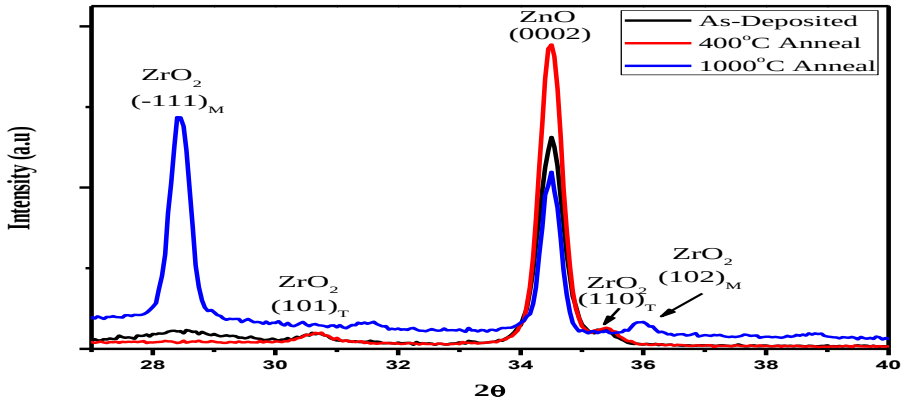

(b)

Figure 4.4: GIXRD analysis of ZnO/Al_2O_3/ZrO_2 nanolaminate films with θ - 2θ scans of as-deposited and annealed films.

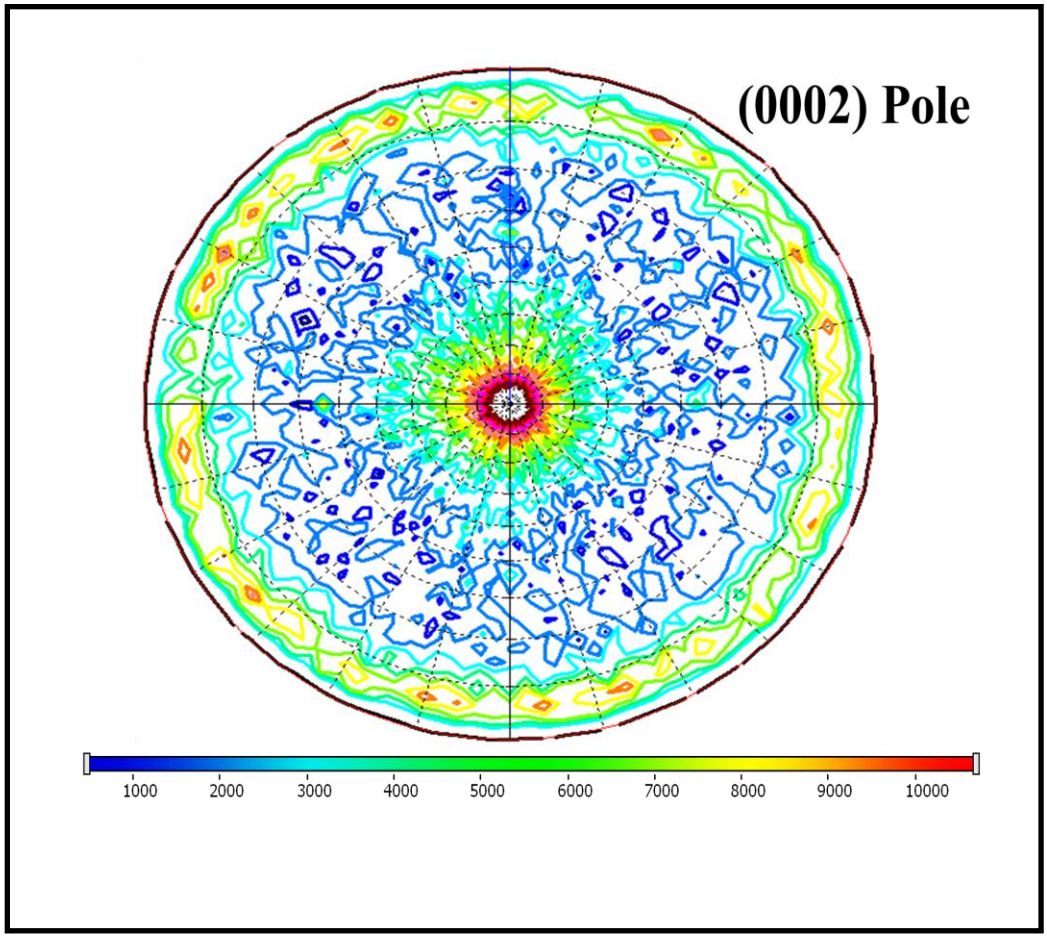

Figure 4.5: ZnO (0002) pole figure of as-deposited film. Color level corresponds to x-ray intensity counts.

With annealing at 400^{o}C, it was determined that the intensity of (0002) diffraction peak increased and the full width at half maximum (FWHM) became slightly narrower. The increase of diffraction intensity and narrowing of FWHM are related to the enhanced crystallinity and increased grain size, respectively. At 1000^{o}C annealing, there was a further reduction in the FWHM with a decrease in intensity. The decrease in intensity is due to the diffusion of the ZnO nanocrystalline layer into the other layers. The values of FWHM for (0002) diffraction peaks were 0.45^{o}, 0.41^{o} and 0.37^{o} for the as-deposited,

400^{o}C and 1000^{o}C annealed films, respectively. In addition, it is clear that there is no peak shift due to annealing (Figure 4.4b), this means that the as-deposited and annealed films have no detectable built-in lattice strain.[8]

The narrowing of the peaks with increase in annealing temperatures can be related to the increase in grain size by the Debye-Scherrer formula (Section 3.3.4). The raw FWHM values were corrected by subtracting the instrumental broadening value that was identified from the x-ray diffraction spectrum of single crystalline silicon wafer to be 0.0016049 radians (section 3.3.4).[9] Table 4.1 shows the FWHM and the calculated grain sizes of the as deposited, 400^{o}C and 1000^{o}C annealed films respectively. The grain size is illustrated in Figure 4.6.

Table 4.1: Table of the FWHM and grain sizes of the $ZnO/Al_2O_3/ZrO_2$ One Trilayer Nanolaminate Films

	FWHM (^{o}) of (0002) ZnO Plane	**Grain Size (nm) of (0002) ZnO Plane**
As-Deposited	0.45	27.8 ± 0.74
400^{o}C Annealed	0.41	34.1 ± 1.04
1000^{o}C Annealed	0.37	49.8 ± 0.74

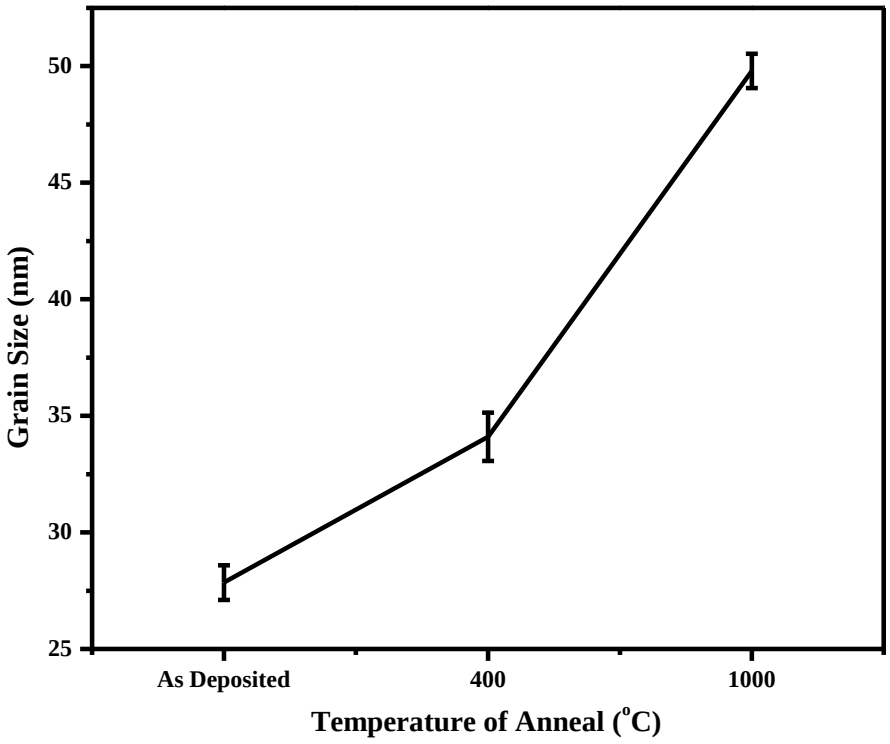

Figure 4.6: A graph that shows an increase in grain size of ZnO (0002) grain with the increase of temperature of anneal.

From the XRD data and as already mentioned, the sandwiched Al_2O_3 between the ZnO and the ZrO_2 layers is amorphous. It has been reported elsewhere that the amorphous Al_2O_3 layer grown beneath a thin ZnO film helps in achieving the (0002) preferred orientation of the ZnO thin film. Thus the *a*-Al_2O_3 layer suppresses growth of (1010) and (1011) ZnO grains. According to Romanes,[10] Al_2O_3 deposited underneath a ZnO layer exhibited a better (0002) reflection than when ZnO was deposited on amorphous SiO_2 native oxide. Thus it is right to conclude that the Al_2O_3 promotes the growth of (0002) oriented grains.

The XRD data also confirms that tetragonal and monoclinic ZrO_2 is crystalline with (101) and (-111) textures, respectively. The (101) peaks were detected at ~30.6 while the (-111) peak was detected at 28.4^{o}C on the 2 theta axis. The mean grain size of tetragonal (101) ZrO_2 before and after 400^{o}C anneal on silicon was ~15.9 nm. There was no change in the grain size after anneal. The relatively high toughness ALD ZrO_2 should act as a load bearing layer (at moderate contract stresses) and as a pathway to dissipate energy to prevent cracking between the bilayers. The phase transformation of ZrO_2 from tetragonal to monoclinic due to thermal anneal has been observed by other groups. Various studies have shown this effect in tetragonal thin films with grain sizes of approximately 50 or less nanometers. From Figure 4.4, it was observed that, the as-deposited and 400^{o}C annealed films both possessed a tetragonal ZrO_2 phase, but when the nanolaminate film was annealed at 1000^{o}C, the tetragonal ZrO_2 transformed to monoclinic. Zhu et al.[11] observed this behavior when they deposited ZrO_2 by a PLD technique in 20 Pa O_2 ambient at various substrate temperatures ranging from 400^{o}C to 700^{o}C on *n*-Si wafers. With substrate temperature of 400 and 500^{o}C, tetragonal (101) ZrO_2 diffraction peaks were observed, but at 700^{o}C substrate temperature, both monoclinic (022) and tetragonal (101) peaks were observed. In 2001, Ji et al.[12] produced ZrO_2 coatings by reactive dc magnetron sputter deposition technique. When the crystal structure of the coatings were characterized, it was determined that at 500^{o}C of annealing, there was no phase transformation of *t*-ZrO_2, but when the film was annealed at 750^{o}C, small (11-1) and (111) monoclinic peaks were observed beside the (111) tetragonal peak. At higher annealing temperatures, i.e. 850^{o}C to 1050^{o}C, the monoclinic peaks greatly

increased and the (111) tetragonal peak intensity rather decreased which indicated further transformation of the metastable tetragonal phase. Liu et al.[13] also studied this effect by using a rapid thermal annealer, it was also observed that above 750^{o}C, there is a resulting mixture of monoclinic and tetragonal ZrO_2 peaks. The monoclinic content (V_m) in the films were calculated based on the temperature of anneal. They observed an increase in the monoclinic content with increasing annealing temperature. They attributed this effect to the crystallite size of their ZrO_2 particles (48 nm). Their reason was that because the ZrO_2 thin films were composed of very small crystallites, they will have a large fraction of surface regions. This transformation effect was first reported by Garvie[14] in 1965, he determined that, ZrO_2 films with maximum grain sizes of 30 nm demonstrated a tetragonal phase up to approximately 500^{o}C. Above 800^{o}C, a complete transformation occurs and they demonstrate monoclinic phase. But at the intermediate temperatures, partial transformation occurs, and a two-phase region is observed. Garvie postulated that the two phases (monoclinic and tetragonal) are in equilibrium at 300^{o}C when the ZrO_2 crystallite size is 30 nm. The total free energies of these two phases can be expressed as

$$E_m = \propto_m V + \beta_m S, \tag{4.1}$$

$$E_t = \propto_t V + \beta_t S \tag{4.2}$$

Where α is the molar free energy (cal/mol) of ZrO_2 in the form of a large single crystal, β is the surface energy (cal/cm^2) and S is the molar surface (cm^2/mole). The subscripts m and t stand for monoclinic and tetragonal phases, respectively. Thus under the condition of small crystallite size, surface energy plays an important role and dictate any structural change since the surface area per unit volume is large.[15] Garvie also reported that high

temperature tetragonal phase has a surface energy (β_t) of about 770 erg/cm^2, lower than the stable monoclinic phase (β_m) at room temperature, 1130 erg/cm^2. Therefore, although $\alpha_t < \alpha_m$ at a temperature below 1100^{o}C, the tetragonal phase may still be energetically favored giving a small enough crystallite size and thus a large enough *S/V* ratio. As the crystallite size increases with increasing annealing temperature, *S/V* ratio decreases accordingly and the monoclinic phase, the low temperature stable phase of bulk ZrO_2, finally appears. In the $ZnO/Al_2O_3/ZrO_2$ nanolaminate film, the ZrO_2 grain size is approximately 15 nm, thus this phase transformation effect confirms what has been observed by other groups.

4.2 Cross-sectional TEM analysis of the unworn nanolaminate films

Figure 4.7 shows a bright-field cross-sectional transmission electron micrograph (XTEM) images of as deposited and annealed unworn ALD $ZnO/Al_2O_3/ZrO_2$ one trilayer nanolaminate film on a silicon substrate. In order to protect the region of interest from ion beam damage prior to the FIB milling, electron and ion beam assisted Pt were first deposited. From these images, it is evident that;

a. There is a distinct and sharp interfaces that exists between the ZnO, Al_2O_3, and the ZrO_2 layers.
b. Both the ZnO and the ZrO_2 layers are crystalline, and they exhibit columnar grains grown to layer thickness as demonstrated by the XRD results.
c. The Al_2O_3 film is amorphous, and this confirms why there were no Al_2O_3 reflections in the XRD data.

d. At 1000^{o}C anneal, there is a significant reduction in the ZnO layer, the ZnO film diffused through the other layers and mostly settled underneath the ZrO_2 layer. Thus the diffusion of ZnO that was observed in the XPS depth profile is confirmed by the XTEM image. HRTEM also showed a phase transformation of the amorphous Al_2O_3 to a crystalline corundum structure, but this was not observed on the XRD. The thickness of the Al_2O_3 is very small and this is below the detection limit of the XRD. There was also the intermixing of ZnO and Al_2O_3 films near the surface.

e. There is also a phase transformation in the ZrO_2 columnar grains at 1000^{o}C anneal. In the as deposited and 400^{o}C anneal ZrO_2 layers, the structure is more columnar but at 1000^{o}C, the grains are more box-like. XRD confirmed that this is a tetragonal to monoclinic phase transformation.

f. There is an increase in thickness of the ZrO_2 layer at 1000^{o}C anneal, this could be related to the phase transformation since the unit cell for a monoclinic structure is larger than the unit cell of the tetragonal structure due to the high packing density of the monoclinic cell.

g. There is also an increase in the native SiO_2 thickness due to the 1000^{o}C anneal. This increase could be attributed to the diffusion of oxygen through the grain boundaries of the ZrO_2 nanofilm stack which resulted in this significant SiO_2 interfacial growth from ~2 nm to ~50 nm.[16]

h. In Figure 4.7b, the 1000^{o}C annealed ZnO/Al_2O_3/ZrO_2 interface shows that the amorphous Al_2O_3 has transformed to crystalline. This was not observed in the

XRD due to the small thickness of the Al_2O_3. In order to determine the composition of this layer, the d-spacing of the crystals were measured and compared to various XRD PDFs. The d-spacing matched the (111) of $ZnAl_2O_4$ ternary compound. The measured d-spacing value was ~4.65 Å. This observation suggests that there is a reaction between the ZnO and Al_2O_3 layers, thus this layer is not homogenous.

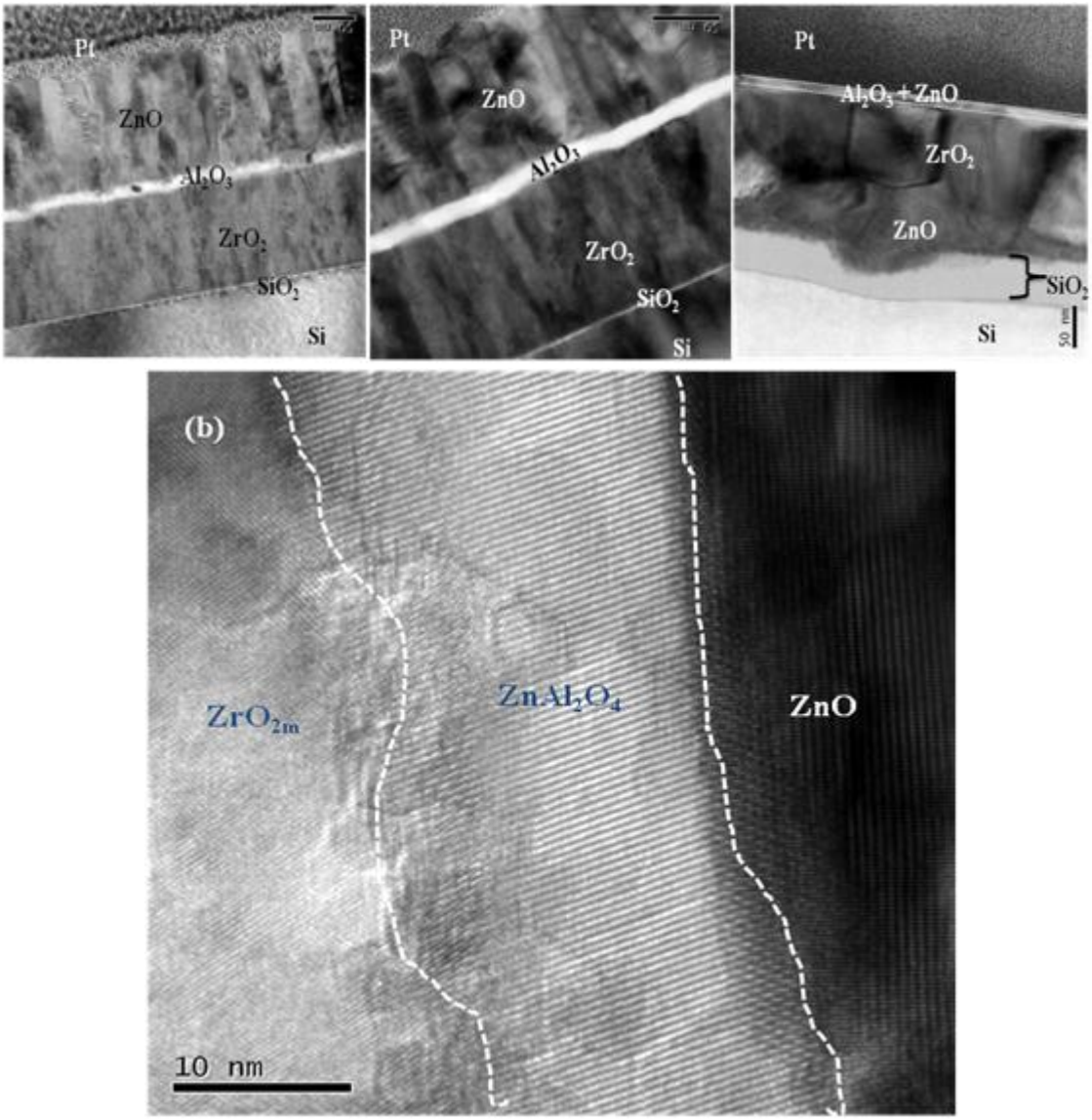

Figure 4.7: XTEM bright-field images for 1 trilayer nanolaminates (left) as deposited, (middle) 400^{o}C annealed and (right) 1000^{o}C annealed. (b) ZrO_2/Al_2O_3/ZnO interface.

In order to determine the cross-sectional composition of the 1000^{o}C annealed films, a couple of chemical EDS analysis were carried out on the unworn sample. Figure 4.8 shows the results of the EDS line scan chemical profile which indicates the compositional variation of the cross-section, the profile is also shown below. From the

EDS line chemical profile scan, a few observations were made: there is the presence of ZnO on the surface of the film, and the ZnO diffusion that was observed by the XPS depth profile and TEM micrograph is also confirmed. It is also observed that the ZrO_2 is sandwiched between the two ZnO layers. The diffusion of the ZnO through the ZrO_2 layer confirms that phase transformation (from tetragonal to monoclinic) that was observed by the XRD. Thus with this transformation, enough space (low packing factor) was created for the ZnO to diffuse through. The Al_2O_3 count that was picked on the line scan was very minimal.

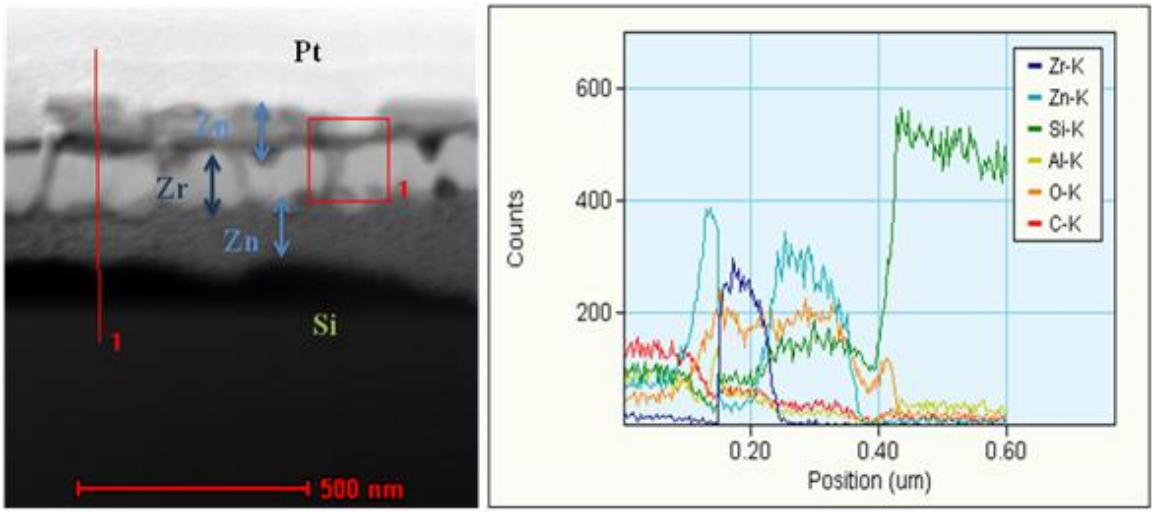

Figure 4.8: XTEM results of unworn 1000^{o}C annealed one trilayer nanolaminate film revealing the microstructure and layer composition.

In order to determine whether the Al_2O_3 was present, EDS chemical mapping was undertaken. Figure 4.9 shows the XTEM image and EDS chemical mapping of the area in the red box. The individual maps indicate the presence of Si, Al, Zn and Zr. The observations that were made by the AES surface mapping are confirmed in this cross-sectional compositional mapping. Thus the surface of the one trialyer nanolaminate film

after 1000^{o}C anneal shows the presence of both Zn and Al on the surface. Even though most of the Al is beneath the ZnO layer, there are some areas that indicate the presence of Al on the surface. Another important observation that was confirmed with this compositional map is the diffusion of ZnO through the ZrO_2 layer. This is also observed in the map. There is some intermixing of the diffused ZnO and the native SiO_2 layers.

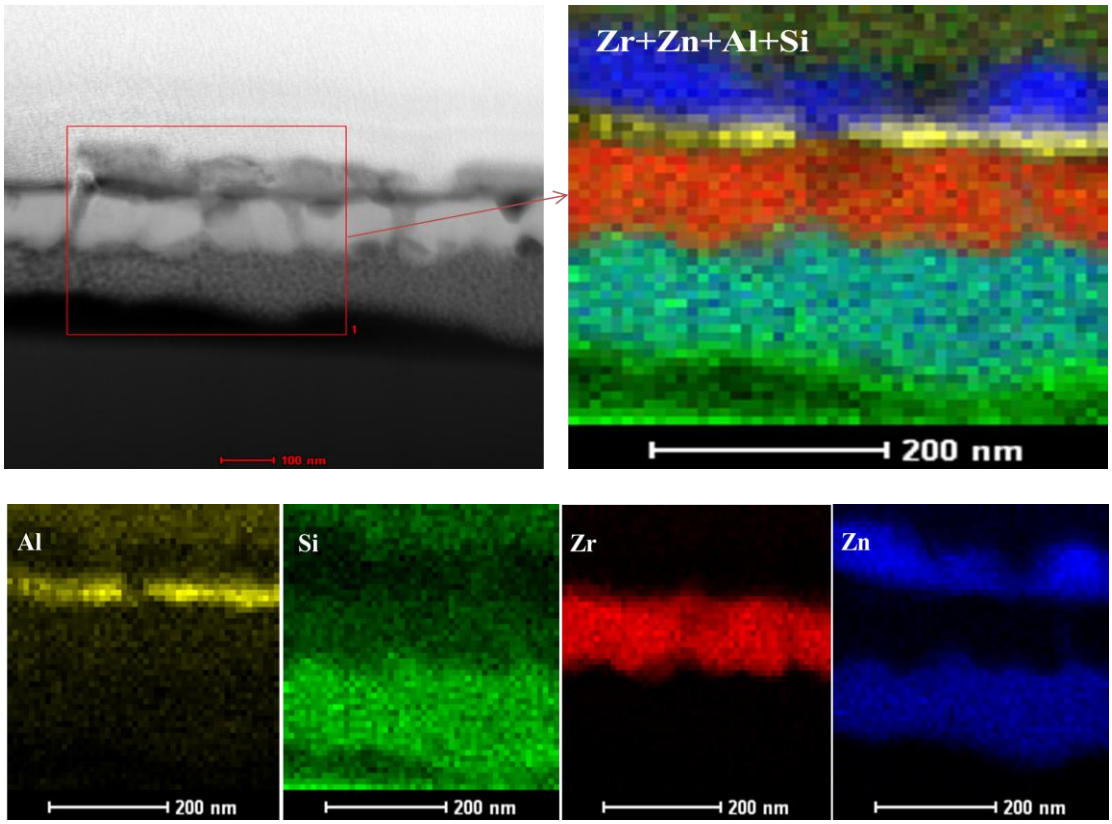

Figure 4.9: XTEM chemical analysis showing chemical maps of unworn 1000^{o}C annealed one trilayer nanolaminate film.

4.3 $ZnO/Al_2O_3/ZrO_2$ One Trilayer Nanolaminate Films Tribological Behavior

The friction coefficient measurements of the nanolaminate films were conducted by using the Falex (Implant Sciences) ISC-200 pin-on-disk tribometer. Tests were set to run to approximately 140 - 200 m with a friction limit of 1.6. When the friction coefficient reaches this friction limit, the test would terminate. For each test, the rotational speed was adjusted to a constant sliding speed of 2.2 cm/s. All tests were performed in a unidirectional sliding mode. A 3.175 nm diameter Si_3N_4 or SS440 C steel balls were used as the counterface to the nanolaminate films.

4.3.1 As-Deposited Friction Test Results

Typical friction behavior curves are shown in Figure 4.10, the plots indicates coefficient of friction (COF) as a function of unidirectional sliding distance (m) for the as deposited one trilayer nanolaminate film. All tests went to completion of 200 m total distance without reaching 1.6 the COF limit set for the tribometer.

In plots (a) and (b), an SS440 C steel ball was used as the counterface material during the friction test. A 50 gram load was used as the hanging weight in plot (a) while 100 gram load was used for the plot (b). The COF of the 50 and 100 gram loads reached steady state friction values of approximately 0.22 and 0.27 respectively. The 50 gram load run started with COF of < 0.2 but increased steadily until it reached the steady state. In the case of the 100 gram load run, the COF started at approximately 0.25, test 1 increased to 0.35 before it reduced to the steady state while test 2 decreased in COF to < 0.2 and steadily increased to 0.3.

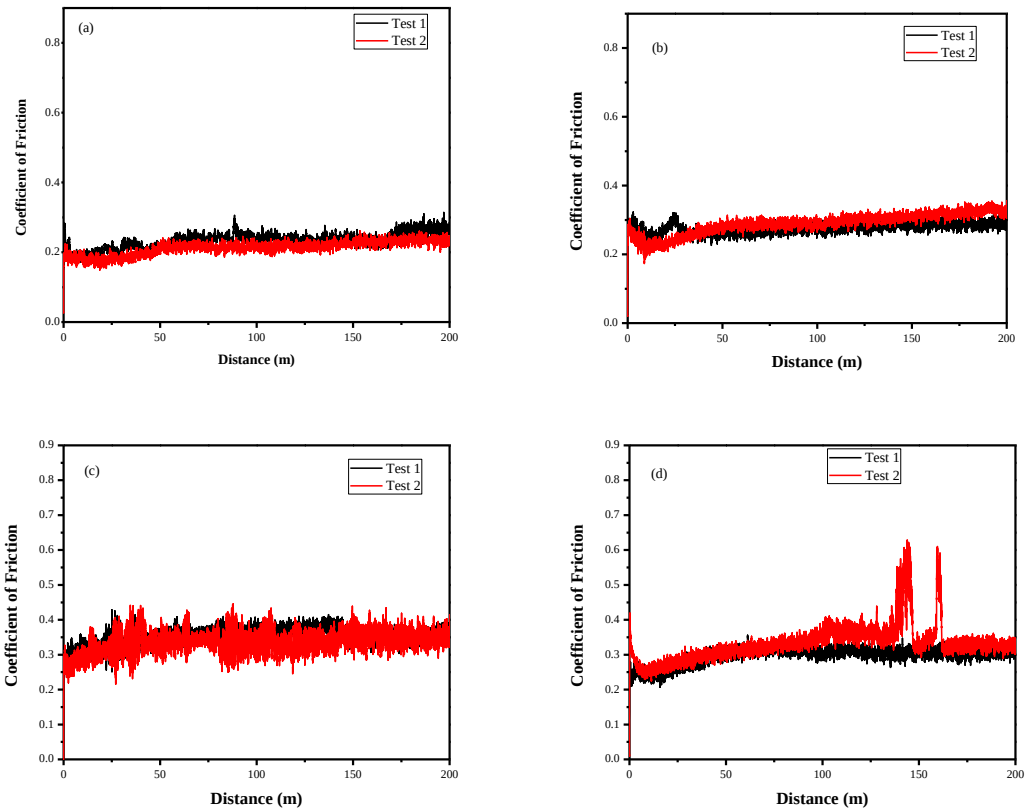

Figure 4.10: Coefficient of Friction measurements of the as-deposited ALD grown one trilayer nanolaminate. (a) 50 gram load with SS440 C ball (b) 100 gram load with SS440 C steel ball (c) 50 gram load with Si_3N_4 ball and (d) 100 gram load with Si_3N_4 ball.

In the case of plots (c) and (d), a Si_3N_4 ball was used as the counterface material during the friction test. A 50 gram load was used as the hanging weight in plot (c) while 100 gram load was used for the plot (d). The COF of the 50 and 100 gram loads reached steady state friction values of approximately 0.34 and 0.26 respectively. In both cases the friction started a little lower and increased steadily to the steady state friction. There was increase in the COF for the test 2 of the 100 gram load at certain points. This anomaly could be due to some debris falling into the wear track. The decrease in the COF with

increase in applied load is confirmed by the Bowden and Tabor theory, i.e. COF decreases with increase in applied load for a sphere on flat contact.

It should be noted that under the same conditions, i.e. same load and running distance, the SS440 C steel ball provided a little lower COF than the Si_3N_4 ball. The increase could be attributed to the properties (hardness) of these two balls. Si_3N_4 is known to be a very tough ceramic with hardness of 9 on the Mohs scale while the SS440 steel ball has a less strong bonding (metallic bonding) and a hardness of 6.5 on the Mohs scale. Due to this toughness properties of the Si_3N_4 material, the interfacial stress is expected to be high (Bowden and Tabor theory) than that of the SS440 C steel ball, thus during unidirectional sliding it is expected that COF of the Si_3N_4 should be higher than the SS440 C steel ball.

4.3.2 400^{o}C Annealed Friction Test Results

Figure 4.11 shows a comparison of the COF plots of the 400^{o}C annealed one trilayer films. All tests went to completion of 140 and 200 m in distance respectively without reaching the 1.6 COF limit set for the tribometer. In plot (a), an SS440 C steel ball was used while a Si_3N_4 was used for plots (b) through (d). In plots a and b, a 50 gram load was used as the hanging weight, in plot c, a 100 gram load was used while in plot d, a 250 gram load was used.

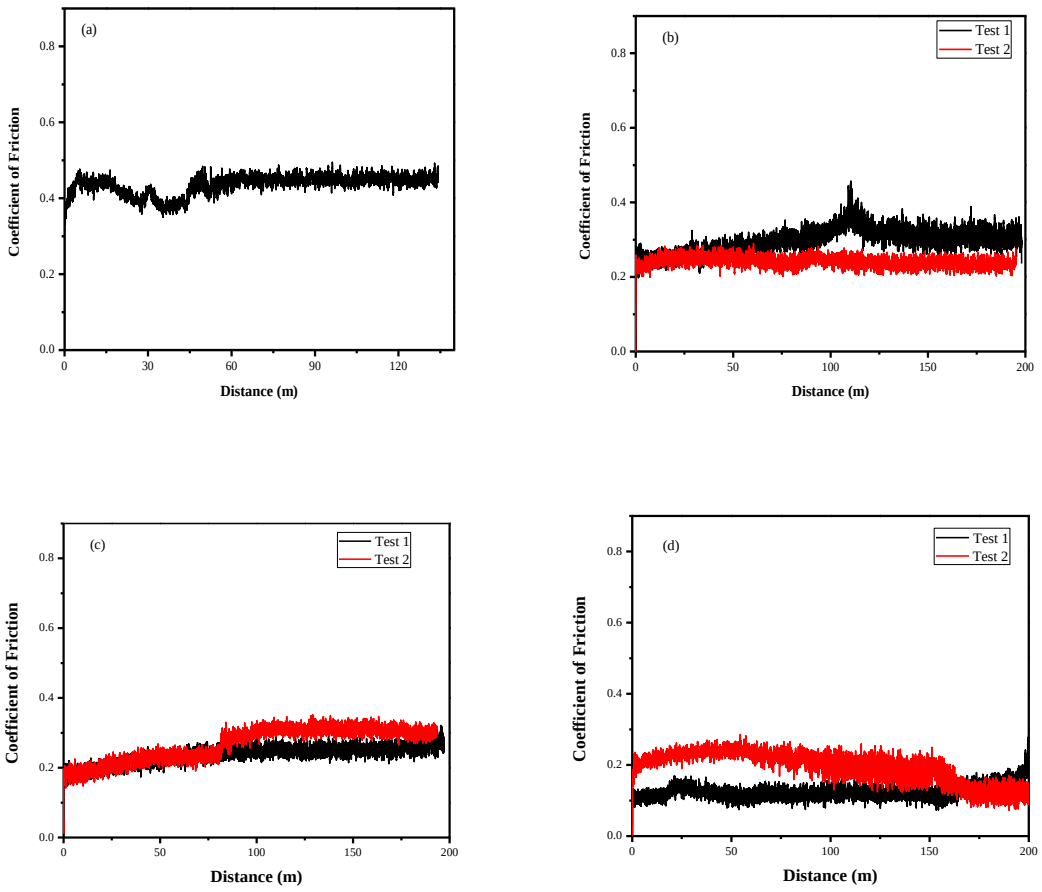

Figure 4.11: Coefficient of Friction measurements of the 400^{o}C annealed ALD grown one trilayer nanolaminate. (a) 50 gram load with SS440 C steel ball, (b) 50 gram load with Si_3N_4 ball, (c) 100 gram load with Si_3N_4 ball and (d) 250 gram load with Si_3N_4 ball.

The steady state COF of plot (a) is approximately 0.45, while plots b through d have steady state COF of approximately 0.27, 0.23 and 0.18. Two important observations from the data above is that firstly, for the Si_3N_4 ball 400^{o}C annealed films, the COF data values achieved were lower than the as deposited under similar conditions. Secondly, there is a decrease in the steady state friction with increase in the applied load. This trend

is observed in both the as-deposited and the 400^{o}C annealed samples. This is in agreement with the Bowden and Tabor (equation 3.10) Hertzian contact model.

4.3.3 1000^{o}C Annealed Friction Test Results

Figure 4.12 shows the effect of high temperature anneal prior to friction test. All the tests went to completion of 200 m distance without reaching the 1.6 COF limit set for the tribometer. A Si_3N_4 ball was used in all the friction tests, in plot (a) a 25 gram load was applied, test 1 started with a very high COF but stabilized to approximately 0.6, test 2 started with a lower COF but also stabilized at approximately 0.45. With 50 gram load (plot b), the steady state COF is approximately 0.5, when a 100 gram load (plot c) is applied, the steady state friction reduced to approximately 0.3. It should be noted that the COF trend also follows the Hertzian contact model, which is as load increases the low COF is observed. In comparing the COF data for the three conditions above, the 1000^{o}C anneal are comparably higher than the 400^{o}C anneal and the as-deposited nanolaminate one trilayer.

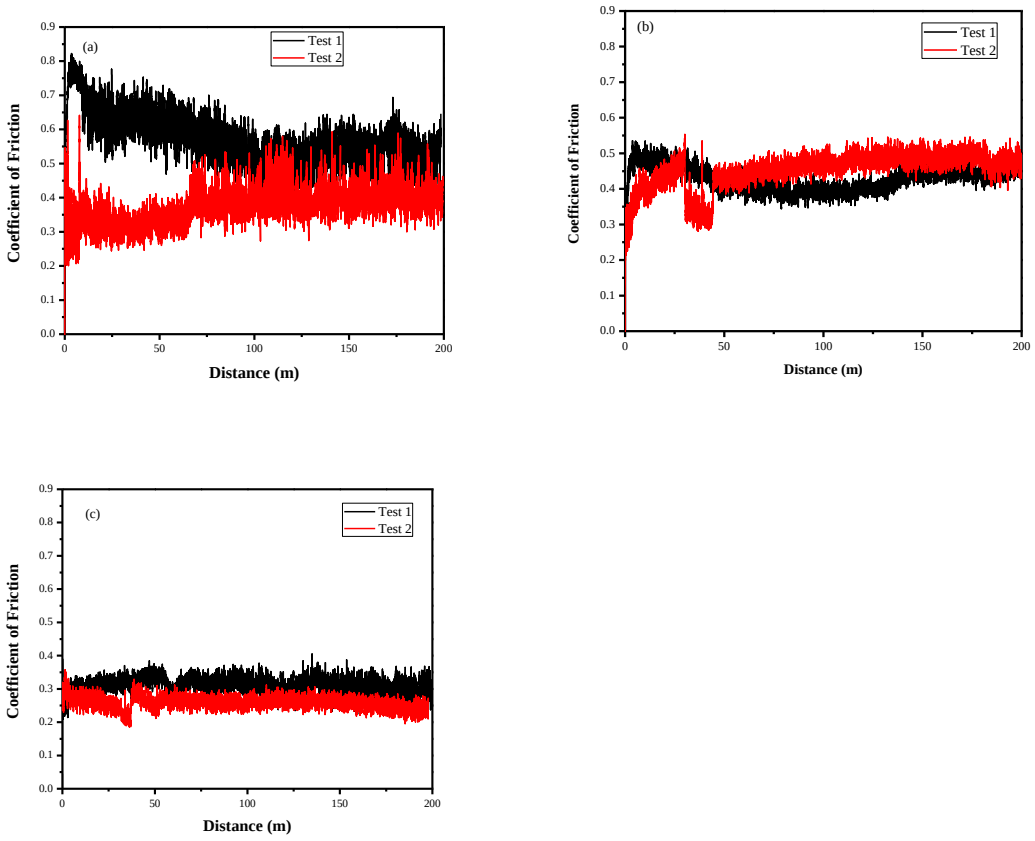

Figure 4.12: Coefficient of Friction measurements of the 1000^{o}C annealed ALD grown one trilayer nanolaminate. (a) 25 gram load (b) 50 gram load and (c) 100 gram load. Si_3N_4 ball was used as the counterface material during the friction test.

The increase in the COF after 1000^{o}C anneal could likely due to many reasons; the increase in the (0002) grain size during the heat thermal treatments. As confirmed by the XRD data, the (0002) peaks become narrower with increase in the annealing temperature. With the narrowing of peaks, the grain size increases according to the Debye Scherrer formula. There was an observation of the mixing of the ZnO and Al_2O_3 layers near the surface, this could be a hard phase and may lose the lubricity properties, this will also contribute to the increase in the COF. Another important observation that

was made is the loss of significant amount of lubricious ZnO on the surface. Since the ZnO was acting as the lubricating layer, loosing this layer is just like wearing off the layer with time during sliding. Finally, the transformation of the ZrO_2 from tetragonal to monoclinic could also contribute to the increase in friction as this is a transformation toughening. Figure 4.13 confirms that there is a toughening mechanism going on with the 1000^{o}C annealed trilayer. There is significant amount of wear on the ball, thus the annealed trilayer is forming a hard coating which is wearing off the ball. Smaller amounts of transferred film were observed on the balls, this transferred film is not thought to be lubricious, and it could be a mixture of the film from the ball and the wear track. There is also an increase in the worn area of the Si_3N_4 ball with increase in the applied load.

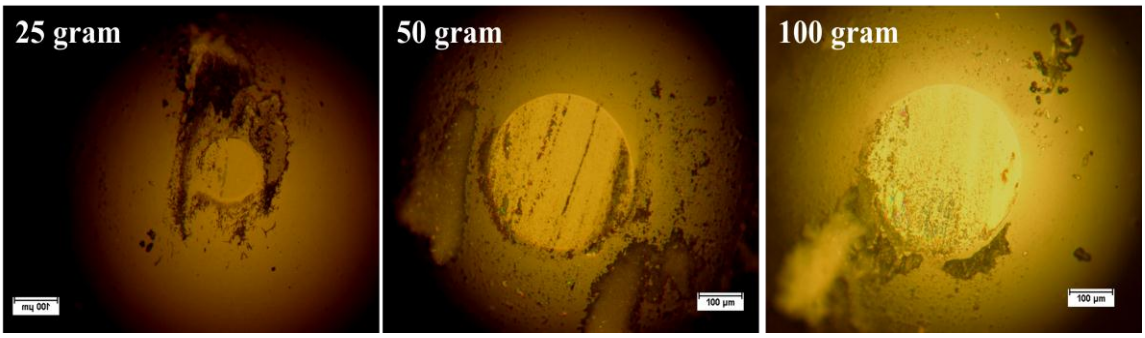

Figure 4.13: Optical microscope images of the Si_3N_4 balls used to test the COF. From left is the 25 gram, 50 gram and 100 gram load pin balls respectively.

Another aspect of tribological behavior that was studied was to determine the amount of material removed during the friction test. In order to measure the volume of material removed, the wear surface was recorded by a stylus profilometer. The worn area was measured in at least five different locations and the wear volume was calculated from the mean value of each wear track. The wear factor was determined by using the equation

$$WF = \frac{V}{LD} \left(\frac{mm^3}{Nm}\right) \quad (4.3)$$

where V is the wear volume, L the normal force and D is the sliding distance.[17] The wear factor is a tribological property to measure the wear behavior of the films, in which a low wear factor represents a good wear resistance.

Figure 4.14 shows the wear factors that were obtained for the above nanolaminate films. Figure 4.14a shows the wear factors for the as-deposited nanolaminate film. It was determined that the SS440 C steel ball produced less wear than the Si_3N_4 ball wear tracks. In Figure 4.10b, the 400^{o}C annealed samples indicate a slightly higher wear factors. The 1000^{o}C annealed films have the highest wear factors with the wear factors increasing with increase in applied load. From Figure 4.13, it was observed that the area of the worn pin increases with the applied load. This has effect on the wear factor that was calculated. This is because the worn area of the nanolaminate trilayer also increased as the applied load increased, thus, the volume of the worn area also increases with increasing applied load. With an increase in worn volume, there is an increase in the wear factor.

The wear factors of each condition are approximately an order of magnitude larger than the wear factors of the next condition. A wear factor on the order of 10^{-3} is considered severe wear, while 10^{-5} is considered as mild wear and 10^{-6} and 10^{-7} are considered low wear. Based on these regimes, all of the above coatings are in the low wear regime.[18] It should be noted that there is a direct correlation between the COF and the wear factor, as observed in this case, the wear factor increase with increase in COF. The obtained results show that the wear factor values compare very well to other solid lubricant coatings (MoS_2[19] and diamond-like nanocomposite (DLN)[20]) in dry

environment.

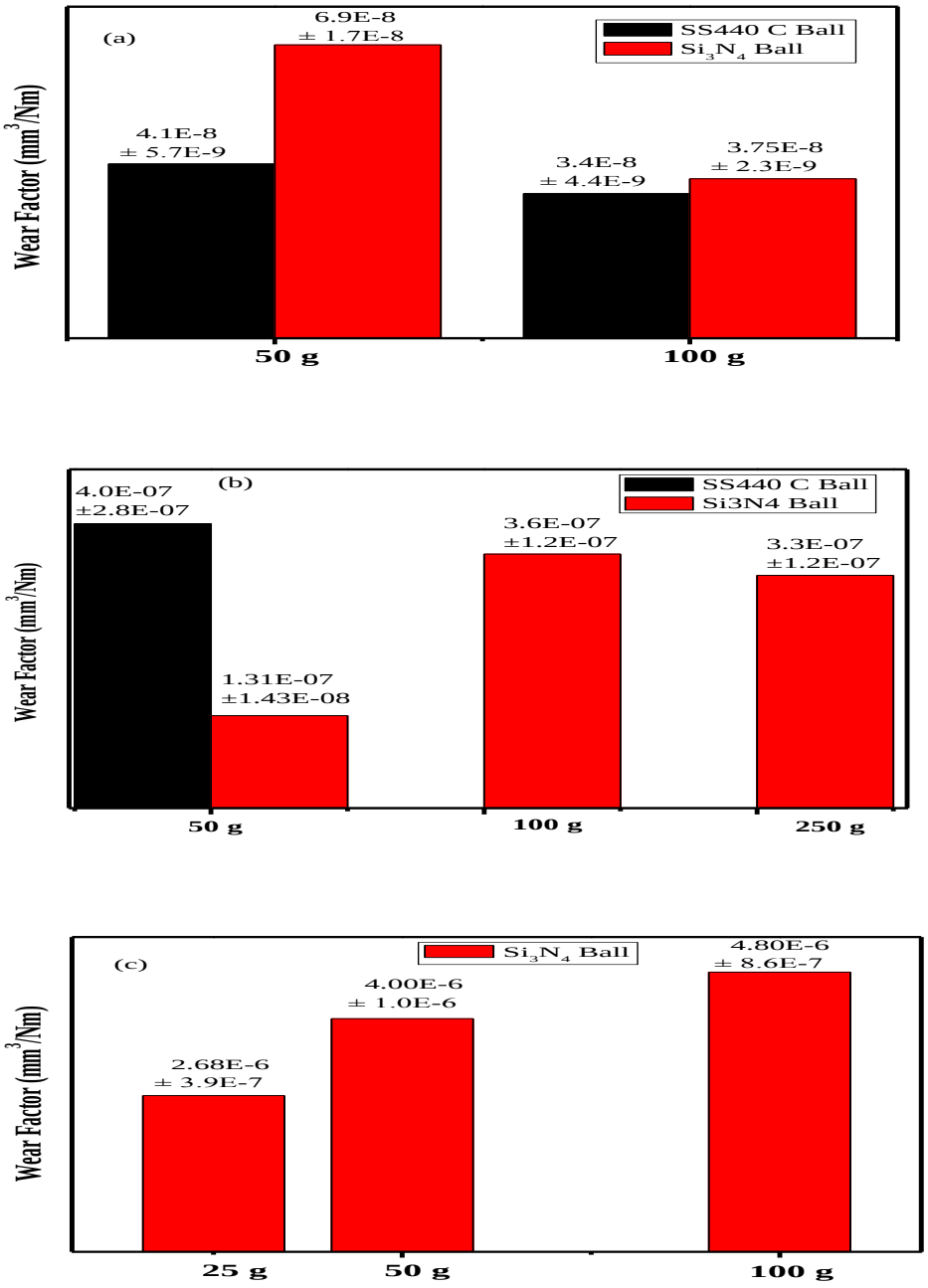

Figure 4.14: Calculated wear factors of the wear tracks (a) As-deposited, (b) 400^{o}C annealed and (c) 1000^{o}C annealed nanolaminates one trilayer.

4.4 Chemical imaging of wear tracks with auger electron spectroscopy

During pin-on-disk test, there is a lot of film transfer either from the pin ball into the wear track or from the wear track onto the pin ball. The transferred film (third body) could enhance or deteriorate the lubrication mechanism, this makes the chemical composition of the wear track very important to be studied. With regards to this, the chemical composition inside the wear track is expected to be different from the outside due to the transferred film. In order to analyze the chemical composition inside the wear tracks, a high spatial resolution chemical imaging was done by mapping the wear tracks using the detected auger electrons. Due to the surface sensitivity and small analysis volume of auger electron spectroscopy (AES), it is known to be one of the ideal analytical techniques for a chemical compositional and mapping characterization of submicron particles. The small analysis volume ensures that the ratio of signal generated by the particles to signals originating from the surrounding materials is favorable even down to particles sizes of nanometers. AES's higher sensitivity for light elements also ensures that no elements will be missed by this technique (with exception of hydrogen or helium).

Figures 4.15 and 4.16 shows SEM images and chemical maps of as deposited sample. In Figure 4.15, a 100 gram load with SS440 C pin ball as deposited tilayer film wear track was analyzed. The mapped elements included iron, zinc and oxygen, the individual element maps shows a high concentration of both zinc and oxygen which resulted from the ZnO deposited film. There is also iron present in some parts of the wear track, the overlayed map indicates a yellow color which is a mixture of red and green

colors (iron and oxygen). The iron present in the wear track is a transferred film from the SS440 C steel ball. The Figure 4.16 also shows another wear track with 100 gram load and a Si_3N_4 pin ball as deposited trilayer film, it is observed once again that there is a high concentration of zinc and oxygen that resulted from the deposited ZnO.

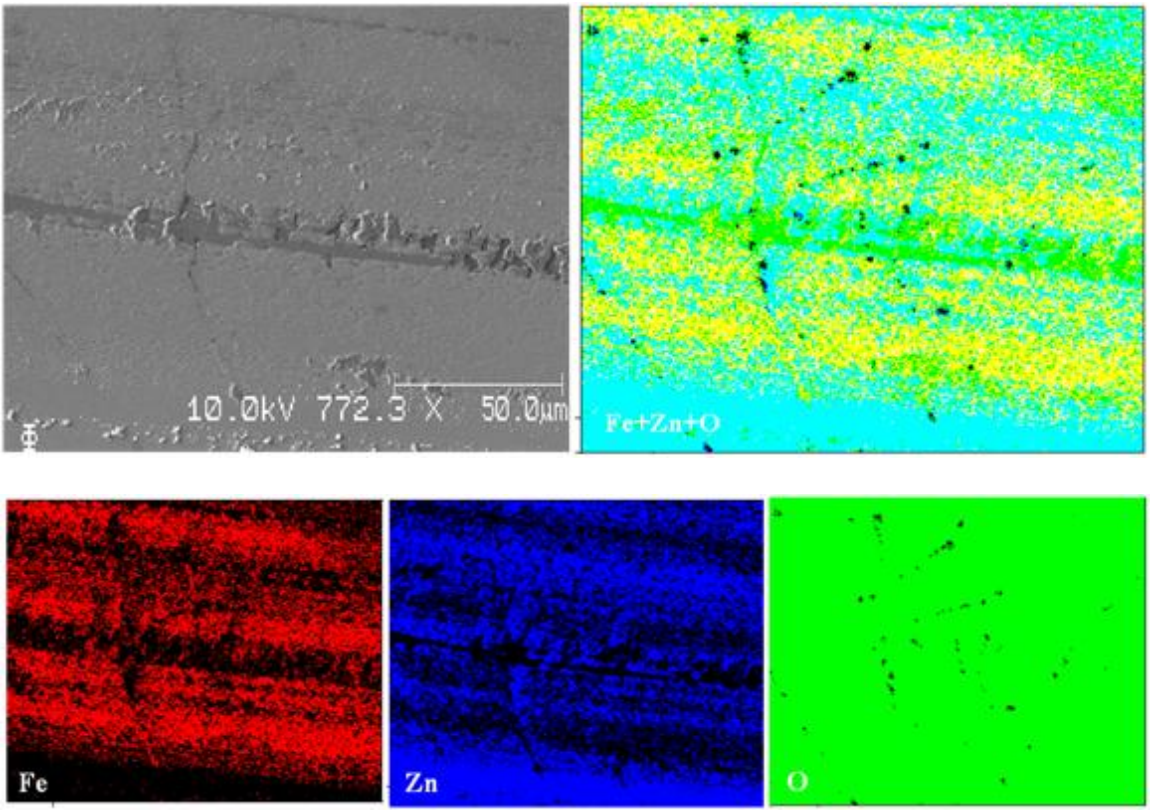

Figure 4.15: Secondary electron image and Auger images (Fe, O and Zn) of 100 gram load wear track with SS440 C steel ball of as-deposited one trilayer.

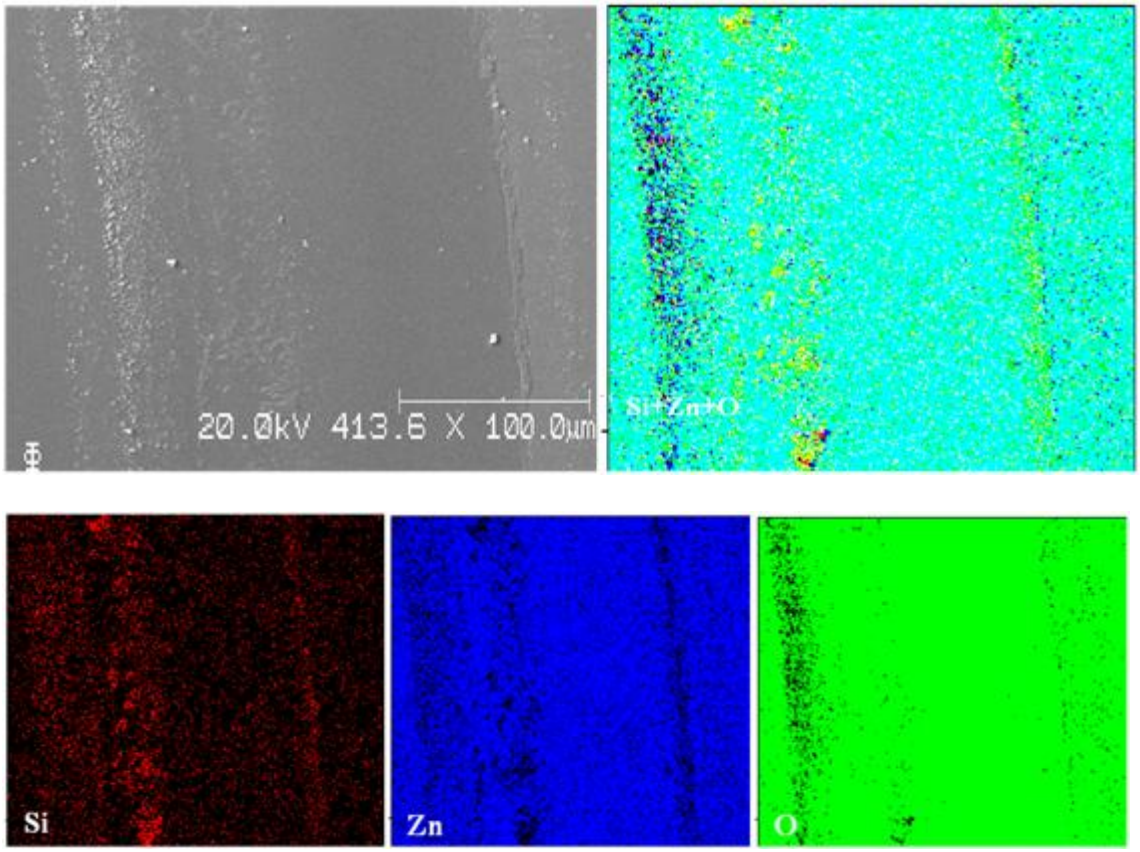

Figure 4.16: Secondary electron image and Auger images (Si, O and Zn) of 100 gram load wear track with Si_3N_4 ball of as-deposited one trilayer.

There are also streaks of silicon inside the wear track that forms SiO_2 with the oxygen. This is obvious in the overlayed map, where the yellow streaks indicate the SiO_2 inside the wear track. In comparing the above two figures, it is observed that the concentration of iron inside the wear track is higher than that of silicon. This is because the Si_3N_4 ball is harder than SS440 C ball, thus less film is worn from the Si_3N_4 ball into the wear track than the SS440 C ball. Both wear tracks did not show any sign of the presence of either aluminum or zirconium, this confirms that the ZnO film is not worn out after the 200 m run.

Due to the high wear of SS440 C steel ball, it is prudent to determine if the iron oxide has any influence on the friction coefficients that were recorded. It has been reported that γ-Fe_2O_3 films have relatively low friction coefficient (~0.25) while Fe_3O_4 has a high friction coefficient (~0.6).[21] Thus the iron oxide that was forming in the wear track could have a lot of influence on the COF behavior of the one trilayer films. In order to determine the iron oxide type present inside the wear track, an XPS high resolution scan was undertaken. Since both Fe_2O_3 (a=0.8350 nm) and Fe_3O_4 (a=0.8396 nm) have nearly the same lattice parameters from the cubic inverse spinel structure, the possibility of the presence of either compounds could not be ruled out by XRD patterns only.[22,23] Thus to obtain more evidence, XPS analysis was required. From a typical Fe_{2p} XPS spectrum, a remarkable observation is made of the two compounds, that is a broadening of $Fe_{2p}^{3/2}$ peak (~711 eV) and the appearance of a shoulder (~709 eV) on the high-energy side of $Fe_{2p}^{1/2}$ peak (~724), which are all characteristics of Fe^{2+} in Fe_3O_4. Another striking feature of the spectrum is that, there is a satellite line that is situated at about 719 eV, which is a characteristic of Fe^{3+} in γ-Fe_2O_3.[24,25]

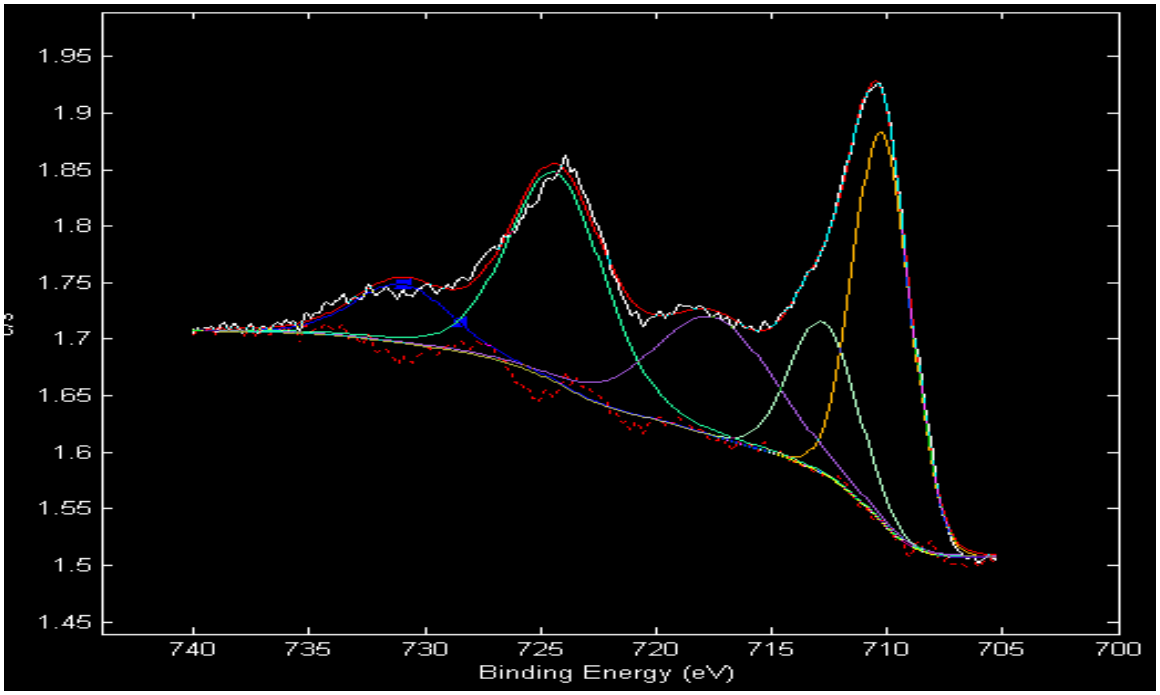

Figure 4.17: XPS high resolution scan of iron peak.

Figure 4.17 shows a high resolution deconvoluted iron peak XPS scan, the major peaks present are Fe2p3 and Fe2p1. It is obvious from this figure that there is no shoulder peak around 709 eV but there is a satellite peak around 719 eV. Thus it could be concluded that the iron present in the wear track forms γ-Fe_2O_3. As already mentioned the COF for γ-Fe_2O_3 is low and may influence that of the ZnO film. Hence in chapter 5 only the Si_3N_4 ball was used as the counterface during the COF test.

As already discussed in figure 4.3c, the XPS depth profile of the 1000^{o}C annealed trilayer film indicated the presence of both zinc and aluminum on the surface of the film. Figure 4.18 shows the SEM image and an auger chemical map of the surface of the 1000^{o}C annealed trilayer film. The surface confirms the presence of both zinc and aluminum as observed in the XPS depth profile. The zinc is color coded red while

aluminum is green, and the overlayed plots shows both are present on the surface. Figure 4.19 also shows the SEM images and auger chemical maps of inside the wear track of a 100 gram load and Si_3N_4 ball of the 1000^oC annealed one trilayer film. In Figure 4.19a, the map indicates the presence of zinc (red), aluminum (green) and silicon (blue). The overlayed plot shows a streak of zinc across the wear track while the bottom part is dominated by silicon, there are spots of aluminum near the top of the map. The presence of silicon could be as a result of the Si_3N_4 ball wearing and leaving traces inside the wear track or it could be as a result of Si from the substrate. The zinc present inside the wear track is also believed to have resulted from the diffused zinc during the thermal anneal. These assumptions will be studied with XTEM EDS chemical composition line scan and compositional mapping. In order to determine whether there is zirconium present inside the wear track, another map was done.

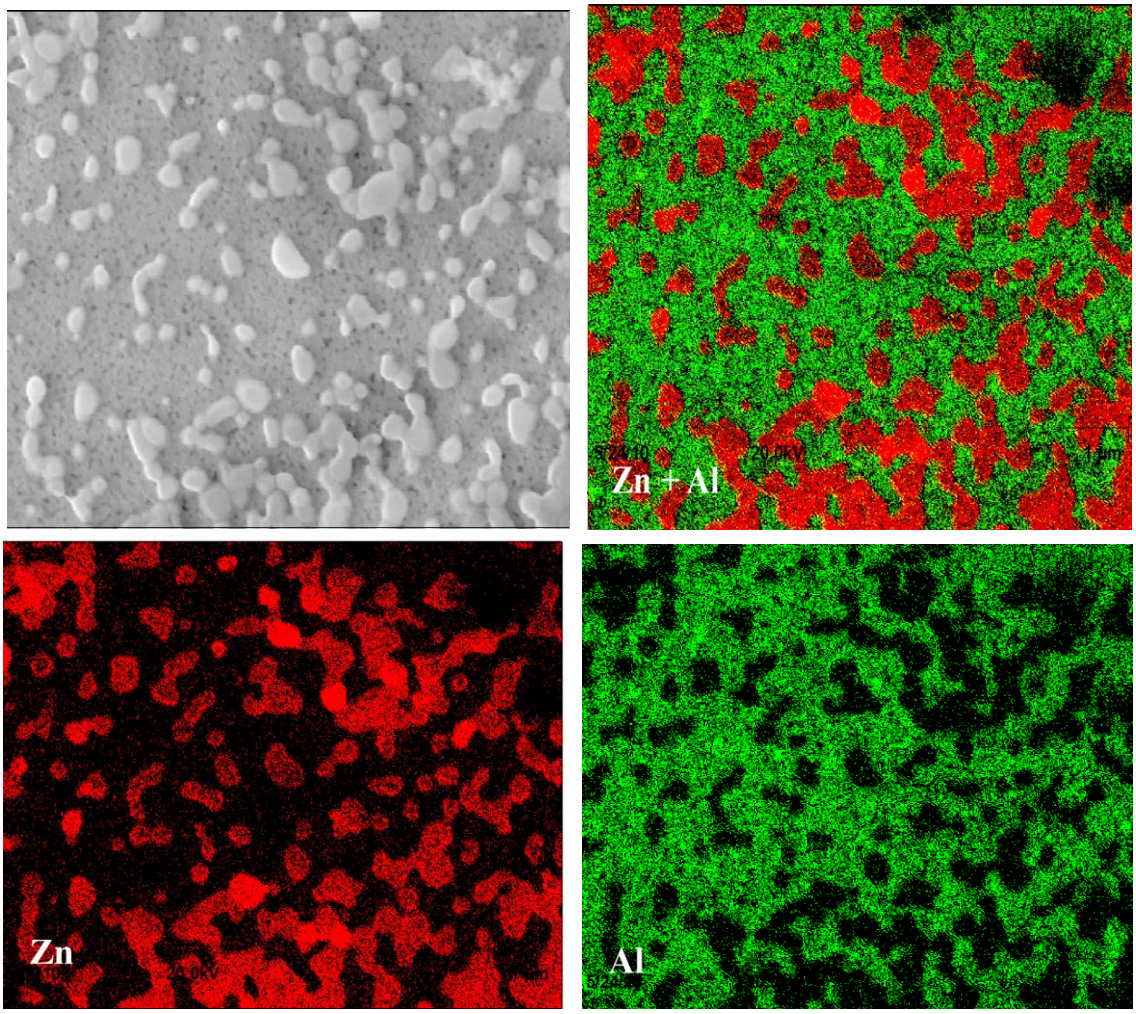

Figure 4.18: Secondary electron image and Auger images (Zn and Al) of the surface of 1000^{o}C annealed trilayer film.

Figure 4.19b shows an auger chemical map for zirconium (blue) and an overlayed map of zinc (red), aluminum (green) and zirconium (blue). The presence of zirconium inside the wear track is obvious in the overlayed map. Thus it could be concluded that at 1000^{o}C anneal, there is an intermixing of layers, and this is not appropriate for lubrication. Finally, it was observed that most of the zinc and aluminum on the surface were worn out during the friction of friction test.

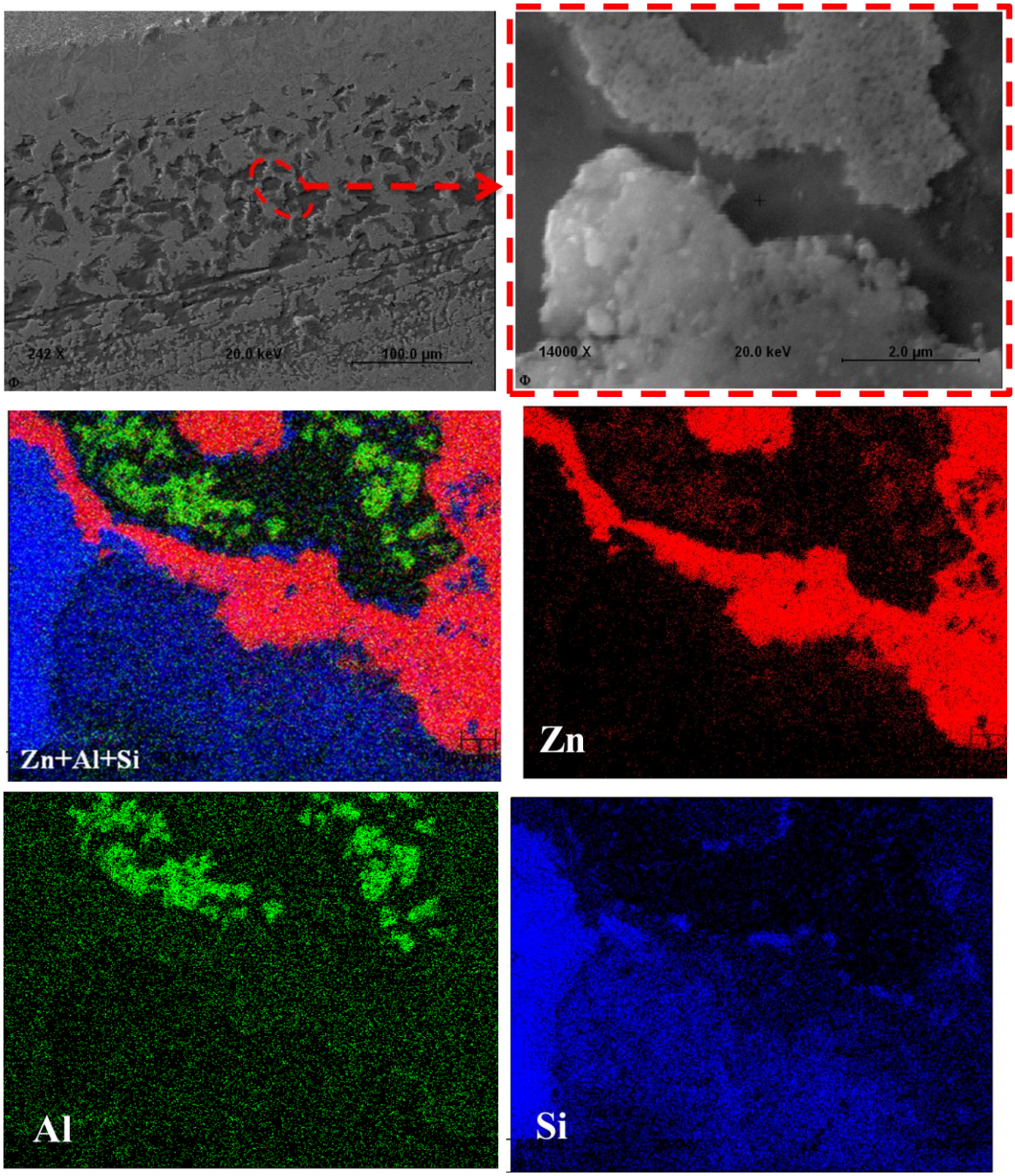

Figure 4.19a: Secondary electron image and Auger maps of Zn, Al, Si and an overlayed map of 100 gram load wear track with Si_3N_4 ball of 1000^{o}C annealed one trilayer film.

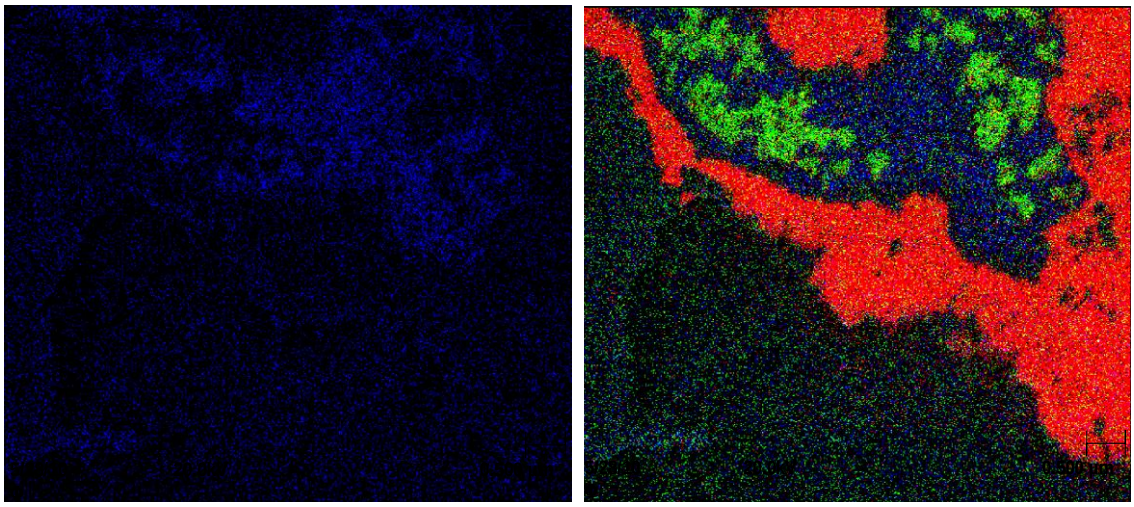

Figure 4.19b: Auger maps of Zr and an overlayed Zn, Al and Zr of 100 gram load wear track with Si_3N_4 ball of 1000^{o}C annealed one trilayer film.

4.5 Cross-sectional TEM Behavior of Worn One Trilayer Films

Recall from reference 17 that peak broadening (FWHM $\geq 0.3^{o}$) by XRD has been linked to growth defects (lattice imperfection): low/high angle grain boundaries, non-uniform strain, dislocations and stacking faults that lie on the (0002) basal plane. Thus it is necessary to perform a TEM cross sectional analysis inside the wear tracks of the one trilayer films to elucidate if any of these growth defects are responsible for the solid lubrication mechanisms that were observed for the lubricity in the nanocrystalline oxide. If the lubrication mechanism is not due to any of these growth defects, the XTEM analysis can help establish what other mechanisms that might be taking place during the friction test.

Figure 4.20 shows a HRSEM image of the as deposited one trilayer 50 gram load with Si_3N_4 ball which indicates the location of the FIB cut. The FIB cut was done at the center of the wear track and in the direction of the pin on disk sliding.

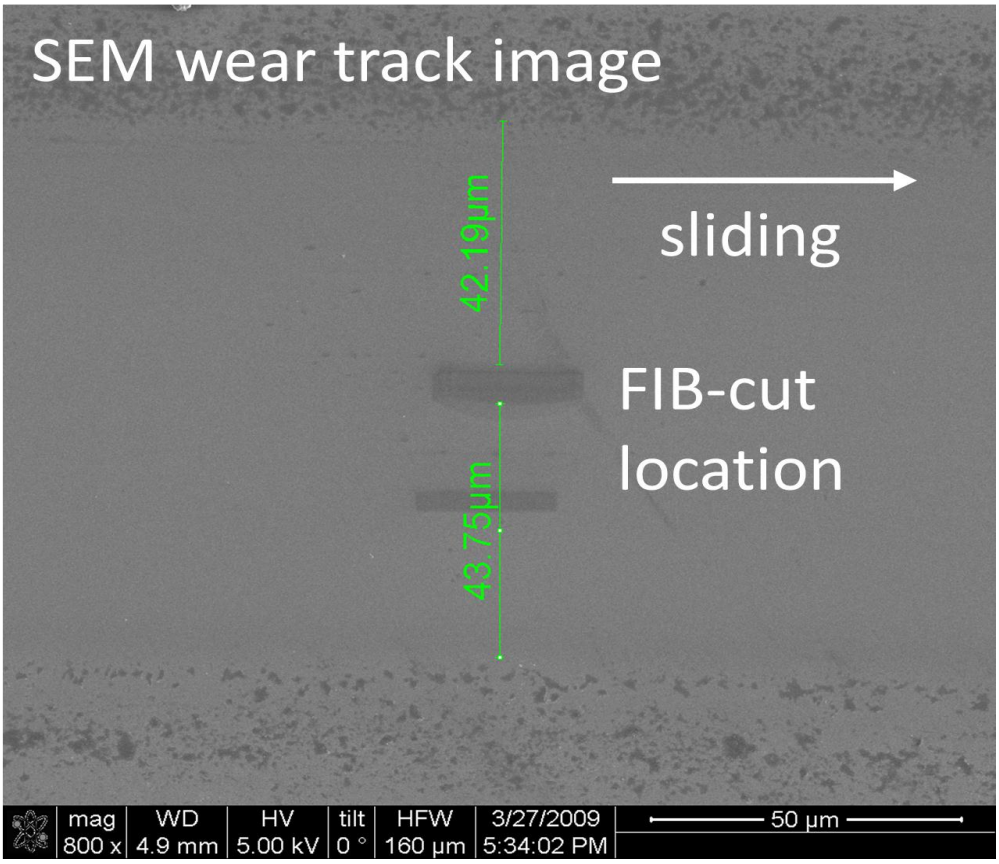

Figure 4.20: HRSEM image of one trilayer of 100 gram load with Si3N4 pin ball showing location of cross-sectional FIB-cut.

4.5.1 As-deposited One Trilayer

Figure 4.21 shows the cross-sectional TEM (XTEM) image of as-deposited worn wear track of 50 gram load with Si_3N_4 ball. This is after 100 m sliding distance, and based on this and the unworn images shown in Figure 4.7, several observations can be made on the effect of the cyclic sliding. As observed in Romanes[10] work, there were micro-cracks after the load was applied on the ZnO, no micro-cracks (no brittle fracture) were observed in this trilayer after the 200 m sliding distance even though higher loads and longer sliding distances were undertaken in this work. This could be attributed to the

presence of the ZrO_2 layer which is serving as a load bearing layer in this case. No cracks/micro-cracks were observed in any of the other loads that were tested.

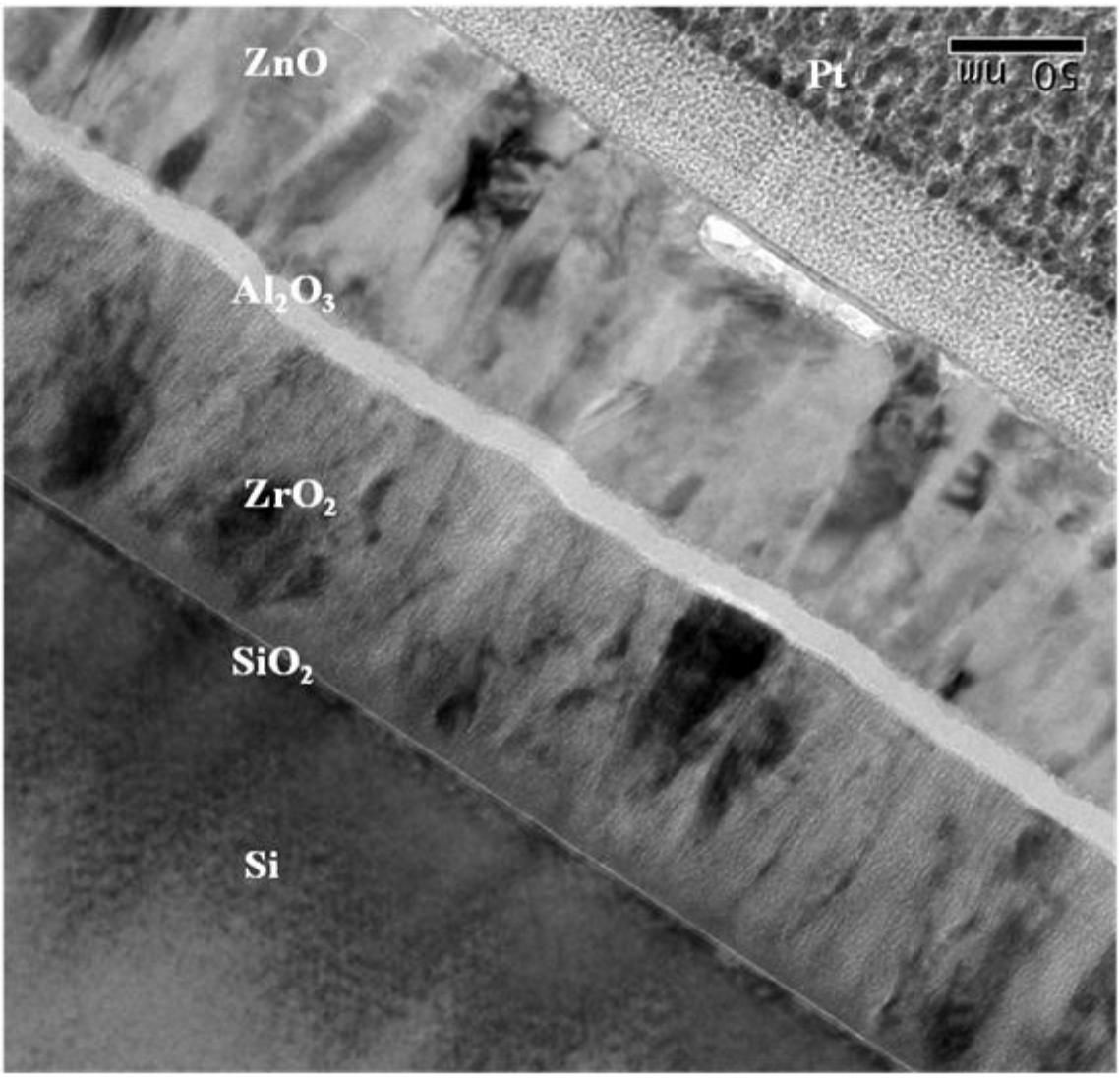

Figure 4.21: XTEM image of as-deposited worn one trilayer.

The amount of ZnO that was worn out after such a long run is very minimal, thus very low wear is inside the wear track. Comparing the worn versus unworn once again shows some evidence of grain re-orientation and bending of the ZnO grains near the top

of the worn trilayer. This shows that some form of plastic deformation occurred in the ZnO layer during sliding. In Figure 4.22, a magnified view of the ZnO with applied stress of 100 gram which has produced the wearing of the film is shown. It is apparent to note that the top part of the ZnO layer has transformed from columnar to mix-amorphous-crystallite layer, this makes it easy for the film to accommodate interfacial shearing. The plastic deformation occurring in the nanocrystalline ZnO layer contributes to the continuous decrease from crystalline to amorphous. Hence for this nanolaminate, the applied stress was being used to transform the columnar grains to progressively smaller crystals and eventually to amorphous ZnO, and shearing the ZnO layer across the surface to accommodate the sliding motion of the ball, i.e. the velocity accommodation mode is intrafilm shear.

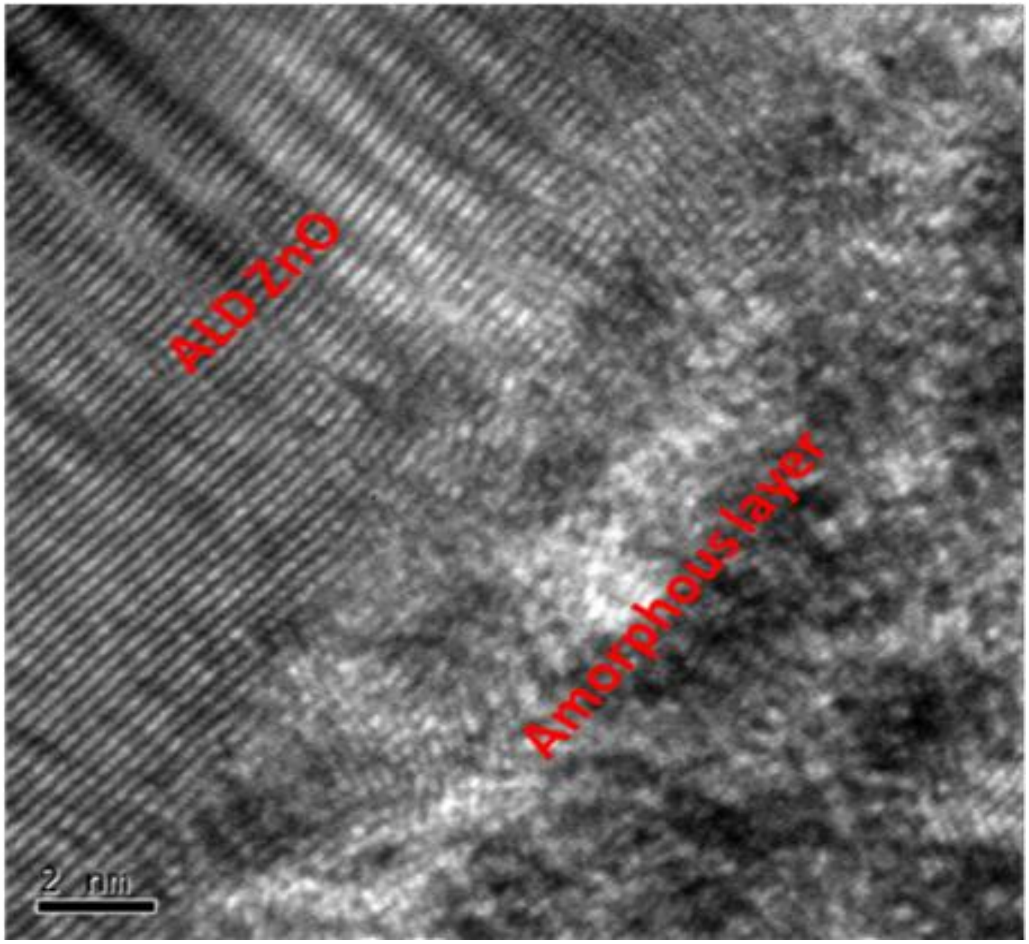

Figure 4.22: XTEM micrograph of worn one trilayer film, the amorphous layer shows the worn ZnO.

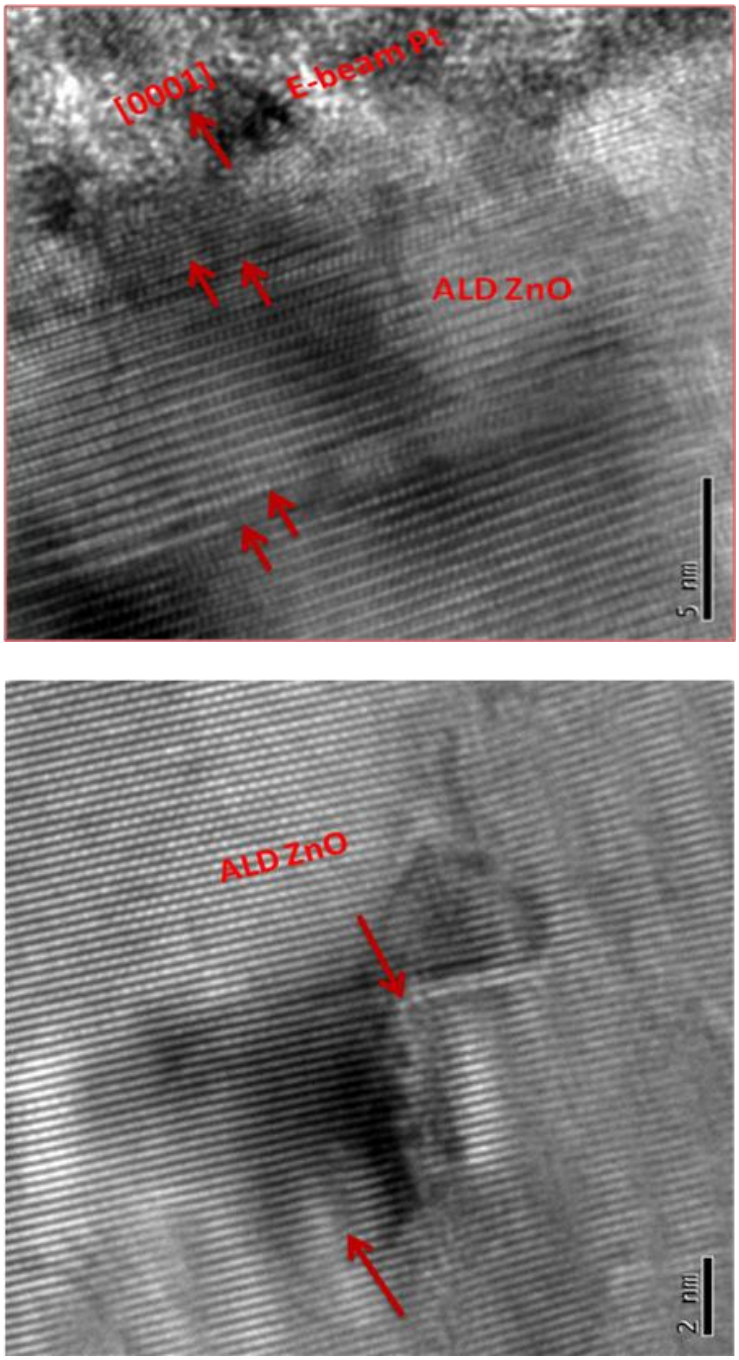

Figure 4.23: XTEM micrograph of worn as-deposited one trilayer film showing (top) ZnO basal stacking faults along the [0001] growth direction, (bottom) ZnO partial dislocations on the (0002) basal plane.

Figure 4.23 top shows XTEM inside the one trilayer wear track (Si_3N_4 ball at 50g load). It is observed that the microstructure of the nanolaminate is dominated by stacking faults that are bordered by partial dislocations (PD). The basal stacking faults (BSFs) are connected to the unfaulted crystals by these PDs. The BSF may originate from incoherent boundaries between adjacent columnar grains or condensation of vacancies or interstitial, so that a missing or extra (0002) plane will be introduced into the lattice. It should also be noted that the {0002}-basal planes are low surface energy planes and have low stacking fault energies (SFE), while the {10-10}-prismatic and {10-11}-pyramidal planes are high surface energy planes and have high SFEs.[26] Thus, it is not surprising that in Figure 4.23 (top) that BSFs are present along the {0002}-basal planes. The identification of these dislocations is confirmed by Figure 4.23 (bottom) which demonstrates that each PD corresponds to additional (0002) plane.

4.5.2 400^{o}C Annealed One Trilayer

The cross sectional TEM micrograph of the worn 400^{o}C annealed one trilayer film is shown in Figure 4.24. Once again it is observed that only the ZnO layer experiences any form of deformation. The deformation observed in the 400^{o}C annealed sample is very similar to that of the as-deposited sample. There was no brittle fracture or any micro-cracks in any of the deposited layers after the sliding. There is minimal thinning of the ZnO layer, hence, very low wear was observed inside the wear track. There was also some nanocolumnar grain bending near the top of the worn trilayer. The insert shows the presence of some plastic deformation near the top of the ZnO layer. The increased amount of plastic deformation which are likely to be dislocations (red arrows)

is known to enhance the lubricity in oxide ceramics.

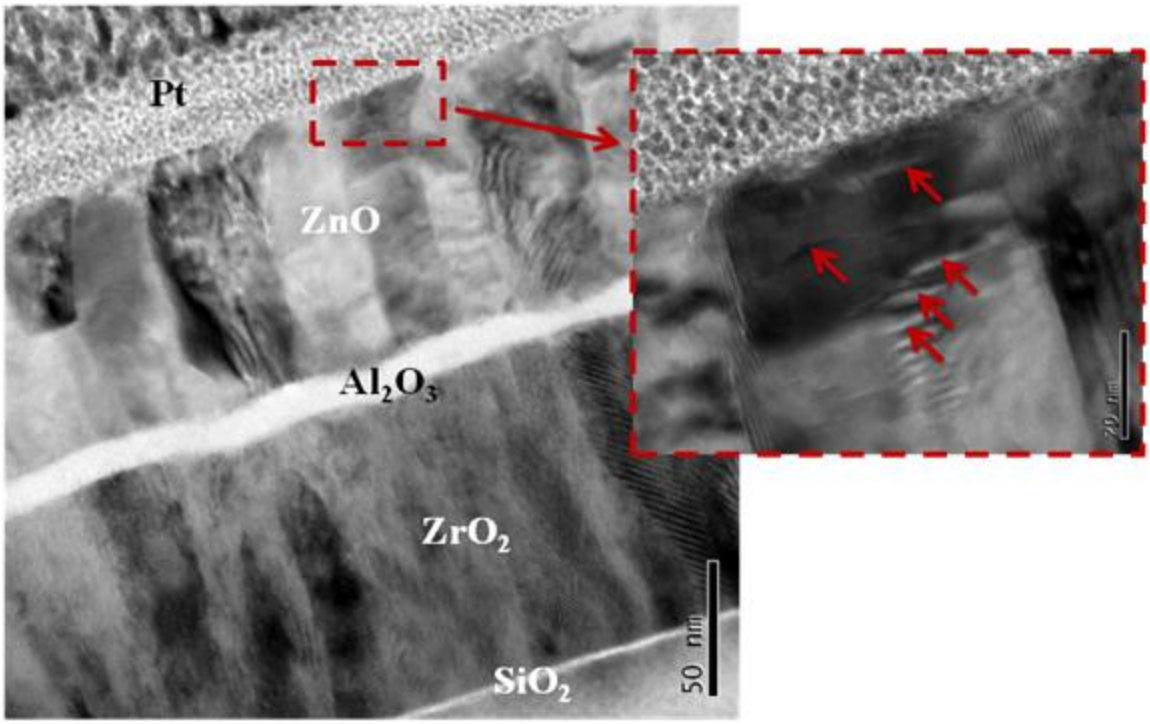

Figure 4.24: XTEM image of 400^{o}C annealed worn one trilayer. Insert image shows a magnified micrograph of one of the ZnO nanocolumnar grains near the surface where the presence of defects and shearing of the columnar grains are observed.

As previously stated, the broadening of the peak (FWHM $\geq 0.3^{o}$) has been linked to growth defects such as low/high angle grain boundaries. In this case, since the columnar grains form low angle grain boundaries, this (0002) peak broadening is not due to high angle grain boundaries, which means the other defects may be operative. Figure 4.25 shows a low angle grain boundary in the ZnO film that was observed. This low angle grain boundary may be one of the contributors of the (0002) peak broadening in the ZnO layer.

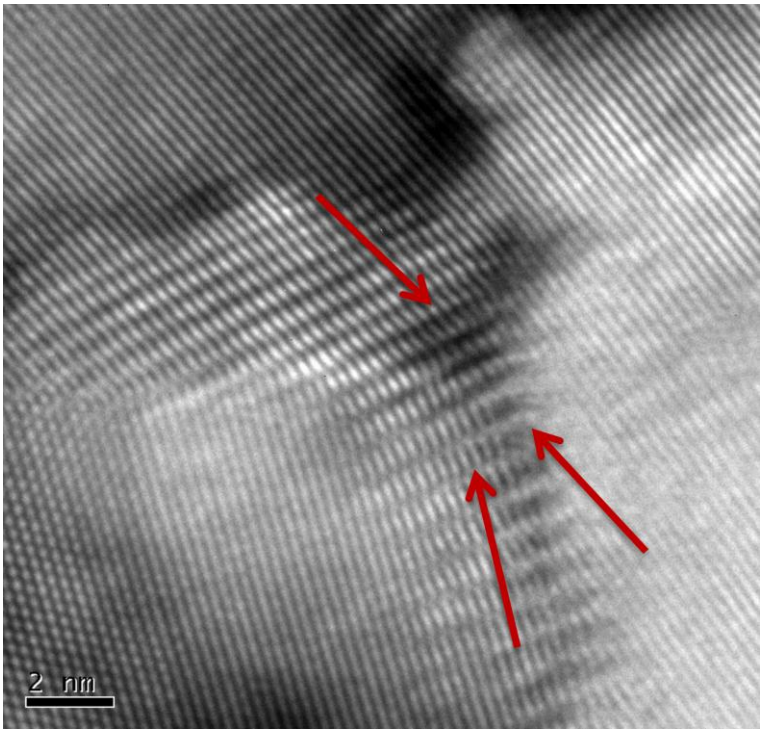

Figure 4.25: XTEM micrograph of worn 400°C annealed one trilayer film showing ZnO low angle grain boundary defects present in the ZnO layer.

4.5.3 1000°C Annealed One Trilayer

In Figure 4.26, an XTEM image of the 1000°C annealed one trilayer nanolaminate inside wear track with 100 gram load is shown. It is observed that part of the cross-section is undeformed while the top part of the film has undergone some form of deformation. There is an intermixing of the layers near the top of the film with no difference between the ZnO, Al_2O_3, ZrO_2 and Si. It is also observed that part of the ZrO_2 layer has also deformed with its particles present in the intermixed layer. The undeformed part of the film includes part of the ZrO_2 layer, the diffused ZnO, and the SiO_2 layers. This intermixing layer may have been caused by the applied stress from the pin ball where the stress causes the film underneath it to undergo this deformation. Recall that this

behavior (intermixing of layers) was not observed in both the as-deposited and the 400^{o}C annealed films.

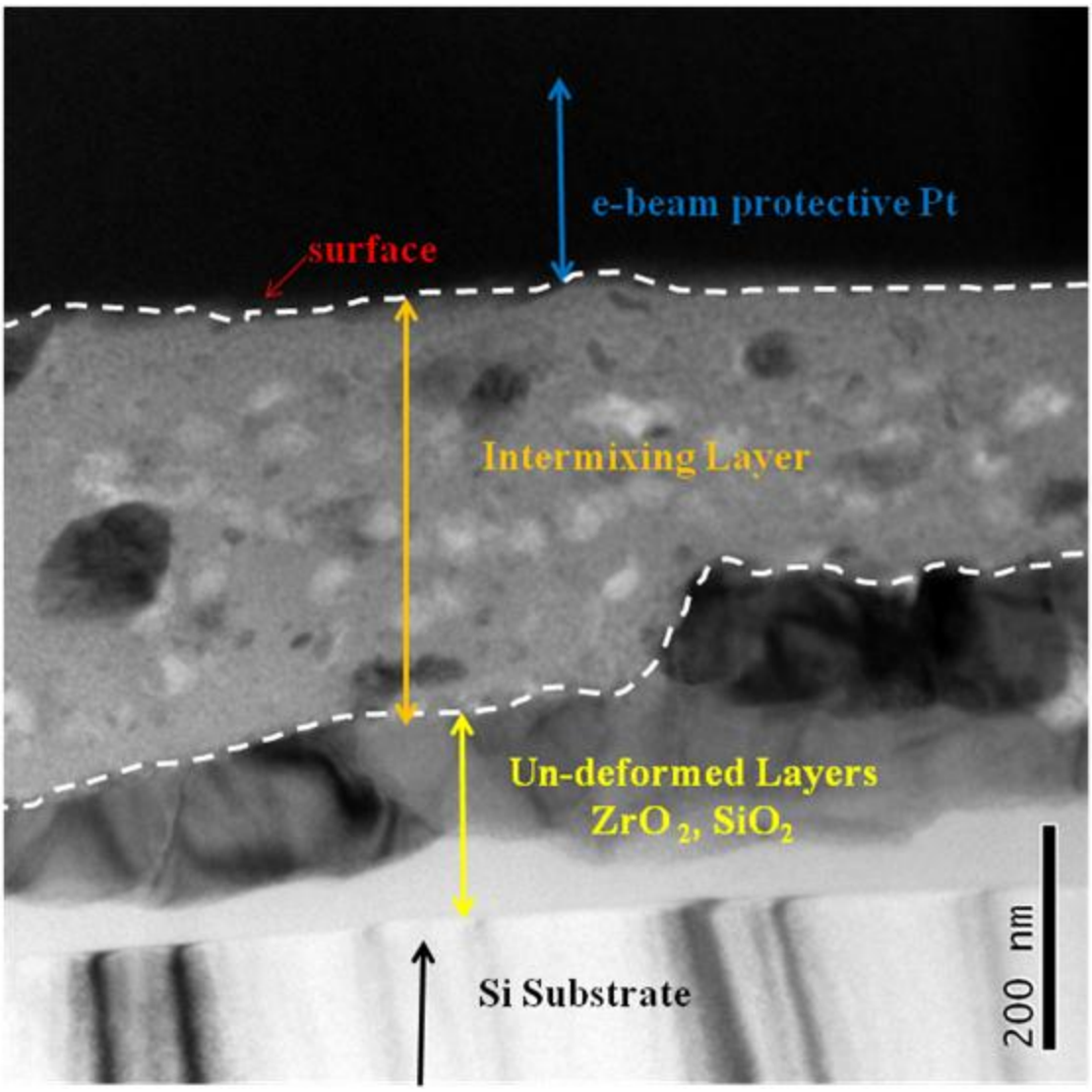

4.26: XTEM image of 1000^{o}C annealed worn one trilayer.

Figures 4.27 and 4.28 illustrate the chemical composition and mapping respectively of the wear track by EDS technique. In Figure 4.27, the line scan indicates the presence of ZrO_2 near the top of the film with ZnO underneath it. There is an

intermixing layer on top of the ZrO_2 which is a result of the applied stress. The counts on the intermixed layer is low and shows the presence of Si which is as a result of the Si_3N_4 ball that was used as the counter surface during the friction test. In the EDS compositional maps shown on Figure 4.28, the area under box one in the XTEM image was mapped out. The presence of Si is confirmed in this map as well. Thus during the friction test, there is a wearing of the pin ball, and the film is transferred into the wear track. This confirms that this coating is a very hard film. One other important observation that was made from Figure 4.28 is that there is very little ZnO near the top of the film. This suggests that all the ZnO film is worn out during the friction test and negates the possibility of using this trilayer as a solid lubricant at such a high temperature. Finally the intermixing of the diffused ZnO and the native SiO_2 is again observed in the compositional map.

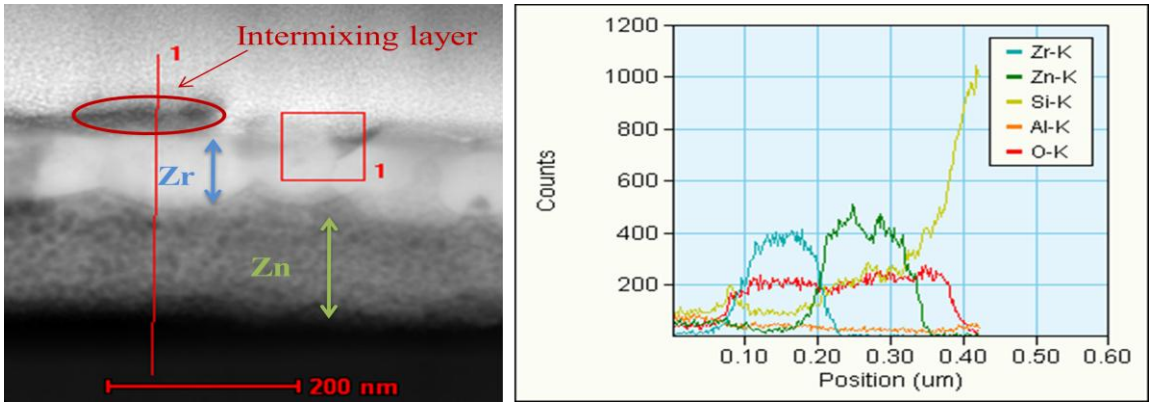

Figure 4.27: XTEM results of worn 1000°C annealed one trilayer nanolaminate film revealing the microstructure and layer composition.

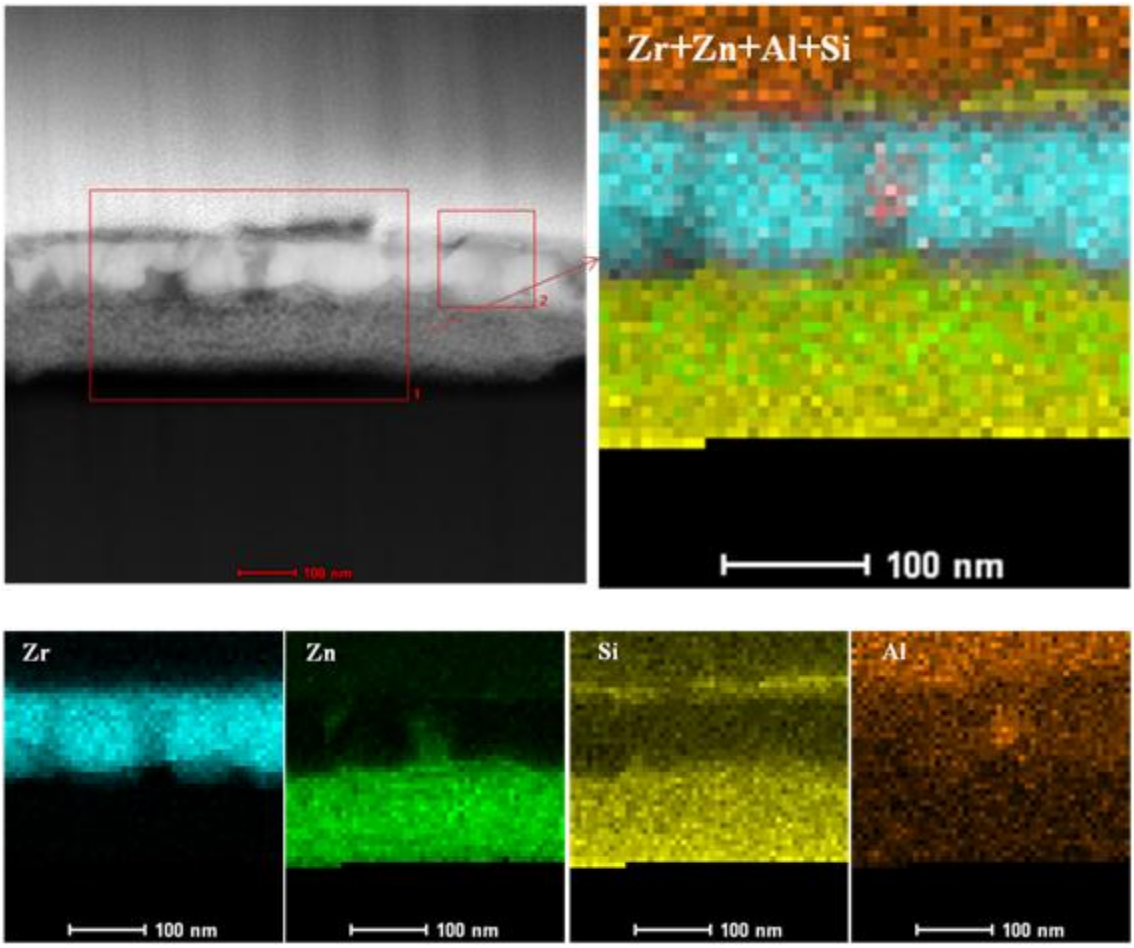

Figure 4.28: XTEM chemical analysis showing chemical maps of worn 1000^{o}C annealed one trilayer nanolaminate film.

4.6 ZnO/ZrO_2 nanolaminates

Other nanolaminates were also deposited by ALD in order to study their friction and wear behavior. ZnO/ZrO_2 two and eight bilayers were studied, and their results are summarized in this section. These systems were studied in order to determine if the absence of the Al_2O_3 layer would influence the tribological properties of the ZnO layer. Recall that the presence of Al_2O_3 beneath the ZnO layer enhances the texturing of the (0002) plane and thus reduces the friction.

4.6.1 Nanolaminate Films Microstructure

Figure 4.29 shows the XRD spectra (with incident angle = 5^{o}) of the ALD as deposited and annealed nanolaminates. The XRD data confirms that both 2 and 8 bilayers exhibited a hexagonal wurtzite crystal structure with strong (0002) diffraction peak for the ZnO film and a tetragonal crystal structure with (101) texturing for the ZrO_2 film. The (0002) texture, otherwise called c-axis orientation, is commonly observed in ZnO films because the c-plane perpendicular to the substrate normal is the most densely packed and thermodynamically preferred in the wurtzite structure.

Figure 4.29a shows the XRD data for the two bilayer nanolaminates while Figure 4.29b also shows the XRD data for the eight bilayer nanolaminates. In comparing the two plots, it is observed that in both cases, the peak intensity of the as-deposited nanolaminates is smaller than that of the 400^{o}C two hours annealed nanolaminate film. This suggests that annealing enhances crystallinity as observed in Section 4.1.3. It is again observed that the (0002) ZnO peak of the two bilayer nanolaminate film exhibits a strong intensity than the eight bilayer nanolaminate films.

Table 4.2: Grain sizes in nanometers of ZnO/ZrO_2 2 and 8 bilayers nanolaminate films.

Conditions	**As-deposited Grain Size (nm)**	**400^{o}C Annealed Grain Size (nm)**
2 Bilayers	23.1 ± 0.88	34.6 ± 0.55
8 Bilayers	12.7 ± 0.41	12.5 ± 0.34

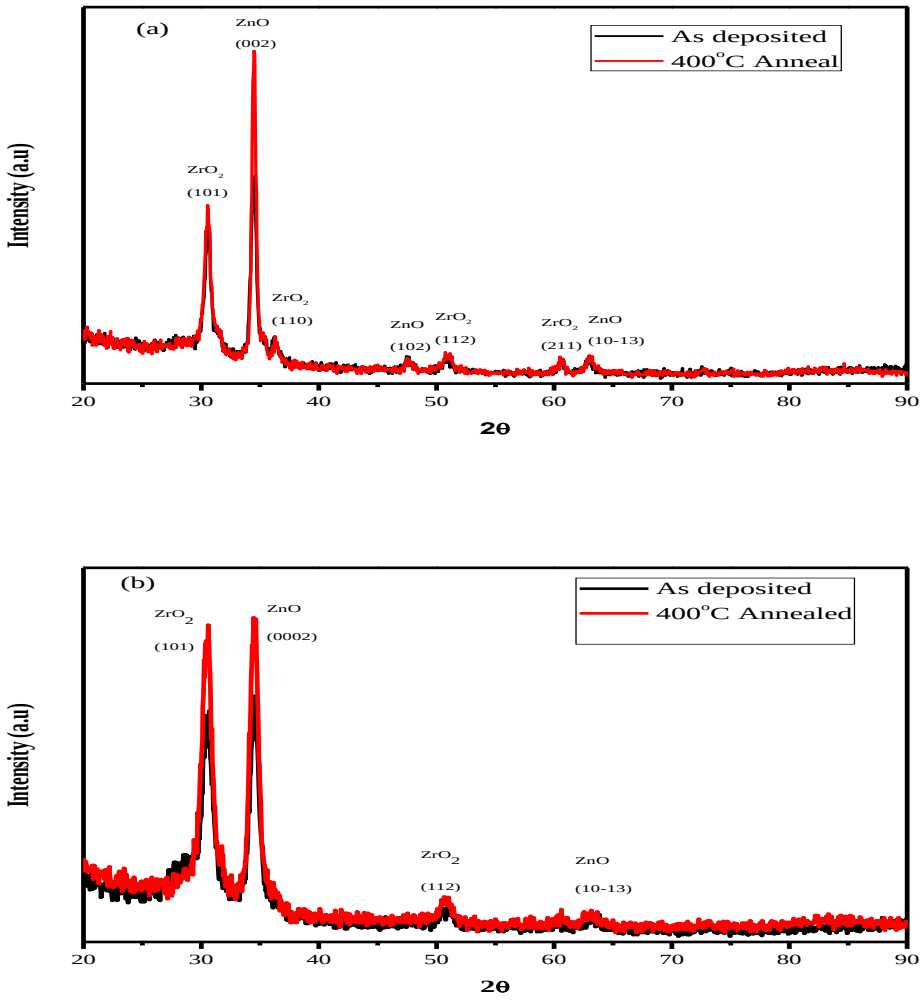

Figure 4.29: X-ray diffraction of (a) 2 bilayer ZnO/ZrO_2 and (b) 8 bilayer ZnO/ZrO_2 nanolaminate coating at room temperature and ex situ annealed 400°C for 2 hours.

The FWHM of the (0002) ZnO peaks is observed to widen with increase in the number of bilayers. This suggests, according to the Debye-Scherrer relationship, that the grain size decreased with increasing number of bilayers, this may be thickness related. Table 4.2 shows the grain sizes of the (0002) ZnO peak computed according to the Debye-Scherrer relationship for both 2 and 8 bilayers. The grain size for the 8-bilayer

nanolaminate indicates that, there is no grain growth due to the thermal annealing as observed in the other films. This could suggest that due to the stronger nature of the ZrO_2 layers, they are preventing any grain growth in the ZnO layers. It should also be noted that there is no phase transformation from tetragonal to monoclinic neither is there any ZnO (0002) or ZrO_2 (101) peak shift due to thermal annealing thus no lattice strain is observed in these nanolaminates.

4.6.2 Tribological Behavior

Figure 4.30 shows the tribological behavior of the 2 and 8 bilayer nanolaminate films. All the tests were done with 50 gram load SS440 C pin ball. It is observed that all the tests reached the 200 m distance without exceeding the 1.6 COF limit. According to Figure 4.30a (2 bilayer) friction plots, it is observed that the 400^{o}C annealed test has the lowest COF with a steady state friction of ~0.22. The as-deposited film test exhibited a lot of noise with a steady state friction of ~ 0.3.

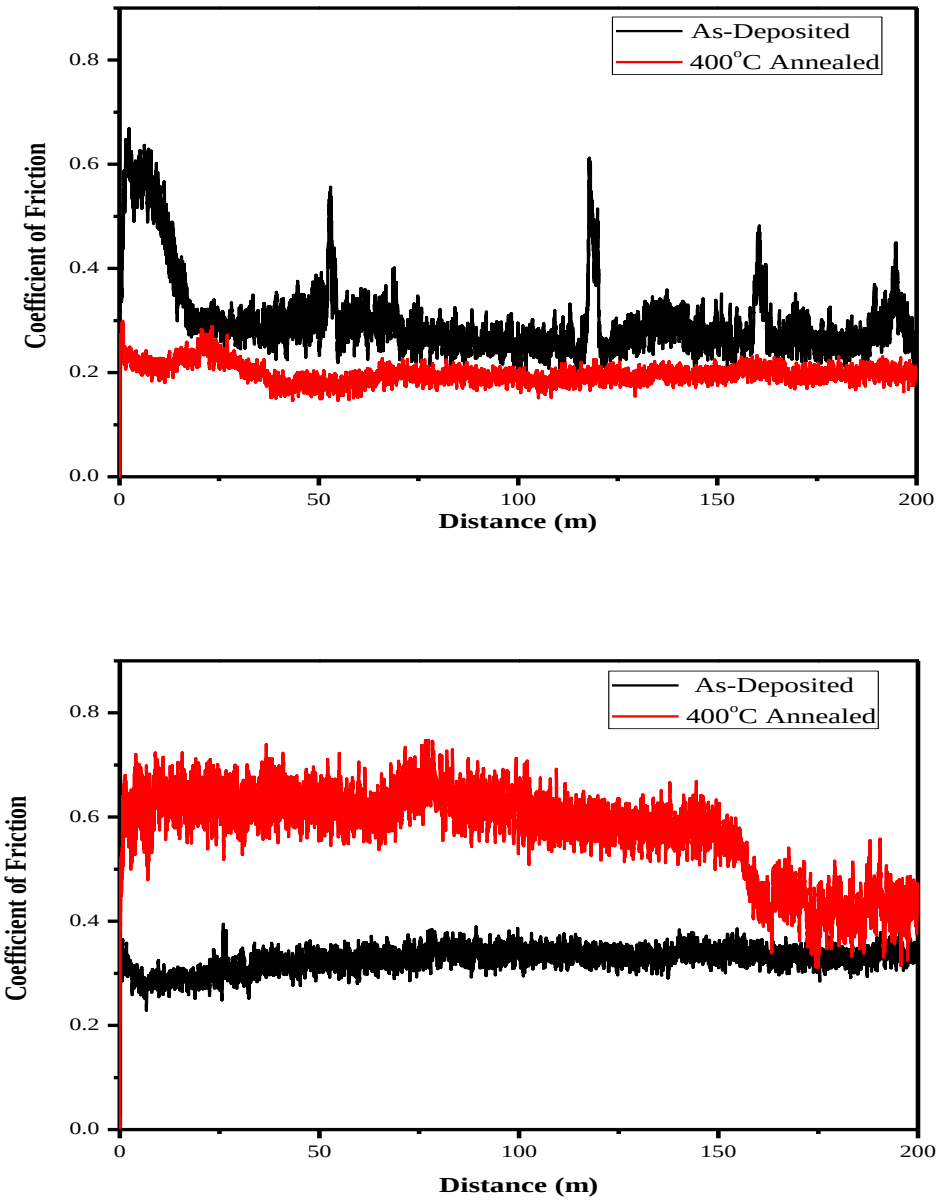

Figure 4.30: Coefficient of Friction measurements of (a) 2 bilayer ZnO/ZrO2 and (b) 8 bilayer ZnO/ZrO_2 nanolaminate coating at room temperature and ex situ annealed 400°C for 2 hours.

In Figure 4.30b, the as-deposited test show a steady state friction of ~0.3, and the 400°C annealed test showed a very high friction of ~0.6 which reduced to ~ 0.45 at the

later stage of the test, this test did not attain a steady state. It could be concluded that the 2 bilayer nanolaminate film exhibited better tribological behavior than the 8 bilayer nanolaminate film. Recall from the XRD results (Table 4.1) that the 8 bilayer nanolaminate films had smaller grain size than the 2 bilayer. Thus, it can be concluded that, the tribological behavior of the ZnO film is directly related to the (0002) grain size. There is a limitation to how low the grain size can be in order to obtain a very good wear behavior.

4.6.3 Cross-sectional TEM Behavior of Unworn/Worn 8 Bilayer Nanolaminate Film

In order to study the mechanisms that contributed to the friction behavior of these films, a cross sectional TEM was undertaken for the 8 bilayer as deposited nanolaminate film. Figure 4.31 shows a bright field cross-sectional TEM image of a ~140 nm thick ZnO/ZrO_2 8 bilayers nanolaminate coating on silicon substrate with its ~2 nm thick native SiO_2 layer. It is evident from this image that distinct and sharp interfaces exist between the crystalline ZnO (~10 nm thick) and ZrO_2 layers (7 nm thick). Both layers exhibited nanocolumnar grains growing to layer thickness. This is confirmed by the XRD data (4.29).

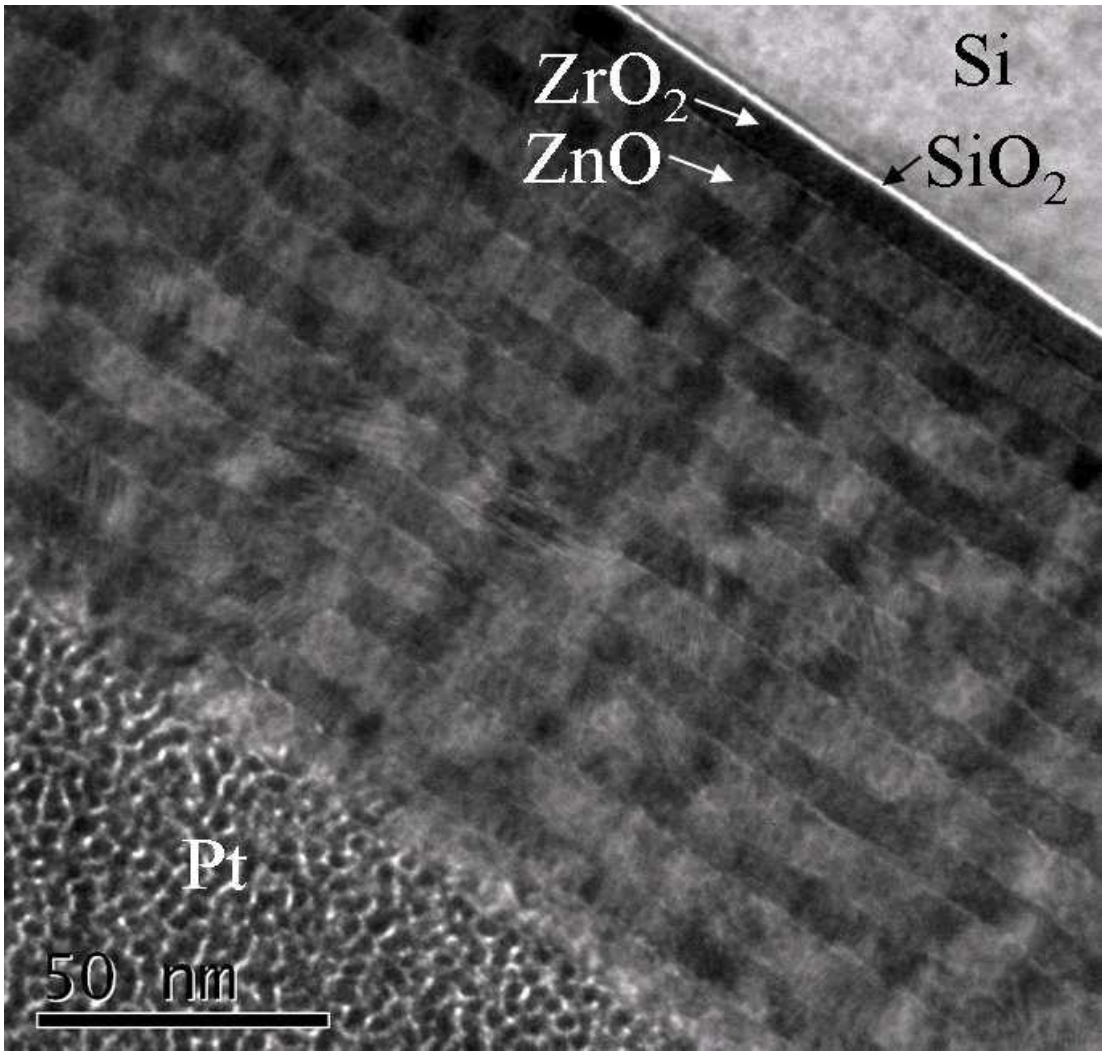

Figure 4.31: Cross-sectional TEM of unworn ZnO/ZrO_2 8 bilayer nanolaminate coating. Platinum was deposited to protect the coating from cross-sectional milling.

Figure 4.32 shows the XTEM image of the worn 8 bilayers nanolaminate coating after the 200 m distance test. The image shows that only the top ZnO layer has experienced deformation among the 16 individual layers. Also shown is a non-uniform layer (up to ~10 nm thickness) just below the protective Pt layer. The arrow in the figure points to a region where this layer is absent and shows slight thinning (wear) of the ZnO

layer.

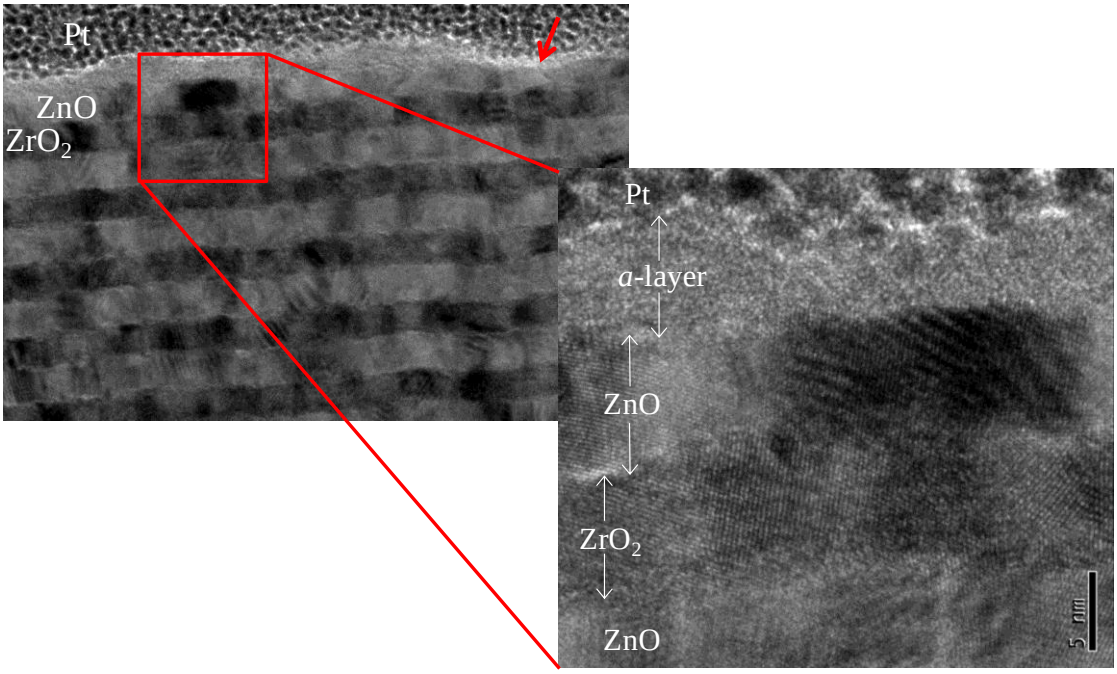

Figure 4.32: XTEM of worn ALD ZnO/ZrO_2 8 bilayer nanolaminate coating. Arrow points to worn ZnO. Insert shows a magnified area in the box.

The insert shows a magnified view of these top layers taken from the box located in the Figure 4.32. It is apparent that the non-uniform layer is amorphous which could either be from the native oxide, Fe_2O_3, on the SS440 C steel ball (adhesive wear) and/or this layer has undergone a stress-induced transformation from columnar structure to amorphous ZnO. There was no visible transfer film accumulated on the steel ball surface. Furthermore, no micro-cracks were observed among any of the layers even in the deformed top ZnO layer that suggests that the bilayers were effective in dissipating the energy required to initiate a crack.

It is also possible that the crystalline to amorphous stress-induced transformation

was accompanied by volume expansion due to less efficient atomic packing. The mixed amorphous-crystallite nature of this transformed layer makes it easy to accommodate interfacial shear. The plastic deformation process appears to be the continuous decrease in crystal size due to the applied cyclic stress until eventual amorphization. Hence, for this nanolaminate, the applied energy was being used to (a) transform the columnar grains to progressively small crystals and eventually to amorphous ZnO, and (b) in shearing the transformed ZnO layer across the surface to accommodate the sliding motion of the ball, i.e., the velocity accommodation mode is intrafilm shear.[27]

Unlike most solid lubricants, such as graphite, DLC, and WS_2, oxides are thermodynamically stable compounds with minimal grain coarsening, and should perform well over a wide range of environmental conditions such as thermal cycling as evident by the aforementioned 400^{o}C anneal. From all the results provided above, it can be concluded that the $ZnO/Al_2O_3/ZrO_2$ one trilayer nanolaminate film produced better COF data and understandable wear mechanism, hence, it was deposited on high speed M50 steels. The lubricous oxide nanolaminates will be demonstrated as good solid lubricants for thrust ball bearings and high vacuum rolling contact fatigue testing in the next chapter.

4.7 Chapter Summary

$ZnO/Al_2O_3/ZrO_2$ trilayer and ZnO/ZrO_2 bilayers nanolaminate films were deposited on Si substrate by Atomic Layer Deposition, the nanolaminate films were ex situ annealed at 400^{o}C and 1000^{o}C for 2 hours. The following observations were subsequently made after characterization and testing:

a. The surface roughness increased with increase in annealing temperature. This was later confirmed by XRD that the increase in roughness is due to increase in grain size according to the Debye-Scherrer formula.

b. XPS was able to determine the Zn:O composition ratio for the as-deposited and annealed films. It was observed that the as deposited film has a higher Zn composition than the 400^{o}C annealed film. Thus after anneal, the ZnO became closer to stoichiometry indicating that there is some surface oxidation after anneal. After 1000^{o}C anneal, analysis showed the presence of both Zn and Al on the surface (confirmed by AES mapping) which indicates that there is either diffusion of Zn into the other layers or evaporation of Zn from the surface. XPS depth profiling and XTEM analysis confirmed Zn diffusion had taken place.

c. The grown ZnO and ZrO_2 layers are nanocrystalline while the Al_2O_3 layers are amorphous. XRD and AFM analysis showed that annealing the films resulted in increases in the grain size of the ZnO film and not so for the ZrO_2 films. This change was related to an increase in the intensity and narrowing of the (0002) ZnO and (101) ZrO_2 peaks after thermal anneal, thus, the increase in grain size according to the Debye-Scherrer formula.

d. At 1000^{o}C of thermal anneal, XRD also demonstrated that there was a phase transformation in the ZrO_2 film. The film transformed from tetragonal to monoclinic ZrO_2. The phase transformation from tetragonal to monoclinic was attributed to the grain size of ZrO_2 crystallites. Crystalline ZrO_2 with grain sizes of 50 or less nanometers have been known to undergo this transformation at

temperatures close to 1000^{o}C.

e. XTEM analysis of the unworn films indicated very distinct and sharp interfaces between the layers. This is one of the advantages of ALD technique. It also confirmed the crystallinity of ZnO and ZrO_2 layers and the amorphization of the Al_2O_3 layers. After 1000^{o}C anneal, the XTEM image confirmed the diffusion of ZnO through the Al_2O_3 and the ZrO_2 layers. The native SiO_2 with thickness of ~2 nm was shown to have increased to ~40 nm, this resulted from the diffusion of oxygen through the nanolaminate stack. The phase transformation of the ZrO_2 that was observed by the XRD analysis was also confirmed in the TEM image and thus an increase in thickness of this layer was also observed.

f. Tribotests on the as-deposited and annealed one trilayers showed that the in the in the tests that Si3N4 ball was used, the 400oC annealed tests exhibited lower friction compared to the as-deposited films. Increase in applied load also exhibited a reduction in the steady state COF which is in agreement with the Bowden and Tabor model. Both of the as-deposited and 400^{o}C annealed films exhibited better COF and wear factor values than the 1000^{o}C annealed film. The 1000^{o}C annealed samples produced COF of ~ 0.45, and this poor friction behavior was partly attributed to the increase in the grain size of the (0002) ZnO film, the ZrO_2 phase transformation, diffusion of the ZnO through the other layers and the intermixing of the ZnO and Al_2O_3 layers. Thus the trilayer nanolaminate film is a good solid lubricant at room temperature and moderate temperatures, but may not have good properties to be used at very high temperatures (1000^{o}C).

g. AES mapping inside the wear track indicated the presence of film worn from the pin ball inside the wear tracks. As-deposited and 400^{o}C annealed films showed only ZnO and film from the pin ball inside the wear track. The 1000^{o}C annealed film showed the presence of ZnO, Al_2O_3, ZrO_2 and film from the Si_3N_4 ball inside the wear track. This confirmed that, the thin ZnO layer did not wear out in the case of the as-deposited and 400^{o}C annealed films, this was confirmed by XTEM analysis. For the 1000^{o}C annealed film, AES mapping confirmed that the unworn surface had both ZnO and Al_2O_3 present, mapping inside the wear track indicated that there is a mixture of all the layers inside the wear track and may cause abrasive wear which contributed to the high COF that was observed.

h. XTEM analysis of the worn surface showed grain re-orientation and bending of the ZnO grains near the top of the layer. This indicates that there is some form of plastic deformation occurring in the ZnO layer during sliding. The top of the ZnO film also shows a transformed ZnO layer from columnar to mix-amorphous-crystallite layer which makes it easy for the film to accommodate interfacial shearing hence low friction. Interfacial sliding with this friction induced surface layer aids in shear accommodation and prevents brittle fracture. The microstructure of the ZnO layer is dominated by stacking faults that are bordered by partial dislocations (PD). These basal stacking faults resulted from the incoherent boundaries between adjacent columnar grains or condensation of vacancies or interstitials. Because of the low surface energy of the (0002) ZnO basal planes, they have low stacking fault energies (SFE) compared to other

planes such as prismatic and the pyramidal planes thus stacking faults are easier to form on the (0002) basal planes than any of the planes. For the 1000^{o}C annealed wear tracks, there was an intermixing of the top layers due to the applied stress. EDS compositional mapping indicated the presence of Si on the top layer which confirms the wearing of the pin ball during the friction test. Finally, it was observed that there was no ZnO present near the top of the film, thus all the ZnO was worn out and the interfacial shearing that was observed in the previous films was not present in the 1000^{o}C annealed films. This concludes that, due to the hardness of this coating, it cannot act as a good solid lubricant.

i. In the ZnO/ZrO_2 bilayer nanolaminates, the XRD confirmed that both layers were crystalline and the as-deposited bilayers had smaller grain sizes than the 400^{o}C annealed samples. The 8 bilayers nanolaminate films comparatively had a smaller grain size compared to the 2 bilayers nanolaminate films. This was attributed to reduced thickness of the deposited layers, as thickness can influence grain growth. The 8 bilayers nanolaminate films grain size remained the same after 400^{o}C anneal, this resulted from the stronger nature of ZrO_2 layers that prevented any grain growth in the ZnO layer.

j. Tribotest indicated a low COF for the 2 bilayer nanolaminate films than the 8 bilayer nanolaminate films. This was observed for both as deposited and 400^{o}C annealed nanolaminate films. This resulted from the limitation of the thickness of the ZnO layer which influenced how large the (0002) grain sizes can grow.

k. XTEM unworn and worn images for the 8 bilayers nanolaminate films showed

that there were sharp interfaces between all the layers, and only the top ZnO film was worn during the tribotest. No microcracks were observed among any of the layers even in the deformed top ZnO layer, thus the bilayers were effective in dissipating the energy required to initiate any crack. There was some mixed amorphous-crystallite on the top ZnO layer which makes it easy to accommodate interfacial shear. Thus the applied energy was used to

i) Transform the columnar grains to progressively small crystals and eventually to amorphous ZnO

ii) In shearing the transformed ZnO layer across the surface to accommodate the sliding motion of the ball, i.e. the velocity accommodation mode is Intrafilm shear.

Thus ALD lubricious $ZnO/Al_2O_3/ZrO_2$ and ZnO/ZrO_2 nanolaminates are good candidates for providing low friction interfaces. In the next chapter, the $ZnO/Al_2O_3/ZrO_2$ one trilayer nanolaminate film will be deposited on high speed M50 steel coupons to demonstrate its lubrication properties in high vacuum rolling contact fatigue testing.

4.8 Chapter References

[1] Rainforth, W. M., J. Mater. Sci. 39 (2004) 6705-6721

[2] Suh, S., Miinea, L. A., Hoffman, D. M., Zhang, Z. and Chu, W. –K., Journal of Materials Science Letters 20 (2001) 115-118

[3] Gao, P.X., and Wang, Z.L., J. Appl. Physics 97 (2005) 044304

[4] Li, W.J., Shi. E.W., Zhong, W.Z., and Yin, Z.W., J. Cryst. Growth 203 (1999) 186

[5] Park, S.K., Lee, Y.E., Journal of Material Science 39 (2004) 2195-2197

[6] Claeyssens, F., Feeman, C.L., Allan, N.L., Sun, Y., Ashfold, M.N.R., Harding, J.H., J. matter. Chem. 15 (2005) 139-148

[7] Zabinski, J.S., Sanders, J.H., Nainaparampil, J., Prasad, S.V., Tribology Letters 8 (2000) 103-116

[8] Zhang, P.F., Liu, X.L., Wei, H.Y., Fan, H.B., Liang, Z.M., Jin, P., Yang, S.Y., Jiao, C.M., Zhu, Q.S., and Wang, Z.G., J. Phys. D: Appl. Phys. 40 (2007) 6010-6013.

[9] Kim, T.-S., Kim, H.S., Kim, T.-G., Jeong, H.G., Hong, S.-J., Journal of Alloys and Compounds 483 (2009) 593-596

[10] Romanes, M., PhD Dissertation, Uni. of N. Texas (2008)

[11] Zhu, J., and Liu, Z.G., Appl. Phys. A 78, (2004) 741-744

[12] Ji, Z., and Rigsbee, J.M., Journal of American Ceramic Society, 84 (12) (2001) 2841-2844

[13] Liu, W.-C., Wu, D., Li, A.-D., Ling, H.-Q., Tang, Y.-F., and Ming, N.-B., Applied Surface Science 191 (2002) 181-187

[14] Garvie, R.C., The Journal of Physical Chemistry 69 (4) (1965) 1238-1243

[15] Kao, A.S., and Gorman, G.L., Journal of Applied Physics 67 (8) (1990) 3826-3834

[16] Ginestra, C.N., Sreenivasan, R., Karthikeyan, A., Ramanathan, S., and McIntyre, P.C., Electrochemical and Solid State Letters, 10 (10) (2007) B161-B165

[17] Crammer, D.C., Journal of Material Science, 20 (1985) 2029-2037

[18] Rainforth, W.M., Journal of Material Science, 39 (2004) 6805-6721

[19] Singer, I.L., Macroscopic and Microscopic Processes. Dordrecht, Netherlands: Kluwer Academic; 1992, 237

[20] Scharf, T.W., and Singer, I.L., Tribology Transactions 45 (2002) 363-371

[21] Chen, M,-M., Lin, J., Wu, T,-W, and Castillo, G., Journal of Applied Physics 63 (8) (1988) 3275-3277

[22] Liu, H., Jiang, E.Y., Zheng, R.K., and Bai, H.L., Phys. Stat. Sol. (a) (201) 4 (2004) 739-744

[23] Tiwari, S., Prakash, R., Choudhary, R.J., and Phase, D.M., Journal of Applied Physics D 40 (2007) 4943-4947

[24] Gao, Q., Chen, F., Zhang, J., Hong, G., Ni, J., Wei, X., and Wang, D., Journal of Magnetism and Magnetic Materials 321 (2009) 1052-1057

[25] Pan, L., Zhang, G., Fan, C., Qiu, H., Wu, P., Wang, F., and Zhang, Y., Thin Solid Films 473 (2005) 63-67

[26] Yan, Y., Dalpian, G.M., Al-Jassim, M.M., and Wei, S.-H., Physical Review B 70 (2004) 193-206

[27] Doll, G.L., Mensah, B.A., Mohseni, H, and Scharf, T.W., Journal of Thermal Spray Technology, 19 (1-2) (2010) 510-516

[28] van Hassel, B.A., and Burggraaf, A.J., Applied Physics A 52 (1991) 410-417

CHAPTER 5

LUBRICIOUS ATOMIC LAYER DEPOSITED NANOCRYSTALLINE $ZnO/Al_2O_3/ZrO_2/Al_2O_3$ NANOLAMINATES ON M50 STEEL SUBSTRATES, RODS AND CUPS

5.1 Introduction

M50 steel a derivative of high speed steels (HSS) is very useful in high-temperature mechanical applications such as in thrust ball bearings of aircrafts and high-temperature vacuum rolling contacts. The major alloy elements consist of Mo, Cr and V with dispersed impurities such as Si, C, Mn and Ni.[1] Due to the extreme operational conditions for these bearing elements such as high rotational speeds and high temperatures, a good lubrication mechanism is required to further improve the friction and wear during the steel to steel contacts.[2]

Lubrication at high temperatures (300-1000^{o}C) presents a lot of challenges for the tribology community.[3] Liquid lubricants have been used but at elevated temperatures, these conventional liquid lubricants have a marked effect on bearing life and load carrying capacity, and they are also not capable in operating effectively in the hostile bearing environments. This is because at the extreme environmental conditions, conventional liquids lose their lubricious behavior and thermally degrade. The most common lattice-layered solid lubricants like graphite and molybdenum disulfide also oxidize quickly and degrade above ~ 350^{o}C. On the other hand, non-layered solid lubricants such as inorganic fluorides (CaF_2, BaF_2) and metal oxides (PbO, TiO, NiO) can

operate at high temperatures due to their low shear strength, high ductility and because they are chemically stable in the presence of air.[4] However, all these materials have their disadvantages and may not correspond to the ideal lubricant which can operate at room temperature as well as elevated temperatures both in air and in vacuum.

For this study, a solid lubricant nanolaminate film consisting of $ZnO/Al_2O_3/ZrO_2/Al_2O_3$ deposited on M50 substrates by ALD technique is investigated. The premise of this nanolaminate film is that a solid lubricant layer will function as a break-in (conditioning) layer for a CrN-M50 steel rolling interface where the CrN would otherwise abrade (damage) the uncoated steel raceways. The lubricous, nanocrystalline ZnO layer was structurally-engineered to achieve low surface energy (0002)-oriented grains, this provided low sliding friction coefficient. The amorphous Al_2O_3 layer contributed to achieve this preferred orientation while the crystalline ZrO_2 structure acted as a high toughness/load bearing layer. The final layer which is another Al_2O_3 served as an adhesion layer between the M50 steel and the ZrO_2 layer.

5.2 Microstructure of the Nanolaminate Film

Following the ALD deposition of the $ZnO/Al_2O_3/ZrO_2/Al_2O_3$ nanolaminate film, XRD analysis was performed to investigate the crystal structure of both the as-deposited and the 400^{o}C 2 hours post deposition annealed film and this is shown in Figure 5.1. The XRD pattern shows the presence of ZnO, ZrO_2 and the M50 steel substrate. This confirms that the ZnO and the ZrO_2 thin films are both crystalline while the Al_2O_3 film is amorphous as determined in the previous chapter. It was also found that the (0002) diffraction peak is the highly orientated ZnO peak. This confirms that the hexagonal close

packed (wurtzite crystal structure) ZnO structure film is orientated on the *c*-axis and the ZrO_2 columnar grains are tetragonal (derivative of fluorite crystal structure). It is also seen that the diffraction peak (0002) of the annealed film also becomes highly intense thus the crystal quality is improved as observed in chapter 4. Once again the FWHM of the 400^{o}C annealed sample became slightly narrower compared to the as-deposited film implying that there is a small increase in grain size.

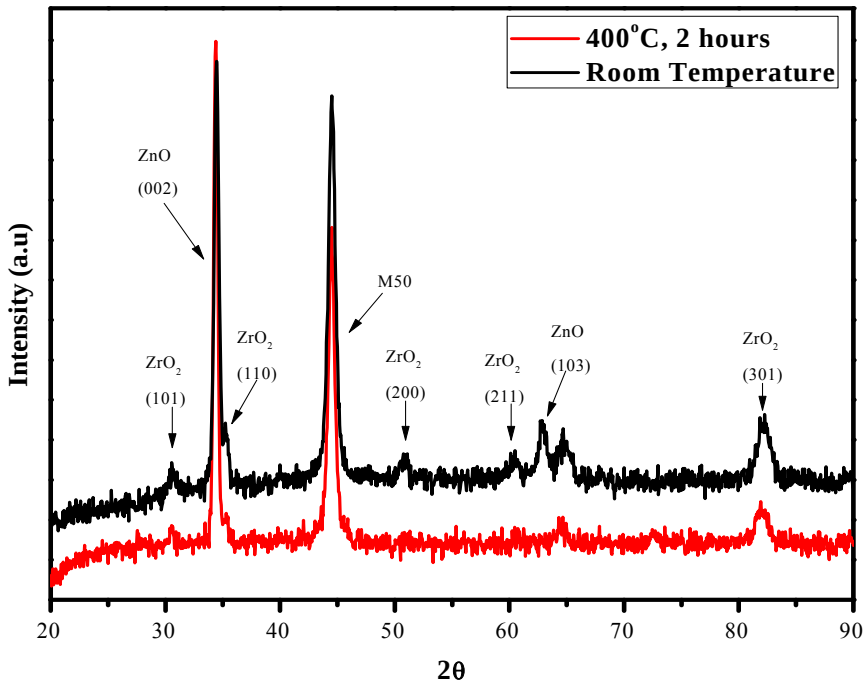

Figure 5.1: XRD measurements of ALD deposited ZnO/Al_2O_3/ZrO_2/Al_2O_3 nanolaminate film on M50 steel substrate before and after anneal.

The FWHM of the ZnO (0002) peak indicated that there is broadening of the peak in both films. Similar to the previous chapter, it is observed that the as-deposited nanolaminates had a FWHM greater than that of the 400^{o}C annealed film, thus the grain

size of the 400°C annealed film is larger than the as-deposited film. It should be noted that the (0002) diffraction peak for the thin films was not shifted with the 400°C anneal, thus there is no residual stress at the interphase of the ZnO film and the Al_2O_3 film.[5]

5.3 Cross-sectional Analysis of the Nanolaminate Film

Figure 5.2 shows an XTEM bright field image of approximately 300 nm thick $ZnO/Al_2O_3/ZrO_2/Al_2O_3$ nanolaminate grown on M50 steel. As observed in the previous chapter, there is a sharp interface between all the layers. There is no decohesion between the M50 steel substrate and the Al_2O_3 adhesion layer, thus, the Al_2O_3 is bonded very well with the substrate. As observed by the XRD analysis, both of the Al_2O_3 layer are seen to be amorphous while the ZnO and the ZrO_2 are crystalline and form columnar grains through to the top of the film.

Recall that the ZnO (0002) peak broadening (FWHM $\geq 0.3^o$)[6] is linked to growth defects (lattice imperfections), in Figure 5.3, a magnified XTEM image of the ZnO layer shows the presence of defect(s) in the as-deposited film. The defects (represented by white arrows) are determined to be stacking faults. It was determined that the density of the basal stacking faults (BSF) in the ZnO films is fairly high. These stacking faults are easily recognizable due to the changes in the stacking sequence of the (0001) planes, and, according to Gerthsen et al.[7], stacking faults may originate from the precipitation and condensation of Zn interstitials or O vacancies so that a missing or extra (0002) plane will be introduced into the lattice. Compared to the other planes, the (0002) basal plane are low surface energy planes and thus have low stacking fault energy. For example, the SFE of the ZnO {0002} plane was computed by a Vienna Ab-initio Simulation Package

(VASP) to be ~ 24 mJ/m^2 while that for {10-10} prismatic plane was also determined to be ~ 427 mJ/m^2. Thus the energy required to create stacking faults on a prismatic plane is approximately twenty times higher than that of a basal plane, this makes it very difficult for stacking faults to form on prismatic planes than on basal planes of ZnO crystal structure. The type of stacking faults that are formed in the {0002} basal planes are type I intrinsic, which is ABAB|CBCB.

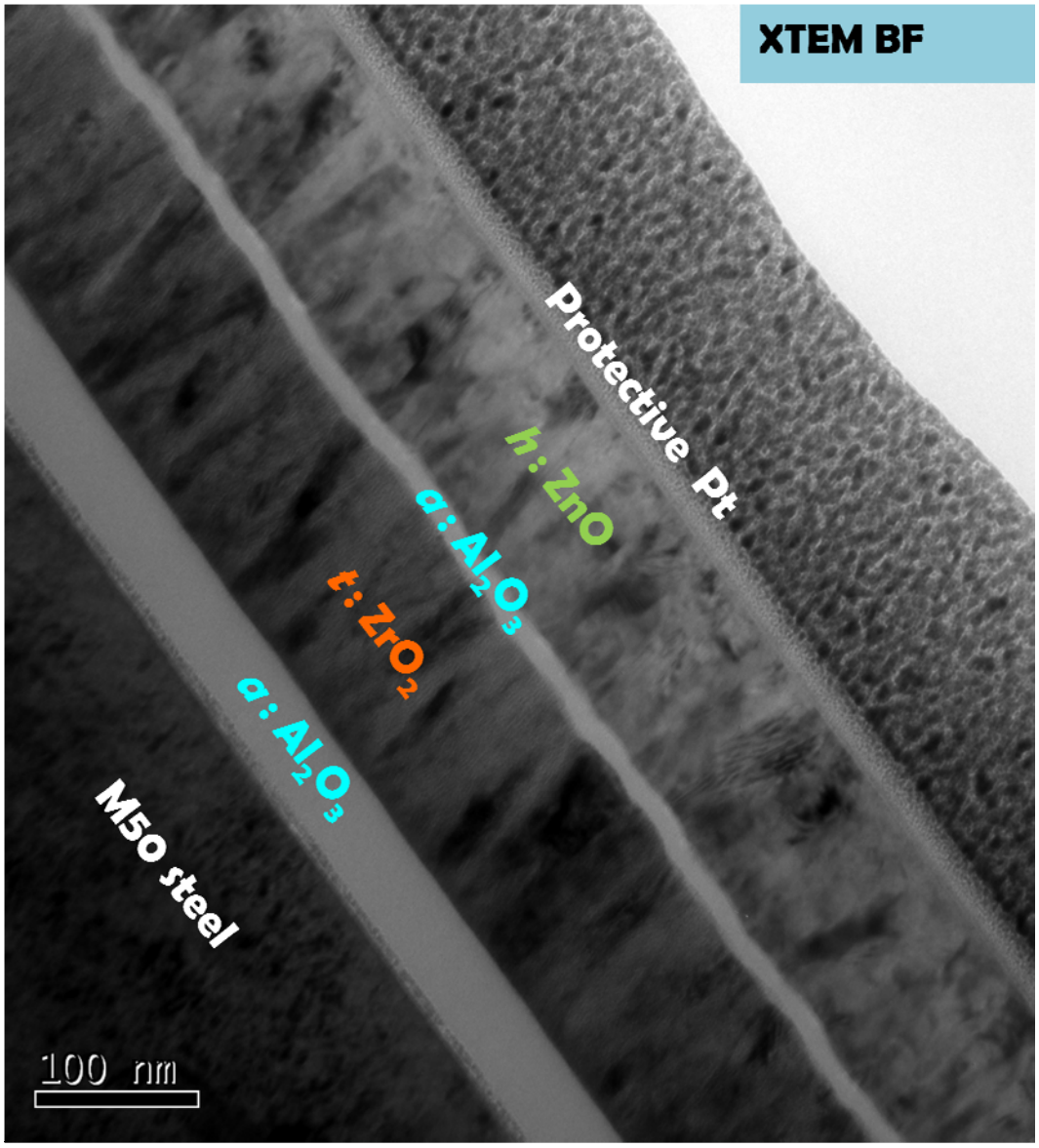

Figure 5.2: XTEM bright field image of unworn $ZnO/Al_2O_3/ZrO_2/Al_2O_3$ nanolaminate film grown on M50 steel.

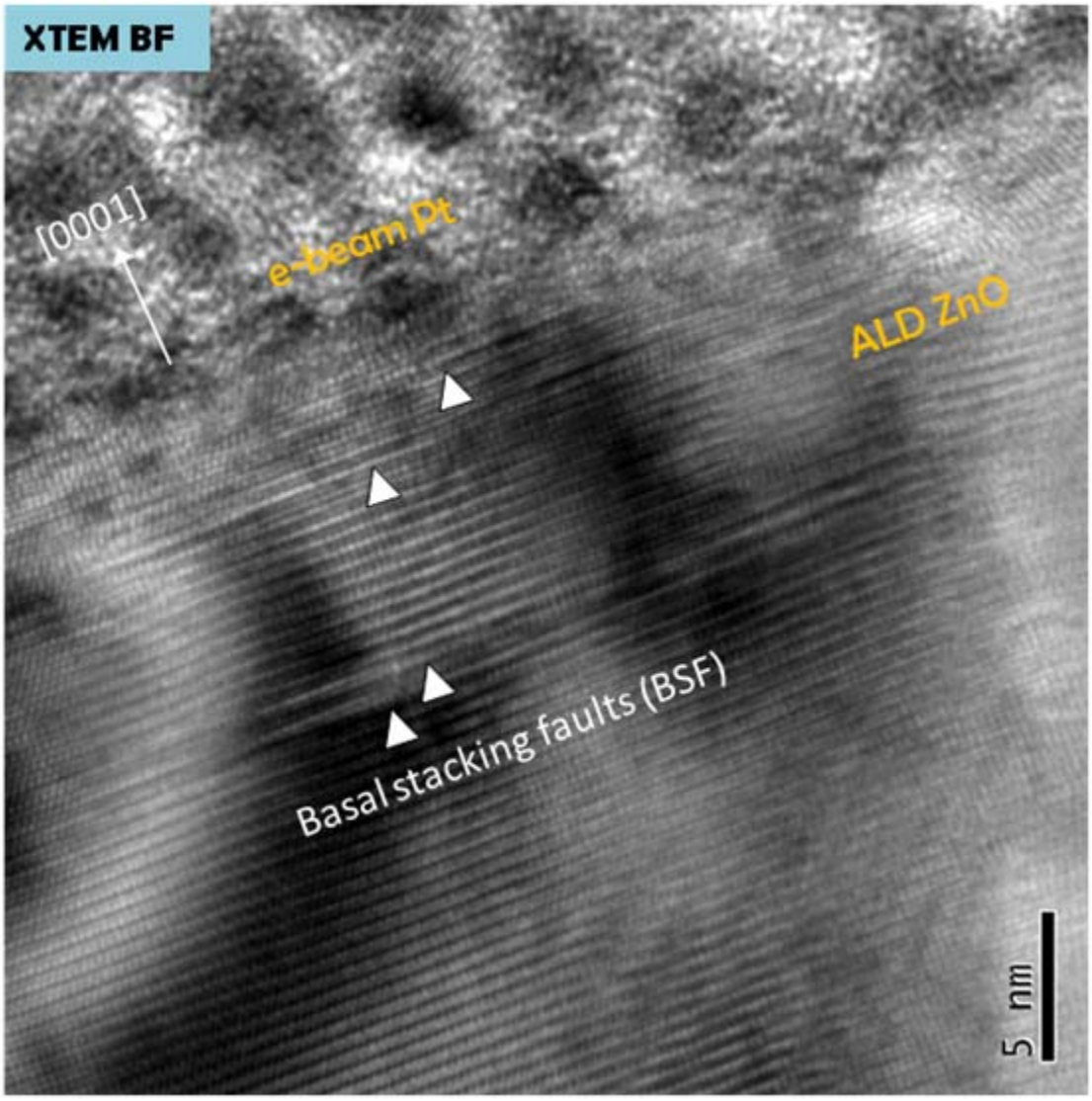

Figure 5.3: Magnified XTEM image showing the interface between the ZnO layer and the Pt layer of the unworn ZnO/Al_2O_3/ZrO_2/Al_2O_3. There is the presence of basal stacking faults (white arrows) along the [0001] growth direction.

Other groups have attributed the high stacking fault density in their ZnO layers to other reasons. For example, Sun et al.[8], related the high density stacking faults in their ZnO to their deposition conditions. According to Sun's group ZnO films grown by island nucleation with lateral extension on a substrate surface will produce a film with a

columnar structure and incoherent grain boundaries with stacking faults originating from these incoherent boundaries between adjacent columnar grains during the growth. In this study, the high stacking fault density is attributed to the low stacking fault energy on the {0002} planes and the broadening of the (0002) peak.

5.4 Tribological Behavior of the Nanolaminate Film

The plots in Figure 5.4 shows the sliding coefficient of friction (COF), μ as a function of unidirectional sliding distance for the as-deposited and 400^{o}C annealed nanolaminate. A Si_3N_4 ball (R = 1.6 mm) was used at room temperature of ~ 40% RH. All tests went to completion of 200 m total distance without reaching 1.6 the COF limit set for the tribometer. For the as-deposited (top figure) nanolaminate film, the steady state friction coefficients were approximately 0.342, 0.282, 0.248 and 0.16 for the 25, 50, 100 and 250 gram loads respectively. All the loads maintained steady state friction from the start to finish of the tribotest except the 100 gram load test. This test exhibited high COF (0.34) at the run in and reduced to its steady state after approximately 60 m sliding distance. For the 400^{o}C annealed nanolaminate film (Figure 5.4 bottom), the steady state friction varied from approximately 0.232, 0.177, 0.136 and 0.122 for the loads of 25 to 250 grams respectively. The 100 and 250 loads maintained their steady state friction for the entire test while the 25 and 50 gram loads started with low COF and rose steadily to their respective steady states.

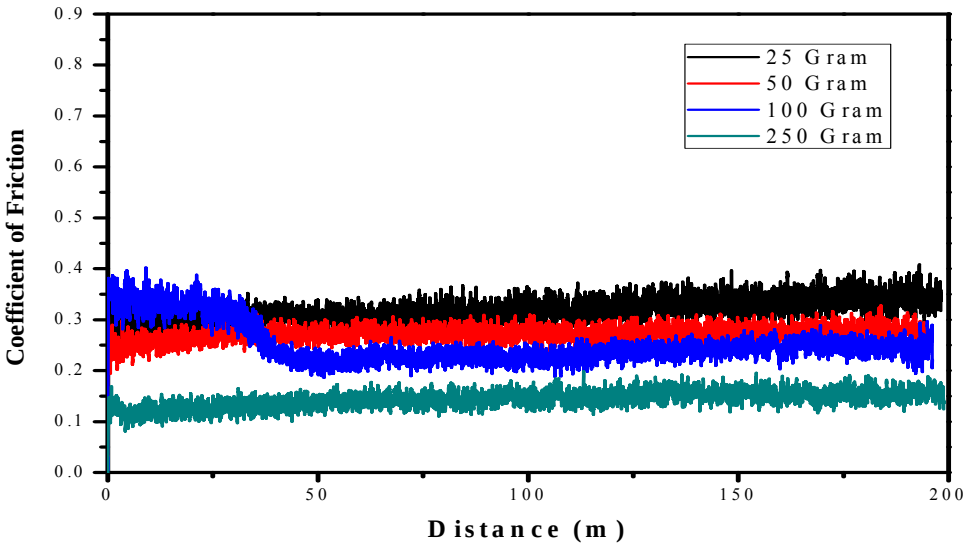

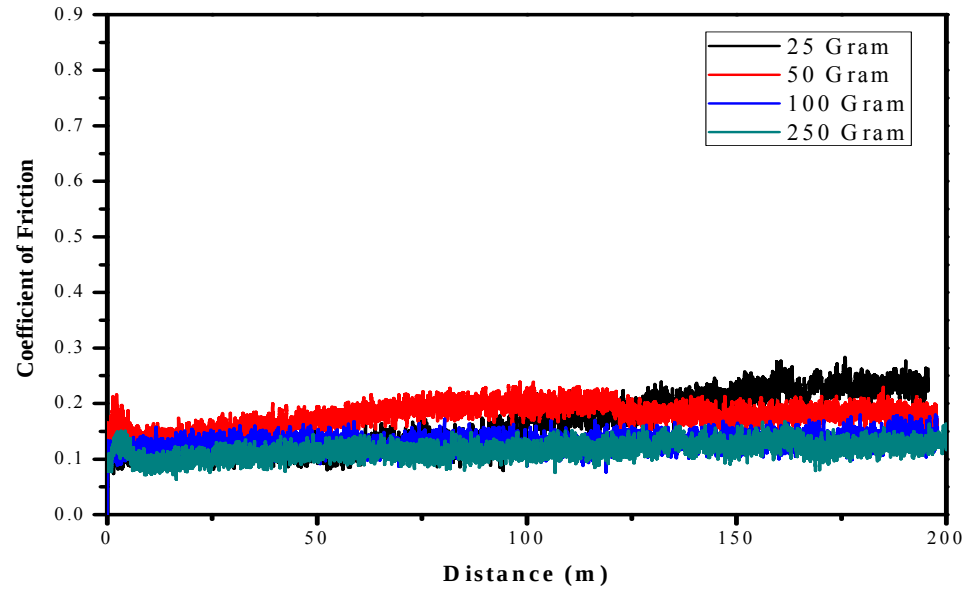

Figure 5.4: Coefficient of friction measurements of the $ZnO/Al_2O_3/ZrO_2/Al_2O_3$ nanolaminate films grown on M50 steel. (Top) as-deposited nanolaminate (bottom) 400^{o}C annealed nanolaminate film.

From Figure 5.4, it is evident that the steady state friction for the as deposited nanolaminate films were higher compared to the 400^{o}C annealed nanolaminate films. Figure 5.5 shows a linear regression for steady state friction coefficient (μ_{ss}) versus the inverse mean hertzian pressure for both as-deposited and 400^{o}C annealed nanolaminate films. The plot shows that the steady state friction decreases as the applied normal load increases in both as-deposited and 400^{o}C annealed films. This trend is in good agreement with the Hertzian contact model ($L^{-1/3}$) as proposed by Bowden and Tabor (equation 3.10). This trend was also observed in chapter 4. The Hertzian contact model showed that, $\mu = L^{-0.32}$ for the as-deposited and $\mu = L^{-0.28}$ for the 400^{o}C annealed films. These values are all in agreement with the friction coefficients, thus for low μ_{ss}, τ_o is expected to also decrease. The τ_o that was observed for the as-deposited and 400^{o}C annealed nanolaminate trilayers were 181 MPa and 107 MPa, respectively. Such interfacial shear strength has been observed for similar solid lubricants.

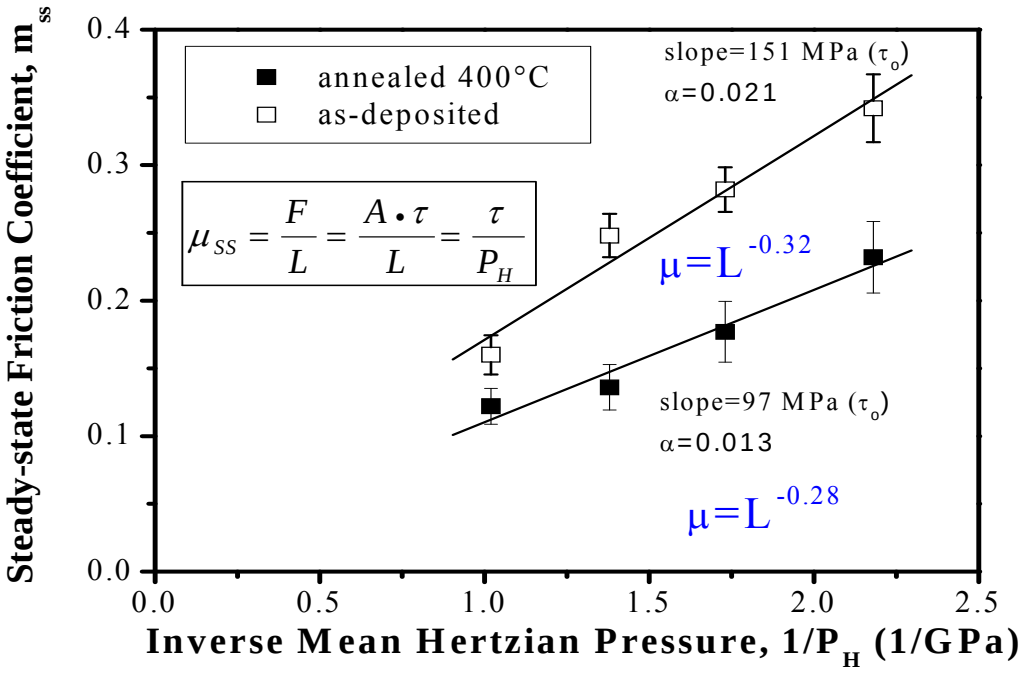

Figure 5.5: Linear regression fits for friction coefficient as a function of inverse Hertzian pressure for as-deposited and 400^{o}C nanolaminate films.

The low friction that is exhibited by this nanolaminate films could be assigned to the ZnO crystal structure (0002) textured plane. Thus the nanocrystalline grains are prone to reorientation during sliding contact, where they can realign to create new surfaces that are rich in defects. The textured (0002) ZnO film with nanocolumnar structure is able to deform plastically.[9] As already mentioned, the 400^{o}C annealed nanolaminates film comparatively has low friction coefficient, this is linked to the increase in the (0002) peak intensity as observed in the XRD plot.

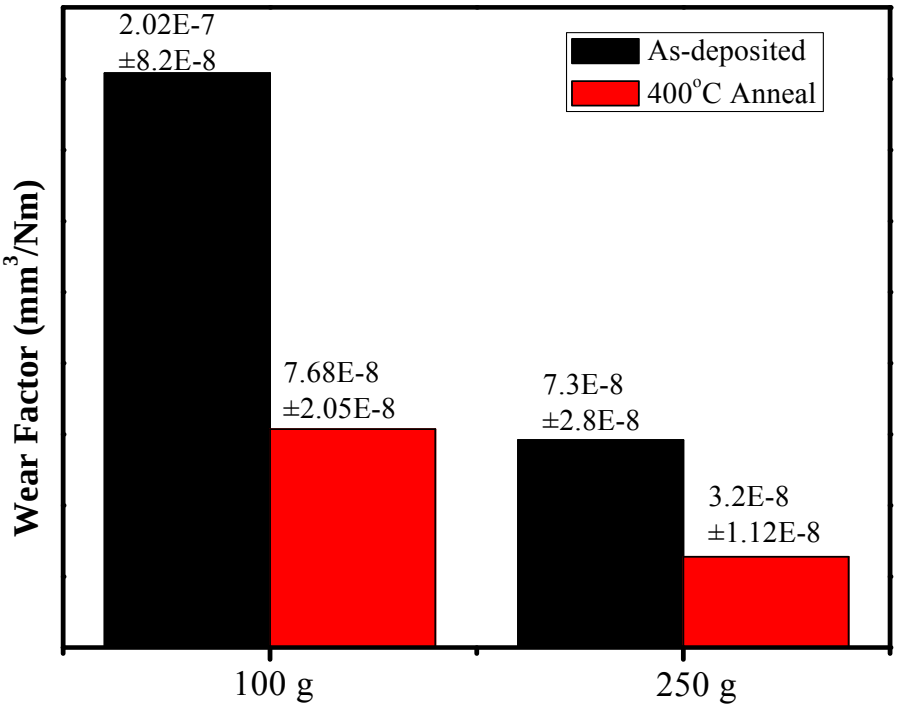

Figure 5.6: Calculated wear factors of the 100 and 250 gram loads for as deposited (black) and 400°C annealed nanolaminate films.

The wear factors calculated using surface profilometry traces is shown in Figure 5.6. It should be noted that only the 100 and 250 gram loads are presented in this study, as there were a lot of inconsistencies in the 25 and 50 gram load measurements. All the wear factor values were in the 10^{-7} to 10^{-8} mm^3/Nm range which is considered as the low wear regime as was the case in the previous chapter. Another observation was that, the 400°C annealed films exhibited slightly lower wear factors than the as-deposited film and this is in agreement with the friction coefficients. Thus it could be concluded that this

nanolaminate film exhibits very good wear behavior at both room and elevated temperatures.

5.5. Cross-sectional Behavior of Worn Nanolaminate Films

Figure 5.7 shows the cross-sectional micrograph of the worn $ZnO/Al_2O_3/ZrO_2/Al_2O_3$ nanolaminate film with 100 gram load. From the image it is observed that there is no evidence of any brittle fracture (cracking) in the ZnO film after 200 m of sliding distance. Thus the ZrO_2 layer which is acting as a load bearing layer is able to prevent crack through the nanolaminates. The amount of ZnO that was worn out after such a long run is very minimal, thus, very low wear is observed inside the wear track. It is also observed that there is some plastic deformation occurring in the ZnO nanocrystalline layer. The presence of plastic deformation is observed near the top portion of the ZnO layer with evidence of bending (area in blue box) of the nanocolumnar grains of the ZnO. In Figure 5.8, a magnified XTEM image of the area in the blue box in Figure 5.7 is shown. This (Figure 5.8) confirms the presence of basal stacking faults on the (0002) plane. The basal stacking fault density increases with sliding (multiple slip of partial dislocations by a dislocation glide mechanism). The plastic deformation occurring in the nanocrystalline ZnO layer contributes to the continuous decrease from crystalline to amorphous.

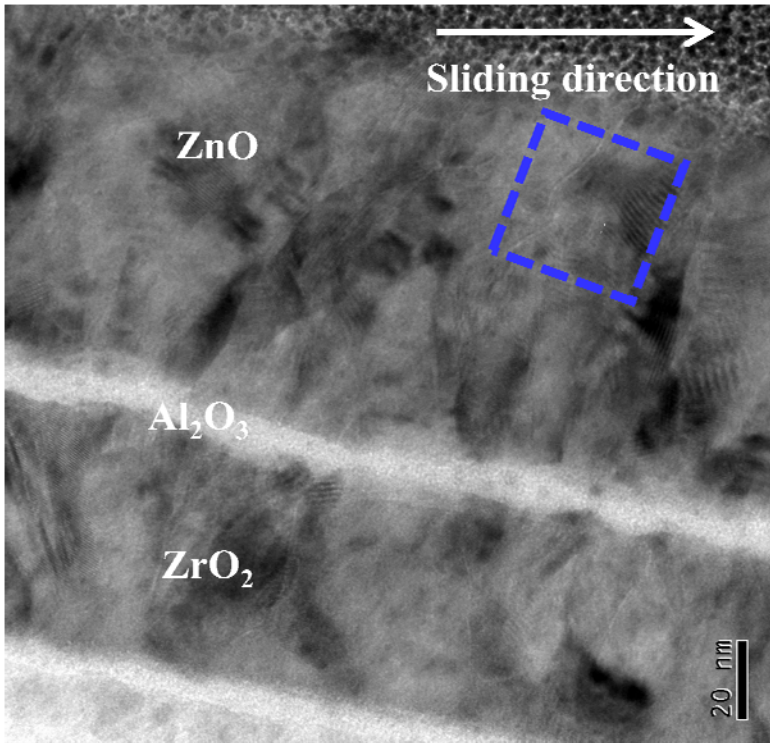

Figure 5.7: XTEM bright field image of a worn $ZnO/Al_2O_3/ZrO_2/Al_2O_3$ nanolaminate grown on M50 steel substrate.

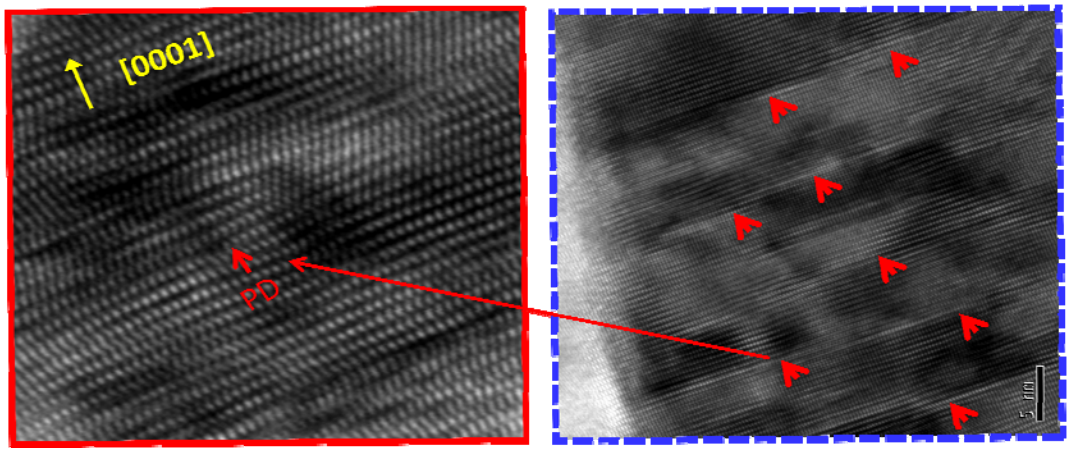

Figure 5.8: Magnified XTEM image of the ZnO layer showing the presence of stacking faults in the [0001] direction.

In order to determine if the dislocations observed are only occurring on the (0002) plane, a Fast Fourier Transform (FFT) diffraction pattern was undertaken. Figure 5.9a shows the XTEM image of the ZnO layer with the (0002) basal plane with its corresponding FFT diffraction pattern and the Fourier-filtered image. There are obviously observable dislocations present in the ZnO (0002) plane. The corresponding electron diffraction pattern (FFT image) of single columnar grain near the surface shows that the {0002} basal planes are streaked along the [2-1-10] beam direction, which is consistent with the presence of planar defects (stacking faults) running normal to the [2-1-10] direction. The identification of these dislocations is confirmed in the corresponding Fourier-filtered image using the {0002} diffractions spots, which demonstrate that each PD (shown by arrows) corresponds to one additional (0002) plane. The BSF density increases with sliding, there are multiple slip of PDs which occurs by a dislocation glide mechanism. In the Figure 5.9b, an XTEM image of the ZnO {01-10} prismatic plane with its corresponding FFT diffraction pattern and the inverse Fourier-filtered image are shown. It is observed from the XTEM image that there was no presence of any subsurface plastic deformation in the nanocolumnar grains after the frictional contact. The corresponding FFT diffraction pattern shows that the {01-10} prismatic planes are not streaked along [2-1-10] beam direction, which is consistent with the fact that there are no planer defects (stacking faults) running normal to the [2-1-10] direction. This is confirmed by the corresponding Fourier-filtered image using the {01-10} diffraction spots, which translates to no prismatic stacking faults in the worn subsurface (due to its high SFE). This is very important since there is only basal slip (no interacting slips

systems) which translates to low interfacial shear strength (friction). Thus as observed with the VASP computation of the SFE, Figure 5.9 confirms that planer defects could not be generate after applying stress on the prismatic plane due to the high SFE on this plane. Thus in order to enhance lubrication of ZnO film, it is very important that the ZnO crystal structure is dominated by the (0002) plane.

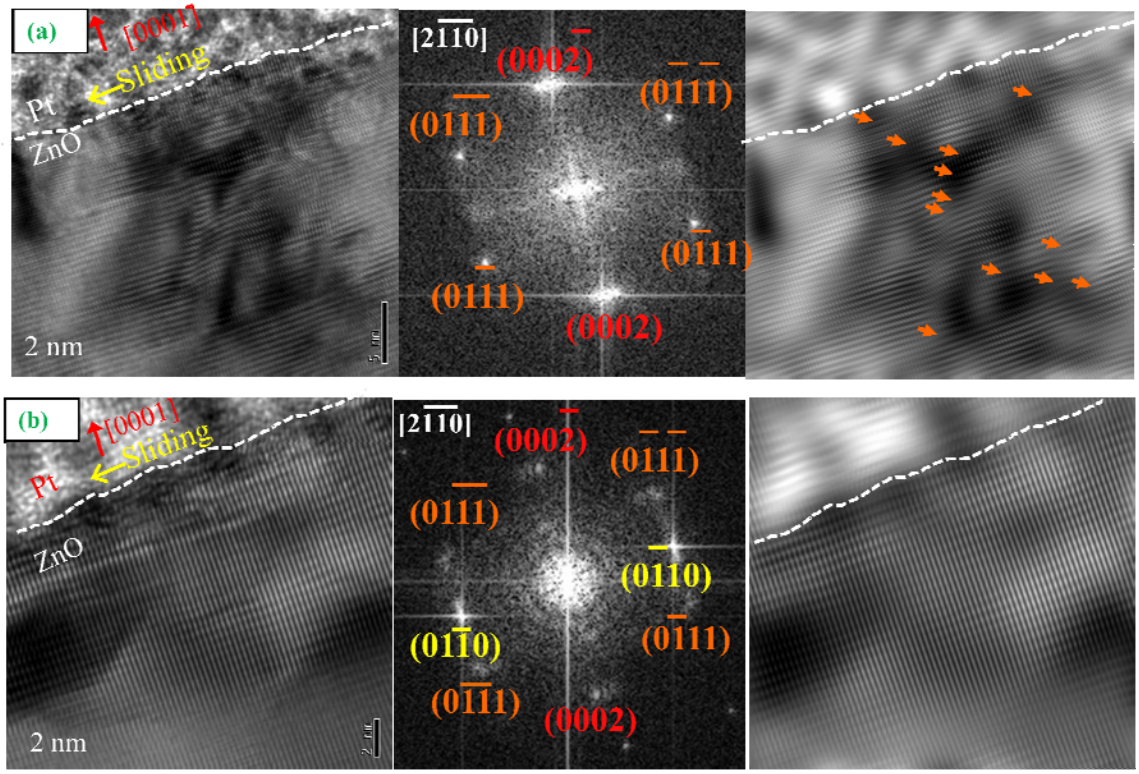

Figure 5.9: XTEM images of the ZnO layer with their corresponding FFT diffraction pattern and the Fourier-filtered image for (a) {0002} basal plane and (b) {01-10} prismatic plane.

5.6 Solid Lubrication Mechanism in the Nanocrystalline ZnO

In order to study the influence of stacking faults on the friction coefficient of the $ZnO/Al_2O_3/ZrO_2/Al_2O_3$ nanolaminate films, it was necessary to analyze the samples from

inside and outside of the wear track. In regards to this, the partial dislocation density was quantified for the as-deposited film, 400^{o}C annealed film and inside the wear track of the annealed film, this is provided in Table 5.1. The partial dislocation density was calculated by counting the number of defects on each micrograph divided by the area of the micrograph. Approximately 40 micrographs were analyzed for each of the above conditions. Based on the calculation, it was observed that the partial dislocation density inside the wear track was the highest, this was followed by the partial dislocation density in the 400^{o}C annealed nanolaminate film. The as-deposited nanolaminate exhibited the lowest partial dislocation density.

Table 5.1: Partial dislocation density in as-deposited, annealed and inside wear track of the (0002) ZnO plane.

ALD 1-Trilayer Nanolaminate	**PD Density (cm^{-2})**
As-deposited	1.5 x 10^{11}
Annealed	6.5 x 10^{11}
Annealed inside wear track	1.2 x 10^{12}

The as-deposited nanolaminate film exhibited low density of partial dislocations because the entire stacking faults in this film is growth related and not due to any applied stress. Thus the {0002}-basal planes are low surface energy planes and they have low stacking fault energies (SFE)[10], recall that basal stacking faults are more likely to be present along the (0002) plane. On the other hand, prismatic and pyramidal planes have

high surface energy planes and have high SFEs. It is therefore very difficult for stacking fault defects to form in these planes. As observed in Figure 5.9b, there were no dislocations present on the prismatic plane even after stress was applied. In the 400^{o}C annealed nanolaminate film, the partial dislocation density increased because ZnO has an open structure and favorable coordination number, this permits Zn to freely move to different positions in the crystal lattice and accommodate external atoms as substitutes. The nanolaminate film was annealed in air; thus the diffusion of oxygen atoms into the ZnO crystal structure is enhanced and this acts as substitute atoms inside the structure. The ideal stacking sequence of the ZnO structure is disrupted which results in additional stacking faults. Finally, after friction test, the partial dislocation density increased once again inside the ZnO (0002) basal plane for the annealed film, this was attributed to the fact that subsurface basal stacking faults were activated to promote intrafilm shear/slip in the ZnO (0002) basal planes. The sliding induced plastic deformation was possible when basal stacking faults were sheared resulting in an intrafilm shear velocity accommodation mode as shown in Figure 5.10. This subsurface aids in shear accommodation (prevents brittle fracture). The high stacking fault density inside the wear track is indicative of the fact that high defect concentration enhances the reduction in the friction coefficient. Thus activating subsurface basal stacking faults will promote intrafilm shear/slip and improve friction. The slip of the partial dislocations is likely to result from a dislocation glide or climb process. It is evident that the individual nanocolumnar ZnO grains are plastically sheared (that is localized nanocrystalline plasticity that is “single crystal” additive and

accumulates to the micro-scale). High resolution SEM analysis indicates a ductile layering and smearing inside the wear tracks.

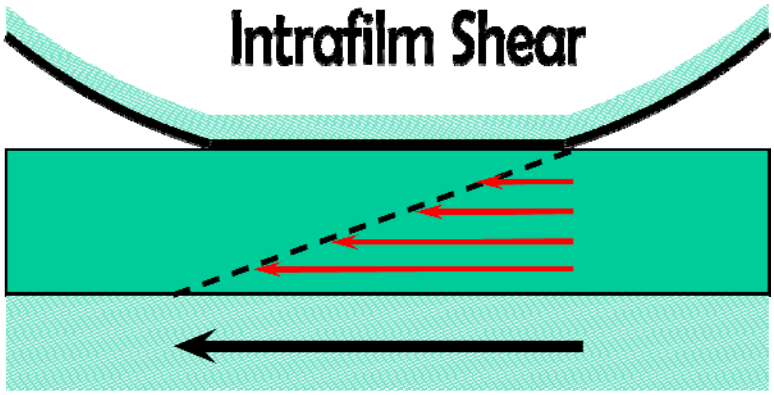

Figure 5.10: Intrafilm shear velocity accommodation mode where a friction-induced subsurface controlled by the material's microstructure aids in shear accommodation (prevents brittle fracture).

5.7 Tribological Behavior of the Nanolaminate in Dry Nitrogen

Recall from the introduction that most of the available solid lubricants today mostly perform best under a limited range of environmental/climatic conditions. Thus the environments play a major role in determining the tribological performance of solid lubricants. One of the reasons of oxides being good potential candidates for solid lubricant is because they are thermodynamically stable materials, thus, oxide lubricants will not degrade but can provide low friction and long life in more than one environment. With regards to this, the tribological behavior of the $ZnO/Al_2O_3/ZrO_2/Al_2O_3$ nanolaminate film was studied in dry nitrogen with less than 1% RH and 10 ppm O_2 at

room temperature. A Si_3N_4 ball with radius of 1.6 mm was used, a normal load of 100 grams was applied with a sliding distance of 16 m.

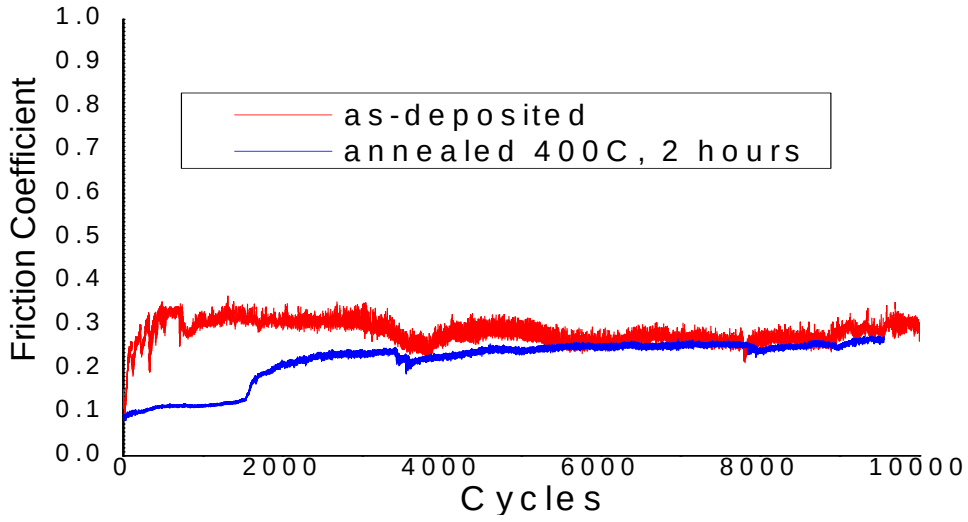

Figure 5.11: COF measurements in dry nitrogen of the as-deposited and 400°C annealed $ZnO/Al_2O_3/ZrO_2/Al_2O_3$ nanolaminate film deposited on M50 steel.

Figure 5.11 shows the friction coefficient plot that was performed in dry nitrogen. Both as-deposited and 400°C annealed films exhibited low COF. The as-deposited nanolaminate film showed steady state friction of approximately 0.29 while the 400°C annealed nanolaminate film produced steady state friction of approximately 0.27. It should be mentioned that these COF values are similar to the ones that were observed in ambient air.

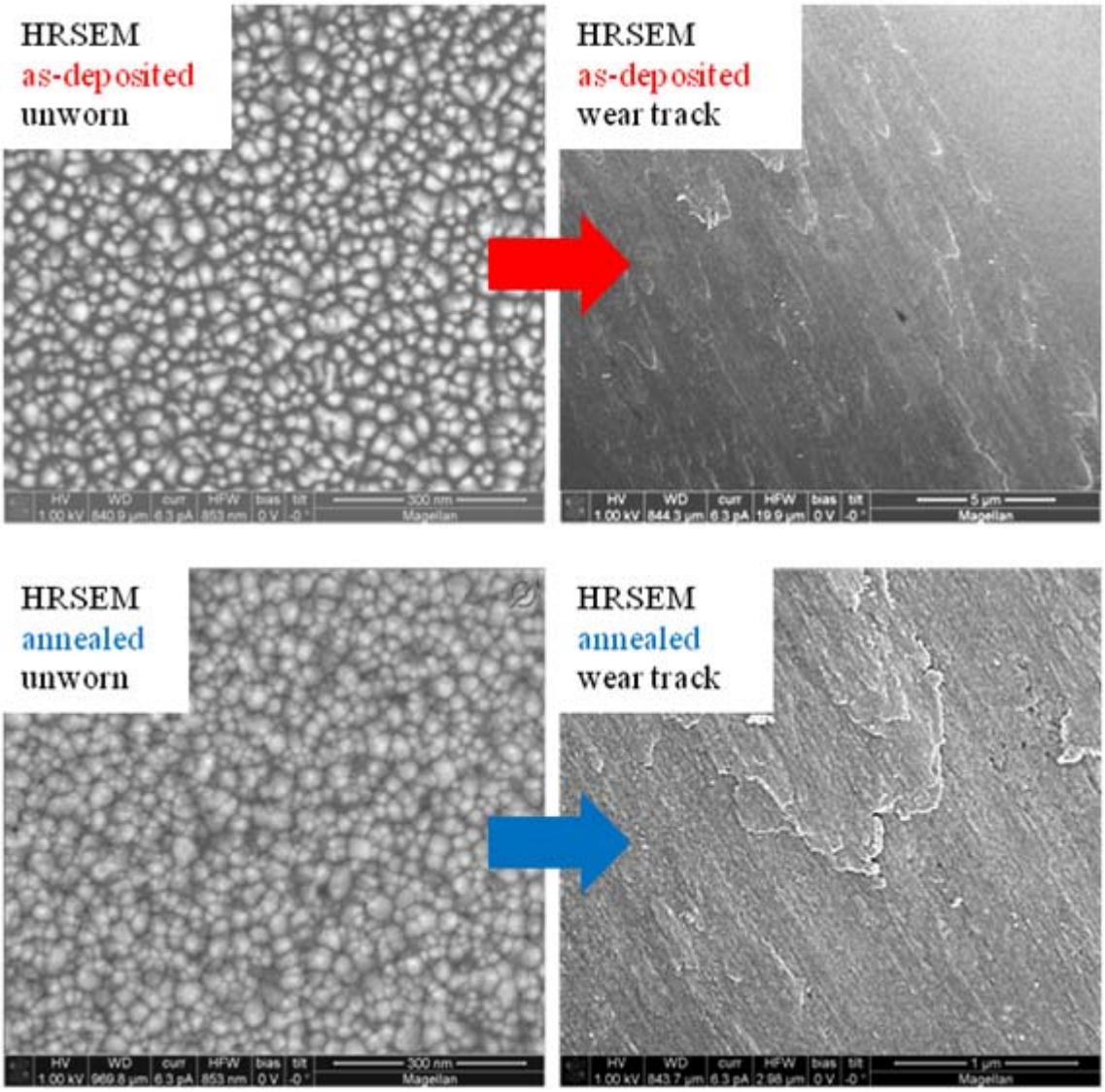

Figure 5.12: High resolution SEM images of as-deposited and 400°C annealed unworn and worn (in dry nitrogen) $ZnO/Al_2O_3/ZrO_2/Al_2O_3$ nanolaminate films deposited on M50 steel.

A high resolution SEM images of the unworn and worn surfaces of both the as-deposited and 400°C annealed nanolaminate films are provided in Figure 5.12. It is observed from this figure that both nanolaminate films did not exhibit any form of brittle fracture (cracks). The surface deformation observed is due to the ductile layering and smearing as

seen in the images. This ductile layering is as a result of the removal of a (0002) basal plane layer and layer transformation from crystalline to amorphous preventing any brittle fracture. This is very consistent with what was observed when the tests were performed under ambient conditions. Thus it could be concluded that the dry nitrogen or lack of atmospheric pressure did not have any major impact on the tribological properties of the nanolaminate films.

5.8 Rolling Contact Fatigue (RCF) Test of the Nanolaminate Film

The $ZnO/Al_2O_3/ZrO_2/Al_2O_3$ nanolaminate solid lubricants were deposited on CrN/Cr/M50 steel cups while $ZnO/Al_2O_3/ZrO_2$ nanolaminate film was deposited on CrN/Cr/M50 steel cylindrical rods for rolling contact fatigue (RCF) test. This was done in order to determine the lifetime of the nanolaminate film coated on the rotating cylindrical specimen. Three 52100 (uncoated) steel balls with Hertzian contact pressure of 1.5 GPa applied were used to roll against the rod and the cups, Figure 5.13 shows the RCF wear tracks inside the cups. Figure 5.13 shows that the nanolaminate film was successfully deposited on the cups and after the RCF test, there is a wear track that is microscopically visible. Different RCF cycles were performed on the cups and rods, the cycles included 10,000, 20,000, 1.3 million and 1.6 million, this was done in order to study the rate of wear.[11] Thus the wear was analyzed after each of these cycles to determine if the coated nanolaminate is still present.

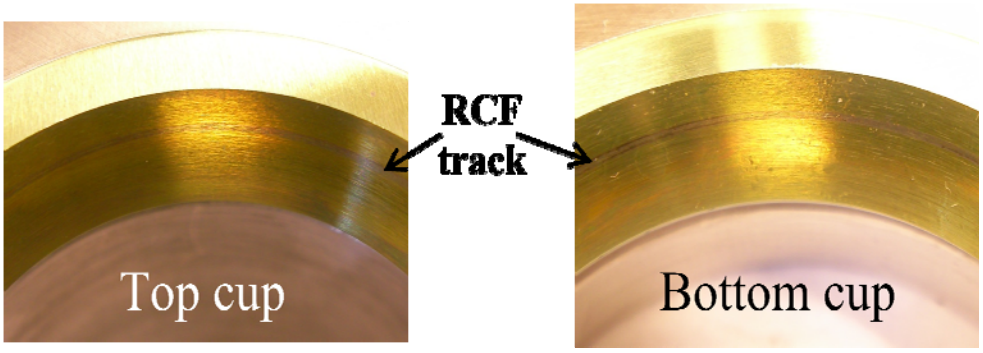

Figure 5.13: Microscopic images showing the $ZnO/Al_2O_3/ZrO_2/Al_2O_3$ nanolaminate film deposited on M50 cups. The arrows points to the wear tracks.

In Figure 5.14, a cross-sectional TEM image of the top part of the cup is shown. The cross sectional TEM cut was performed on the non-polished top surface of the cup (shown as an insert), that is not inside the polished race were the three balls roll, hence there is some high, intrinsic roughness in the TEM micrograph of the layers. The image shows that all the deposited layers are present and the layers actually mimics the surface roughness of the CrN layer that was present prior to the nanolaminate deposition. It is once again observed that the ZnO and ZrO_2 layers are crystalline while the Al_2O_3 layer is amorphous.

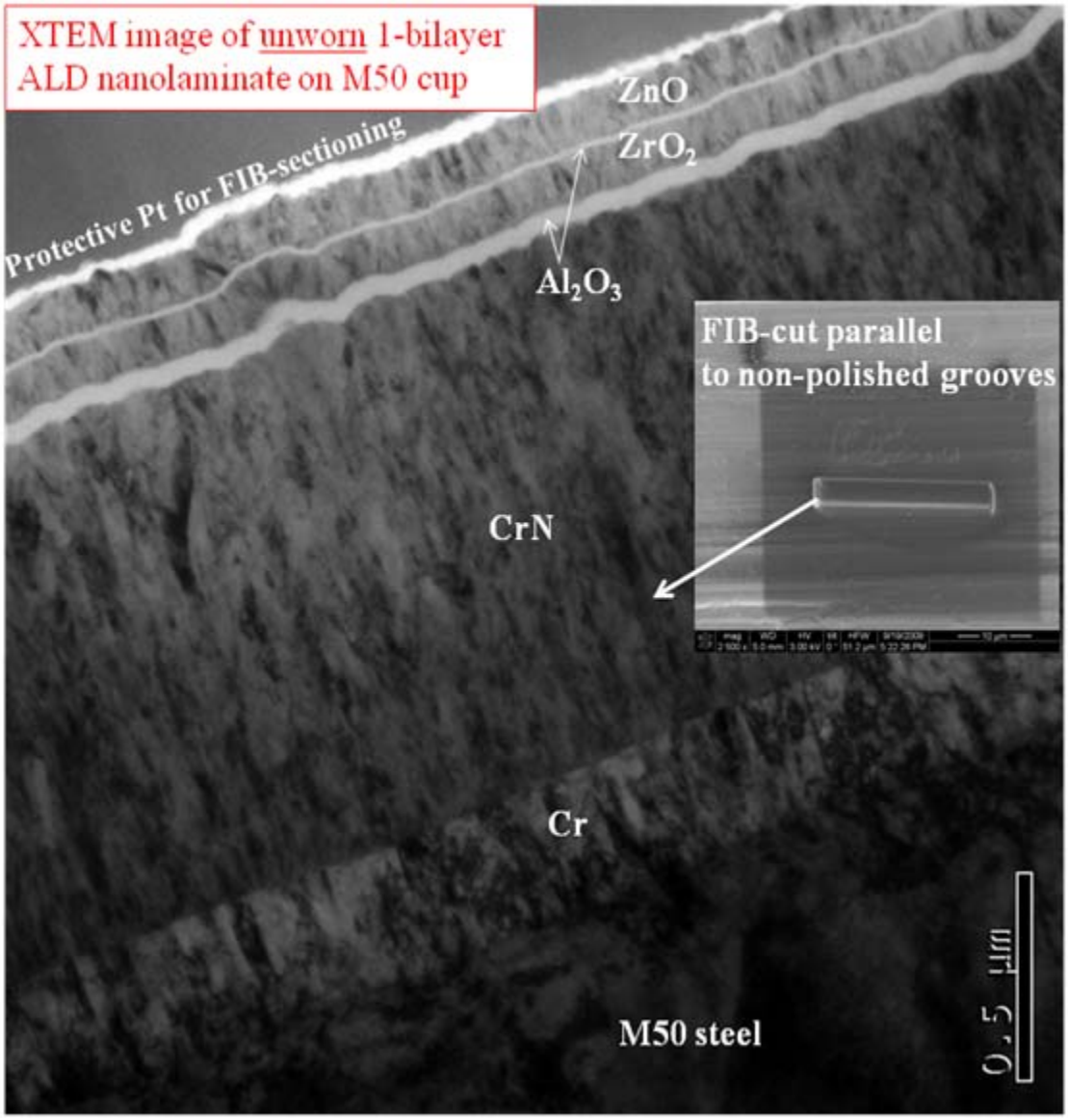

Figure 5.14: XTEM image of $ZnO/Al_2O_3/ZrO_2/Al_2O_3$ nanolaminate film on CrN/Cr/M50 steel cup. Insert is HRSEM image of the location of cross-sectional FIB-cut.

After the 6 million cycles run, a FIB cut was undertaken on the $ZnO/Al_2O_3/ZrO_2$ + CrN/Cr/M50 rod. Figure 5.15 shows the XTEM image of the worn area on the rod after 6 million cycles. Wear was only observed in the top ZnO layer and the wear was non-uniform. There was no evidence of any brittle fracture (cracking). Thus the ALD

deposited nanolaminate film on the rods (Figure 5.15) and cups (not shown) survived under all the RCF cycles (10000, 20000, 1.3 million and 6 million). The whitish amorphous layer on top of the ZnO layer could be the lube (ML-L-23699) that was dropped 8-10 times per minute into the wear tracks during the test or a tribochemical wear that was transferred from the 52100 steel balls thus forming Fe_2O_3 layer. Further chemical analysis needs to be done to determine the exact composition of this amorphous layer.

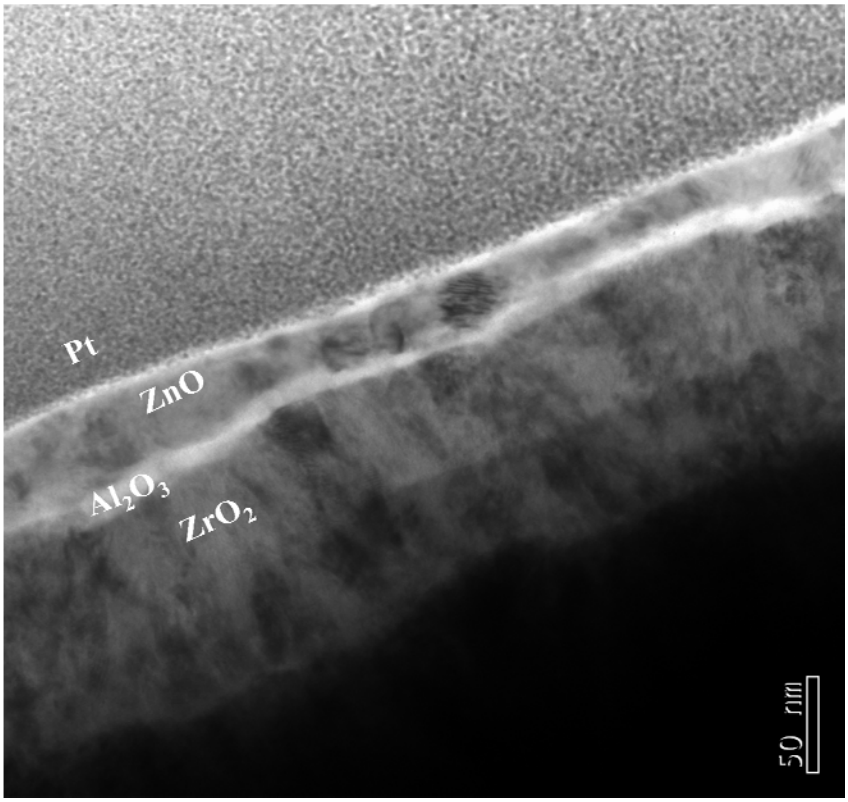

Figure 5.15: XTEM image of worn $ZnO/Al_2O_3/ZrO_2/Al_2O_3$ nanolaminate film on CrN/Cr/M50 rod, this was after 6 million cycles.

A magnified XTEM image of the ZnO layer exhibits (0002) orientation with stacking fault defects present. The arrows in the red boxes of figure 5.16a show the presence of the

stacking faults near the surface of the ZnO layer. The stacking faults that are exhibited in the (0002) plane are bordered by partial dislocations (PDs). The basal stacking faults are connected to the unfaulted crystal by the PDs. Thus during the RCF testing, there is slip of the PDs hence creating a higher density of the BSFs. The presence of stacking faults is observed better in Figure 5.16b, this figure shows one of the filtered images of the ZnO layer. The identification of these dislocations is confirmed in Fourier-filtered images using (0002) diffraction spots, which demonstrate that each PD corresponds to one additional (0002) plane. These stacking faults are shown by the arrows in the images.

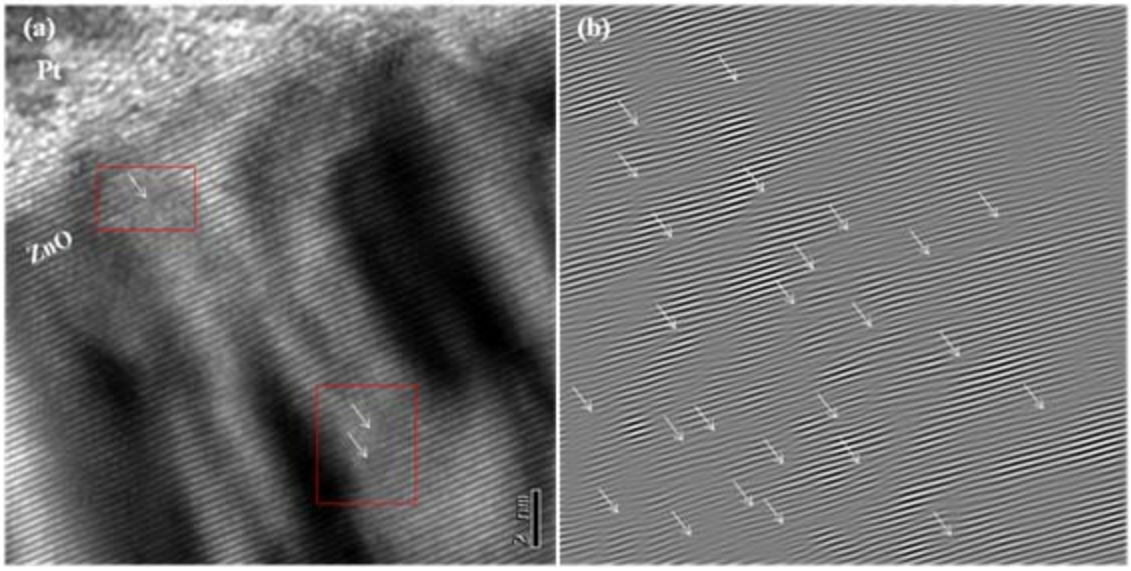

Figure 5.16: (a) Magnified XTEM image of worn ZnO layer showing the presence of stacking faults. (b) Fourier-filtered image of another ZnO layer after RCF test showing the presence of stacking faults.

It can be concluded that the ALD deposited ZnO/Al_2O_3/ZrO_2/Al_2O_3 nanolaminate solid lubricant on CrN/Cr/M50 steel could function as a break-in (conditioning) layer for a

CrN/steel rolling interface where the CrN would otherwise abrade the uncoated steel raceways.

5.9 Chapter Summary

Conformal and uniform ALD $ZnO/Al_2O_3/ZrO_2/Al_2O_3$ nanolaminate films have been successfully deposited on M50 substrates, cups and rods. The following are the conclusions based on the nanolaminate's structural characterization and tribological behavior.

a. XRD analysis showed that the deposited ZnO and ZrO_2 layers were crystalline while the Al_2O_3 was amorphous. The ZnO nano-layer film was highly textured on the (0002) plane and this is known to enhance lubrication. The FWHM of the (0002) peak was determined to be greater than 0.3^o, this behavior has been linked to growth defects such as high/low angle grain boundary, stacking faults etc. It should be mentioned that these observations were also made when the nanolaminate layers were deposited on a silicon substrate (Chapter 4).

b. XTEM analysis of the unworn nanolaminate confirmed the crystallinity of the ZnO and the ZrO_2 with Al_2O_3 being amorphous. Both the ZnO and ZrO_2 crystal structures exhibited nanocolumnar grain growth through thickness. At high magnification, basal stacking faults were observed in the (0002) plane, the high density of BSF were growth defects. A Vienna Ab-initio Simulation Package (VASP) calculation confirmed that the energy required to create stacking fault defects is approximately ten times lower on the (0002) plane than the (01-10)

prismatic plane. Thus stacking faults are more likely to form on the (0002) basal plane than the prismatic plane.

c. Tribological studies showed low friction coefficients and wear factors for both as-deposited and 400^{o}C annealed nanolaminate films. 400^{o}C annealed film exhibited lower friction and wear factor values than the as-deposited nanolaminates. This was attributed to the increase in intensity of the (0002) basal plane XRD peak after the thermal anneal which suggests that the annealing enhanced the (0002) grain growth. A linear regression fit for friction coefficient as a function of inverse Hertzian pressure showed that both as-deposited and 400^{o}C annealed films followed the Bowden and Tabor relation. That is the friction coefficient decreases with increase in applied load.

d. After the tribotest, XTEM analysis was done inside the wear track to determine the effect of the applied stress on the deposited nanolaminate. No cracks were observed after the 200 m sliding distance and the amount of ZnO worn out was very minimal considering the traveling distance. Due to the applied stress, evidence of bending in the nanocolumnar grains of the ZnO layer was observed. FFT diffraction patterns and Fourier-filtered images for the (0002) basal plane and (01-10) prismatic plane confirmed the VASP calculation that even after tribotest, stacking fault defects could not be created in the prismatic planes but rather only in the basal plane.

e. The mechanism by which the ZnO layer acts as a good solid lubricant was studied and it was observed that inside the wear tracks, the density of BSF is very high

compared to the annealed unworn nanolaminate films, the as-deposited nanolaminate film had the lowest BSF density. The high concentration of BSF in the ZnO layer of the wear track is attributed to the sliding induced plastic deformation due to the shearing of the layers resulting in an intrafilm shear velocity accommodation mode. This subsurface is thought to aid in shear accommodation thus preventing brittle fracture.

f. A tribotest was undertaken in dry nitrogen in order to determine the effect of extreme environment on the nanolaminate film. It was observed that the tribological behavior exhibited under the dry nitrogen is similar to that exhibited under ambient environmental conditions. HRSEM analysis also showed that there were no brittle fracture inside the wear track, the only surface deformation that was observed was due to the ductile layering and smearing. Thus the nanolaminate solid lubricant is capable in performing under dry nitrogen conditions.

g. The nanolaminate was successfully deposited on CrN/Cr/M50 cups and rods for rolling contact fatigue test. After 6 million cycles, XTEM analysis showed that only part of the ZnO layer had worn off. No cracks or brittle fracture was observed on the nanolaminate film coated rod. A white layer that is on top of the ZnO layer could not be analyzed to determine whether it was from the applied lube or an iron oxide layer from the 52100 steel balls. Magnified XTEM inside the wear track showed that there was high concentration of stacking faults in the

(0002) plane and these are bordered by partial dislocations. The high stacking fault density is enhancing the lubrication mechanism and thus reducing friction.

In conclusion, it has been shown that it is feasible to generate lubricious oxides through microstructural control at the nanometer level. The ALD deposited nanolaminates are good candidates for providing low friction, wear and good rolling contact fatigue resistance in moving mechanical assemblies that require thin (~10-300 nm), uniform and conformal solid lubricant films.

5.10 Chapter References

[1] Decaudin, B., Djega-Mariadassou, C., Cizeron, G., Journals of Alloys and compounds 226 (1995) 208-212.

[2] Trivedi, H. K., Gerardi, D.T., Rosado, L., Lubrication Science (8) 3 (2006) 211-232.

[3] Mulligan, C.P., Gall, D., Surface and Coatings Technology 200 (2005) 1495-1500.

[4] Zabinski, J. S., Sanders, J. H., Naimaparampil, J., Prasad, S. V., Tribology Letters 8 (2000) 103-116.

[5] Lin, L. –Y., Kim, D. –E., Thin Solid Films 517 (2009) 1690-1700.

[6] Sagalowicz, L., and Fox, G.R., Journal of Materials Research, 14 (1999) 1876

[7] Gerthsen, D., Litvinov, D., Gruber, T., Kirchner, C., Wasag, A., Appl. Phys. Letters 81 (21) (2002) 3972 – 3974.

[8] Sun, H. P., Pan, X. Q., Du, X. L., Mei, Z. X., Zeng, Z. Q., Xue, Q. K., Appl. Phys. Letters (85) 19 (2004) 4385 – 4387.

[9] S. V. Prasad, J. S. Zabinski, J. J. Nainaparamil, Journal of Material Science Letters, 10 (2000) 1979-1981

[10] Yan, Y., Physical Review B, 70 (2004) 193-206

[11] Wereszczak, A.A., Wang, W., Wang, Y., Hadfield, M., Kanematsu, W., Kirkland, T.P., and Jadaan, O.M., http://info.ornl.gov/sites/publications/files/Pub2425.pdf

CHAPTER 6

CONCLUSIONS AND FUTURE WORK

6.1 Conclusions

The major aim of this study was to determine that the $ZnO/Al_2O_3/ZrO_2$ and ZnO/ZrO_2 nanolaminates deposited by Atomic Layer Deposition technique can perform as good lubricous oxide films by exhibiting certain behaviors that allow these films to absorb the applied stress without showing any catastrophic failure and generating any wear debris at different temperatures and environmental conditions. Based on the experimental results, conclusions and future works are summarized in this chapter. In the case of the $ZnO/Al_2O_3/ZrO_2$ trilayer nanolaminate films that were deposited on Si substrates, low friction coefficient values were achieved and no catastrophic failures were observed due to the following reasons:

1. Ex-situ annealing of the ALD nanolaminate films exhibited grain coarsening with increase in the annealing temperature. This effect was very obvious at the 1000^oC temperature films where there was an increase in both friction and wear values.
2. The (0002) basal plane orientation of the ZnO layer has the lowest surface energy which lowers the friction while the (101) prismatic plane has higher surface energy. Thus the lubricous ZnO layer was achieved because the

(0002) ZnO orientation has low stacking fault energies compared to the prismatic plane and can accommodate interfacial shear which tends to exhibit plastic deformation while the other planes exhibit brittle fracture.

3. The presence of ZrO_2 layer acted as a load bearing layer by being able to withstand the high stress that was applied thus preventing any cracks through the nanolaminate films.
4. The thinning of the ZnO layer after 1000^oC anneal was due to the phase transformation of the ZrO_2 layer from tetragonal to monoclinic, this allowed the diffusion of the ZnO into the ZrO_2 layer. This prevented any good tribological behavior and the nanolaminate film became a very hard coating and thus losing its lubricious behavior.

For the ZnO/ZrO_2 two and eight bilayers nanolaminate films, the two bilayer film exhibited good wear and friction behavior as compared to the eight bilayer films at both room and 400^oC annealing temperatures. The reason for this trend are that, the thickness of the top layer ZnO was too thin for the eight bilayer film compared to the two bilayer films. Film thickness in this case influenced the grain growth of the (0002) basal plane thus fewer stacking faults were able to be generated in the eight bilayer film to help reduce the friction.

When the ZnO/Al_2O_3/ZrO_2/Al_2O_3 nanolaminate films were deposited by ALD on M50 substrates, cups and rods, lower friction and wear factor values were observed. The observations that were made during the tests are summarized below:

1. The as-deposited nanolaminate film had lower density of stacking fault compared to the annealed film while the inside the worn area of the annealed nanolaminate film exhibited the highest concentration of stacking faults. The high stacking fault density contributed immensely to the reduction in the friction coefficient and wear factor.
2. High stacking fault energy was computed for the prismatic plane of the ZnO layer while the basal plane stacking fault energy was very low. The energy required to create stacking faults in a prismatic plane is too high and even after friction test, no stacking faults were observed in the prismatic planes.
3. The 400^{o}C annealed nanolaminate films exhibited lower friction coefficient than the as-deposited nanolaminate films. This was shown in a linear regression fit for the friction coefficient verses the inverse Hertzian pressure. All the nanolaminate films followed the Bowden and Tabor relation, which is there was a decrease in friction coefficient with an increase in the applied load.
4. Tribotest inside a dry nitrogen chamber also exhibited good friction coefficient values which were comparable to the ones tested in atmosphere. Hence lack of atmospheric pressure will not have any major impact on the tribological properties of the nanolaminate films.
5. Rolling contact fatigue test on the nanolaminate films deposited on CrN/M50 rods showed wear only in the ZnO layer after 6 million cycles, the wear was non-uniform and not much wear debris was observed. Thus the nanolaminate

ALD solid lubricant could function as a break-in (conditioning) layer for a CrN/steel rolling interface where the CrN would otherwise abrade the uncoated steel raceways.

The nanolaminate films have been successfully deposited on various substrates by the ALD technique. The growth, structural and tribological investigations has demonstrated that by structurally engineering the ZnO layer to conform to the (0002) basal plane, the nanolaminate become both lubricous and exhibit low wear factors at both room and elevated temperatures. The low friction coefficients, wear factors and good rolling contact fatigue resistance that were observed is due to the nanoscale sliding-induced plastic deformation which became possible when the basal stacking faults were sheared resulting in an intrafilm shear velocity accommodation mode. This sub-surface aids in shear accommodation thus preventing brittle fracture. Thus, it is feasible to generate lubricous oxides through Microstructural control at the nanometer level. In addition, the ALD $ZnO/Al_2O_3/ZrO_2$ nanolaminate films are good candidates for providing low friction, wear and good rolling contact fatigue resistance in moving mechanical assemblies that require thin (~10 – 300 nm), uniform and conformal solid lubricant films.

6.2 Future Work

Future work on the oxide lubricants should include but not limited to the following:

1. For high temperature (1000^{o}C) applications, the ZrO_2 layer should either be replaced or stabilized in the tetragonal phase in order to prevent the ZrO_2

phase change from tetragonal to monoclinic which is a transformation toughening mechanism.

2. The newly replaced toughness bearing layer and the other layers should be structurally and tribologically investigated at high temperatures in order to determine if the ZnO layer can withstand these high temperatures.
3. Three-dimensional atom probe (3DAP) should be used to investigate the oxide superlattices of the $ZnO/Al_2O_3/ZrO_2$ and ZnO/ZrO_2 nanolaminate films to help understand the nanostructure and compositional interfaces.
4. With the success achieved in the friction and rolling contact fatigue tests, Timken Company can implement this deposition procedure to function as a break-in (conditioning) layer for a CrN-M50 steel rolling interface where the CrN would otherwise abrade (damage) the uncoated steel raceways. This run in interface can now only be used at room and moderate temperatures.